

CRC Report No. AVFL-7a

**Novel Techniques for NO_x Reduction
in an Oxidative Environment**

Final Report

July, 2008



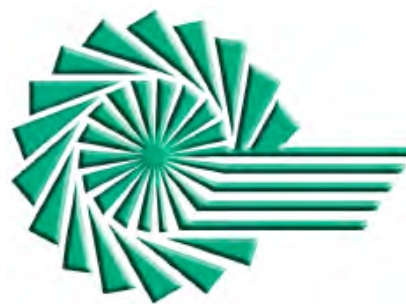
COORDINATING RESEARCH COUNCIL, INC.
3650 MANSELL ROAD • SUITE 140 • ALPHARETTA, GA 30022

The Coordinating Research Council, Inc. (CRC) is a non-profit corporation supported by the petroleum and automotive equipment industries. CRC operates through the committees made up of technical experts from industry and government who voluntarily participate. The four main areas of research within CRC are : air pollution (atmospheric and engineering studies); aviation fuels, lubricants, and equipment performance, heavy-duty vehicle fuels, lubricants, and equipment performance (e.g., diesel trucks); and light-duty vehicle fuels, lubricants, and equipment performance (e.g., passenger cars). CRC's function is to provide the mechanism for joint research conducted by the two industries that will help in determining the optimum combination of petroleum products and automotive equipment. CRC's work is limited to research that is mutually beneficial to the two industries involved, and all information is available to the public.

CRC makes no warranty expressed or implied on the application of information contained in this report. In formulating and approving reports, the appropriate committee of the Coordinating Research Council, Inc. has not investigated or considered patents which may apply to the subject matter. Prospective users of the report are responsible for protecting themselves against liability for infringement of patents.



University of Kentucky



Center for Applied Energy Research

AVFL-7a Final Report

CRC project heading: Novel Techniques for NO_x Reduction in an Oxidative Environment

Project title: Novel Concepts for Low Temperature Hydrocarbon SCR Catalyst Development

Submitted to the Coordinating Research Council

Dr. Christopher J. Tennant
Coordinating Research Council
3650 Mansell Road, Suite 140
Alpharetta, GA 30022
Phone: 678-795-0506
Fax: 678-795-0509

Prepared by

Dr. Mark Crocker* (Principal Investigator)
Dr. Rodney Andrews (Co-Principal Investigator)
University of Kentucky
Center for Applied Energy Research
2540 Research Park Dr.
Lexington, KY 40511-8479
*Tel.: 859-257-0295
*Fax: 859-257-0220
*E-mail: crocker@caer.uky.edu

Table of Contents:

Table of Contents	2
List of Figures	4
List of Tables	6
Executive summary	7
Objective	8
1. Literature study	9
2. Preparation and characterization of support materials	10
<i>Support materials preparation</i>	10
<i>Support materials characterization</i>	12
3. Catalyst preparation and characterization	15
<i>Catalyst preparation</i>	15
<i>Catalyst characterization</i>	16
4. Catalyst screening in a microflow reactor	21
<i>Microflow reactor construction</i>	21
<i>Catalyst screening</i>	23
5. Catalyst optimization	26
<i>Effect of the catalyst support</i>	26
<i>Effect of the catalyst preparation method</i>	27
<i>Effect of the reductant concentration</i>	33
<i>Effect of promotion with Rh and/or Ir</i>	34
<i>Sodium promotion</i>	40
<i>Examination of alternative metals and metal promoters</i>	45
6. Spectroscopic studies	45
<i>STEM and XPS studies</i>	45
<i>Elemental mapping</i>	56
<i>Diffuse Reflectance Infrared Fourier Transform Spectroscopy (DRIFTS) studies</i>	59
7. Reactor studies	60
<i>Kinetic studies</i>	60
8. Preparation of monolithic catalysts	61
<i>Growth of MWNTs on a metal monolith</i>	61
<i>Precious metal deposition on monolith-grown MWNTs</i>	62
<i>Activation of monolith-grown MWNTs</i>	63
9. Engine tests	66
<i>Pt/NO₂-fMWNTs/metal monolith catalyst</i>	66
<i>3:1 Pt-Rh/NO₂-fMWNTs/metal monolith catalyst</i>	68
Conclusions	72
References	73
Appendix: Experimental Methods	75
A. Preparative	75
<i>Functionalization of MWNTs with a mixture of 1:1 H₂SO₄-HNO₃</i>	75
<i>PGM deposition via wet impregnation</i>	75
<i>PGM deposition via the polyol method</i>	75
<i>Growth of MWNTs on a metal monolith</i>	75
<i>Functionalization of metal monolith-grown MWNTs with 0.5% NO₂ in N₂</i>	75
<i>PGM deposition on NO₂-functionalized monolith-grown MWNTs via the polyol method</i>	76

B. Analytical	76
<i>Determination of precious metal loadings.</i>	76
<i>Precious metal particle size analysis.</i>	76
<i>Thermogravimetric analyses.</i>	77
<i>Spectroscopic analyses.</i>	77
C. Catalyst testing	77
<i>Powder catalysts.</i>	77
<i>Monolith catalysts</i>	77

List of Figures:

Figure 1. Schematic of carbon nanotube functionalization with acid.....	11
Figure 2. Schematic of Pt deposition on acid activated MWNTs.....	11
Figure 3. TEM image showing the disruption of the MWNT graphene structure as a result of acid treatment.....	14
Figure 4. Background corrected ATR IR spectra of 1:1 H ₂ SO ₄ -HNO ₃ treated MWNTs.....	14
Figure 5. STEM-Z image showing Pt particles deposited on Darco KB-B.....	19
Figure 6. TGA plot of different carbon supports with and without Pt under 10% O ₂ in N ₂	19
Figure 7. TEM image of Pt/Al ₂ O ₃ and corresponding EDS spectrum.....	21
Figure 8. Reactor schematic.....	22
Figure 9. Microflow reactor.....	22
Figure 10. Plot showing the performance of 1 wt.% Pt/Al ₂ O ₃ in NO reduction with propene.....	23
Figure 11. Plot showing the performance of 1 wt.% Pt/fMWNTs in NO reduction with propene.....	24
Figure 12. Combined plot comparing the performance of 2 wt. % Pt/fMWNTs-I, 2 wt.% Pt/activated carbon fibers-I and 2 wt.% Pt/Al ₂ O ₃ -I in NO reduction with propene.....	25
Figure 13. Combined plot comparing the performance of Pt/MWNTs-I and Pt/fMWNTs-I in NO reduction with propene.....	27
Figure 14. Combined plot comparing the performance of 2 wt.% Pt/fMWNTs-I, 2 wt.% Pt/fMWNTs-P and 2 wt.% Pt/MWNTs-I in NO reduction with propene.....	28
Figure 15. Particle size distribution histograms of 2 wt.% Pt/fMWNTs-I, 2 wt.% Pt/fMWNTs-P and 2 wt.% Pt/MWNTs-I.....	29
Figure 16. TEM micrographs of fMWNTs and bfMWNTs.....	30
Figure 17. Combined TGA plot for fMWNTs and bfMWNTs under 10% O ₂ in N ₂	31
Figure 18. Particle size distribution histograms for 2 wt.% Pt/fMWNTs and 2 wt.% Pt/bfMWNTs.....	32
Figure 19. Combined plot comparing the performance of 2 wt.% Pt/fMWNTs and 2 wt.% Pt/bfMWNTs in NO reduction with propene.....	33
Figure 20. Combined plot comparing the performance of 2 wt.% Pt/fMWNTs in NO reduction with propene under different propene:NO ratios.....	34
Figure 21. Combined plot comparing the performance of 2 wt.% Pt/fMWNTs-I, 1 wt.% Pt – 1 wt.% Rh/fMWNTs-I and 1 wt. % Pt – 1 wt.% Ir/fMWNTs-I in NO reduction with propene.....	35
Figure 22. Combined plot comparing the performance of Pt/fMWNTs-I and Pt-Rh/fMWNTs-I with different Pt:Rh ratios in NO reduction with propene.....	36
Figure 23. Particle size distribution histograms for 1.0 wt.% Pt – 1.0 wt.% Rh/fMWNTs-I, 1.5 wt.% Pt – 0.5 wt.% Rh/fMWNTs-I and 1.8 wt.% Pt – 0.2 wt.% Rh/fMWNTs-I.....	37
Figure 24. Particle size distribution histograms for fresh 2 wt.% Pt/fMWNTs-I, 2 wt.% Pt/fMWNTs-I after exposure for ~12 h to reaction conditions, fresh 1.5 wt.% Pt – 0.5 wt. % Rh/fMWNTs and 1.5 wt.% Pt – 0.5 wt. % Rh/fMWNTs after exposure for ~12 h to reaction conditions.....	38
Figure 25. Combined plot showing the performance of three 1.5 wt.% Pt – 0.5 wt.% Rh/fMWNTs catalysts prepared by different methods.....	40
Figure 26. Plot showing the performance of 2 wt.% Pt – 10 wt.% Na/fMWNTs-I, 2 wt.% Pt – 1 wt.% Na/fMWNTs-I and 2 wt.% Pt – 5 wt.% Na/fMWNTs-I in NO reduction with propene.....	41

Figure 27. TEM micrograph of a region containing a MWNTs aggregate within a 2 wt.% Pt – 10 wt.% Na/fMWNTs-I catalyst and corresponding EDS spectrum	43
Figure 28. TEM micrograph of a region containing well dispersed MWNTs within a 2 wt.% Pt – 10 wt.% Na/fMWNTs-I catalyst and corresponding EDS spectrum	44
Figure 29. TEM and STEM micrographs of Pt-Ir/fMWNTs-I and corresponding EDS spectrum	46
Figure 30. STEM micrographs under different magnifications of 2 wt.% Pt/fMWNTs-I.....	47
Figure 31. STEM micrograph of 2 wt.% Pt/fMWNTs-I and corresponding EDS spectrum.....	48
Figure 32. STEM micrograph of 1 wt.% Pt - 1 wt.% Rh/fMWNTs-I and corresponding EDS spectrum.....	49
Figure 33. Particle size distribution histograms for 10 wt.% Pt/Al ₂ O ₃ , 10 wt.% Pt/MWNTs, 10 wt.% Pt/fMWNTs and 7.5 wt.% Pt – 2.5 wt.% Rh/fMWNTs.....	51
Figure 34. Expanded view of the Pt 4d region in the XPS spectrum of the 10 wt.% Pt/Al ₂ O ₃	52
Figure 35. Combined plot showing an expanded view of the Pt 4f region in the XPS spectra of 10 wt.% Pt/MWNTs, 10 wt.% Pt/fMWNTs and 7.5 wt.% Pt – 2.5 wt.% Rh/fMWNTs	53
Figure 36. Expanded view of the Pt 4f and the Al 2p region in the XPS spectrum of 10 wt.% Pt/Al ₂ O ₃ prepared by impregnation followed by H ₂ reduction.....	55
Figure 37. STEM micrograph of a 1.5 wt.% Pt – 0.5 wt.% Rh/fMWNTs, corresponding carbon, platinum and rhodium elemental maps and composite image of all three maps.....	56
Figure 38. Carbon, platinum and sodium elemental maps of three 2 wt.% Pt – 10 wt.% Na/fMWNTs catalysts prepared by different preparation methods.....	58
Figure 39. Photograph of a metal monolith coated with MWNTs and SEM image of the MWNTs showing their alignment.	61
Figure 40. TEM image of Pt/MWNTs/metal monolith and corresponding EDS spectrum.....	62
Figure 41. TEM image of Pt/MWNTs/metal monolith.....	63
Figure 42. TEM micrographs of Pt/NO ₂ -fMWNTs/metal monolith	65
Figure 43. TEM micrographs of 3:1 Pt-Rh/NO ₂ -fMWNTs/metal monolith.....	65
Figure 44. Results of temperature sweep for Pt/NO ₂ -fMWNTs/metal monolith (GSHV = 30,000 h ⁻¹).....	66
Figure 45. Results of temperature sweep for Pt/NO ₂ -fMWNTs/metal monolith (GSHV = 50,000 h ⁻¹).....	67
Figure 46. Results of temperature sweep for 3:1 Pt-Rh/NO ₂ -fMWNTs/metal monolith (GSHV = 30,000 h ⁻¹).....	68
Figure 47. Results of temperature sweep for 3:1 Pt-Rh/NO ₂ -fMWNTs/metal monolith (GSHV = 50,000 h ⁻¹).....	69
Figure 48. Results of C:NO _x sweep for 3:1 Pt-Rh/NO ₂ -fMWNTs/metal monolith	70
Figure 49. N ₂ O make during C:NO _x sweep for 3:1 Pt-Rh/NO ₂ -fMWNTs/metal monolith.....	70

List of Tables:

Table 1. Summary of literature concerning use of Pt alloy catalysts in HC-SCR.....	10
Table 2. Elemental analysis of pristine and acid-treated MWNTs.....	12
Table 3. EDS analysis of pristine and acid-treated MWNTs.....	12
Table 4. Surface properties of pristine and acid-treated MWNTs.....	13
Table 5. Elemental analysis of an activated carbon fiber monolith.....	15
Table 6. Physical properties of an carbon fiber monolith.....	15
Table 7. Precious metal loadings of the catalysts prepared via the polyol method determined by ICP-AES.....	17
Table 8. Elemental analysis data for two catalysts analyzed by different techniques.....	17
Table 9. Hydrogen chemisorption results showing the dispersion and average diameter of Pt particles on different substrates.....	18
Table 10. Differential thermogravimetric maxima for selected samples.....	20
Table 11. Elemental analysis of fMWNTs and bfMWNTs.....	31
Table 12. NO conversion data for selected Pt and Pt-Rh catalysts.....	37
Table 13. Metal dispersion and average particle size of model Pt/Al ₂ O ₃ reference catalysts.....	50
Table 14. Kinetic data for 2 wt.% Pt/fMWNTs and 1.5 wt.% Pt – 0.5 wt.% Rh/fMWNTs.....	60

Executive summary:

The objective of this project was to develop precious metal/carbon nanotube composite materials as active, selective and oxidation-resistant catalysts for the reduction of nitrogen oxides under lean conditions. Metals were deposited on pristine and functionalized multi-walled carbon nanotubes (MWNTs and fMWNTs, respectively), and the resulting catalysts were characterized and tested in a microflow reactor using propene as the reductant. Once the catalysts with the best performance were identified, experiments were performed with the aim of optimizing these formulations with respect to the support, preparation method, and supported metal phase. A 1.5 wt.% Pt – 0.5 wt.% Rh/fMWNTs catalyst prepared *via* impregnation was found to show optimum NO_x reduction activity. This catalyst showed a maximum NO conversion of ~60% at 200 °C (at a GHSV of ~50,000 h⁻¹), the selectivity to N₂ at this temperature being ~45%. Further, the effect of Na⁺ promotion on the activity and selectivity of the Pt/fMWNTs and Pt-Rh/fMWNTs catalysts was investigated. Both the preparation method and the Pt:Na ratio were found to be critical variables for successful catalyst promotion, a 2.0 wt.% Pt – 10.0 wt.% Na/fMWNTs catalyst prepared by a method involving two subsequent impregnations showing the most promising performance. This catalyst showed a NO conversion of between 20 and 30% and a selectivity to N₂ of *circa* 100% over the 130 to 300 °C temperature range. In order to gain fundamental insights which may inform further improvements to MWNTs-based catalysts, reactor and spectroscopic measurements were performed in order to: 1) study the relationship between catalyst structure and NO_x reduction activity, and 2) probe the mechanism of NO_x reduction over these catalysts. Finally, the synthesis of the most promising catalysts was scaled up, using commercial metal monoliths as the catalyst substrate. The results of engine testing revealed that the monolithic Pt and Pt-Rh catalysts were fairly active for the oxidation of CO and hydrocarbons, while NO_x reduction activity was found to be rather low; this fact can be largely attributed to the very high effective space velocities used. Of interest is the finding that the N₂O make declined at high C:NO_x ratios, even as the NO_x conversion increased. This suggests that high hydrocarbon surface coverage inhibits N₂O formation.

Objective:

The aim of this project was to optimize hydrocarbon Selective Catalytic Reduction (HC-SCR) performance. Given that one of the main drawbacks of HC-SCR is the narrow temperature range of operation shown by the catalysts, the use of a low temperature formulation (which would operate in the 150-300 °C range) and a high temperature formulation (for the 300–500 °C range) was proposed, together with the use of a gas switching system that would ensure the utilization of the appropriate catalyst based on the exhaust gas temperature. Platinum supported on activated carbon was identified as the best low temperature HC-SCR catalyst based on its high deNO_x activity. Furthermore, the fact that both catalyst activity and selectivity could be improved by alloying Pt with other metals, such as Rh and/or Ir, had been indicated. However, two major concerns remained: 1) the propensity of carbon supports to undergo combustion in an oxidizing environment, and 2) the fact that in the case of alloy catalysts, it is frequently unclear which is the active site (i.e., whether NO_x conversion takes place over alloyed particles or over monometallic ones). Therefore, it was proposed to: 1) examine the use of multi-walled carbon nanotubes (MWNTs) as the support for low temperature HC-SCR catalysts (on the basis that they are more resistant to oxidation than amorphous forms of carbon), and 2) study structure-activity relationships in Pt-based metal alloy catalysts in order to gain fundamental insights which may aid the design of HC-SCR catalysts.

1. Literature study.

Prior to commencing experimental work, the literature study undertaken during preparation of the project proposal was extended with the purpose of identifying other candidate metal alloy catalysts for inclusion in the screening process.

It was confirmed that there had been relatively little research directed at the use of metal alloys in HC-SCR, although some workers had found that the fresh state, zeolite and alumina-supported Pt-Rh alloys show enhanced activity relative to Pt-only catalysts [1,2]. However, upon hydrothermal aging at 600 °C, the performance of the Pt-Rh catalyst declines significantly, whereas Pt/alumina shows only a small decline at this temperature [2]. These findings suggested that use of a Pt-Rh catalyst could be advantageous if sufficiently protected from hydrothermal aging. Further, use of a carbon-based support, rather than alumina, may be beneficial, by helping to maintain the Pt-Rh alloy in a more reduced state; over-oxidation of Rh is well-known in three-way catalysis as a cause of (reversible) deactivation (Rh^{III} being significantly less active in NO_x reduction than $\text{Rh}^{\text{I}}/\text{Rh}^0$).

A related catalyst system comprises Pt-Rh-Ir supported on ZSM-5, which was developed for Mazda 323 lean burn vehicles sold in the Japanese market [3-6]. Testing of various precious metal combinations gave the order Pt-Rh-Ir>Pt-Ir>Pt>Ir for NO_x reduction activity at 300 °C (using propene as the reductant). N_2O make over the Pt-Rh-Ir catalyst was reported to be negligible and although some deactivation was observed upon aging the catalyst at 700 °C, durability was said to be adequate for the application. Unfortunately, data pertaining to the state of the metals in the catalyst were not provided, so it is not clear if Pt-Rh-Ir alloy particles are indeed the active sites (as opposed to mono- or bi-metallic particles). However, these reports provided a useful starting point for the study of Ir-containing alloy catalysts. Iridium catalysts have been used by Mitsubishi for lean burn vehicles sold in Europe [7], although this is no longer the case. This is in part due to concerns surrounding the volatility of IrO_3 at high temperatures, which can result in loss of Ir from the catalyst. In the case of a system based on exhaust gas switching, this problem could clearly be avoided.

The results of the literature study are summarized in Table 1. In short, few additional references were found proposing precious metal alloys as active HC-SCR catalysts, and those that were found support the idea that Pt-Rh and Pt-Rh-Ir alloys show the most promise for this particular application.

Table 1. Summary of literature concerning use of Pt alloy catalysts in HC-SCR.

Year	Catalysts studied	Comment	Authors	Reference
2003	Pt, Pd, Rh, Pt-Pd, Pt-Rh, Pd-Rh, all supported on alumina	NO _x conversion w/ propene: Rh(73%, 375 °C)>Pt (65%, 225 °C)>Pd (47%, 275 °C). Pt-Rh is best bimetallic catalyst (main effect is simply to broaden temperature window for NO _x conversion)	J.-H. Li, J.-M. Hao, L.-X. Fu, T.-L. Zhu, L.-L. Chen	<i>Gao deng xue xiao hua xue xue bao (Chem. J. of the Chinese Universities)</i> , 24 (11), 2060-2064
2001	Ir/ZSM-5, and physical mixture of Ir/ZSM-5 and Pt-Rh/Al ₂ O ₃	Ir/ZSM-5 shows good durability. Ir/ZSM-5 + Pt-Rh/Al ₂ O ₃ mixture used for improved lean and stoichiometric NO _x reduction	S. Nojima, K. Iida, N. Kobayashi	<i>Nippon Kagaku Kaishi</i> , 2001(1), 27-36
2000	Pt-Rh/zeolite	Alloying claimed to improve resistance of precious metal to sintering and sulfation in lean NO _x reduction	M. Ishikawa	JP2000140644 (to Toyota Motor Corp.)
2000	Pt-Au, Pt-Ag, Pt-Rh, Pt-Pd-Rh, Pt-Rh-Co, supported on alumina	Claims use of sequential multicomponent catalysts to cover broad temperature range. Temp. range of lean NO _x reduction: Pt/Au: 475-800 °C; Pt/Ag: 315-475 °C; Pt/Rh, Pt/Pd/Rh, Pt/Rh/Co: 200-425 °C	K.C.C. Kharas, H.J. Robota, M.G. Henk	WO 00/00272 (PCT/US98/19281) (ASEC)
2000	Pt-Rh-Co/Ba-stabilized alumina, Pt-Rh/alumina	Continuation of US 5,894,068	K.C.C. Kharas, H.J. Robota	US 6,087,295 (to ASEC)
1999	Pt-Rh-Co/Ba-stabilized alumina, Pt-Rh/alumina	Claims use of sequential multicomponent catalysts to cover broad temperature range. Some NO _x conversion data given.	K.C.C. Kharas, H.J. Robota, M.G. Henk	US 5,894,068 (to ASEC)
1999	Pt-Cu, Pt-Ag, Pt-Rh, Pt-Rh-Co, supported on alumina or Ba-stabilized alumina	Claims method of catalyst preparation. Some NO _x conversion data given.	K.C.C. Kharas, H.J. Robota, J.G. Nunan, M.G. Henk	US 5,977,012 (to ASEC)
1999	Pt, Ir, Rh, Pt-Ir, Pt-Rh, Ir-Rh, Pt-Ir-Rh, all supported on H-ZSM-5	Pt-Ir-Rh/H-ZSM-5 most active (also after aging)	H. Iwakuni, A. Takami, K. Komatsu	<i>Stud. Surf. Sci. Catal.</i> , 121 , 251-256
1997	As for 1999 publication	As for 1999 publication	A. Takami, T. Takemoto, H. Iwakuni, K. Yamada, M. Shigetsu, K. Komatsu	<i>Catal. Today</i> , 35 , 75-81
1995	As for 1999 publication	As for 1999 publication	A. Takami, T. Takemoto, H. Iwakuni, F. Saito, K. Komatsu	SAE 950746
1995	As for 1999 publication	As for 1999 publication	M. Shigetsu, A. Takami, M. Kyougoku, H. Iwakuni, F. Saito, K. Komatsu	<i>Matsuda Giho</i> , 13 , 30-36
1993	Pt, Rh, Ir, Ru, Pd, Pt-Rh, Pt-Au, all supported on γ -Al ₂ O ₃	Claims a 3:1 Pt:Rh weight ratio to show the highest and widest NO _x conversion	A. Obuchi, A. Ohi, M. Nakamura, A. Ogata, K. Mizuno, H. Ohuchi	<i>Appl. Catal. B</i> , 2 , 71-80

2. Preparation and characterization of support materials.

Support materials preparation:

As a first step, a batch of MWNTs was prepared using a chemical vapor deposition method [8]. For catalytic applications, MWNTs are usually first treated with a strong mineral acid to introduce oxygen functionalities onto the surface in the form of carboxylic, phenolic and lactonic groups, these acting as nucleation sites when supporting metals or metal oxides. Figure 1 schematically shows how these functionalities are introduced to both the outer-wall and the tip of a MWNT, and Figure 2 illustrates how these functionalized multi-walled nanotubes (fMWNTs) can nucleate precious metal particles.

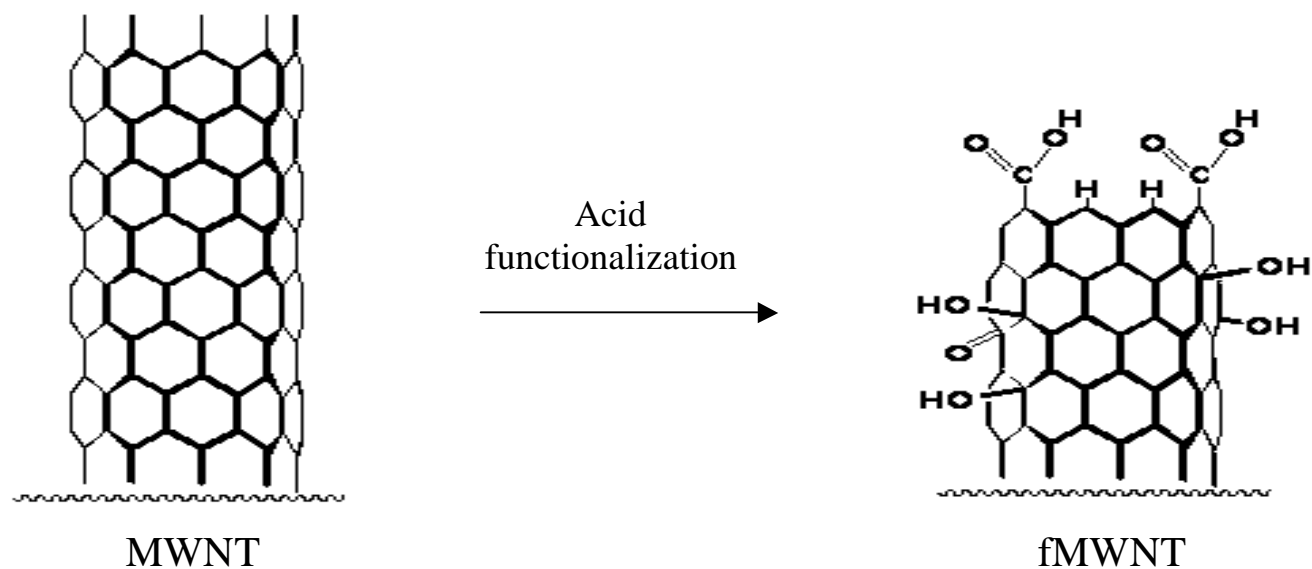


Figure 1. Schematic of carbon nanotube functionalization with acid.

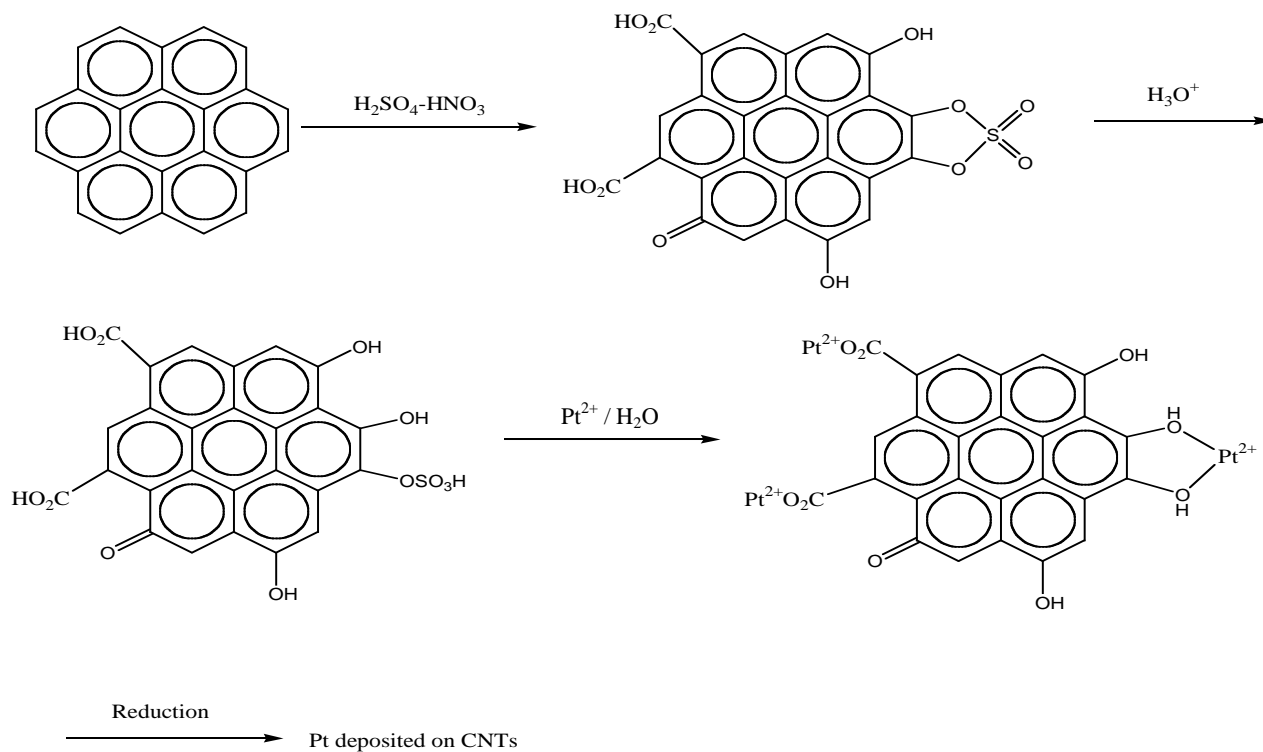


Figure 2. Schematic of Pt deposition on acid activated MWNTs (after Yu *et al.* [9]).

Although not essential, this treatment is generally beneficial for the dispersion of the supported phase. To this end, several literature-based procedures were studied for the acid activation of the as-synthesized MWNTs. Procedures utilized comprised (i) treatment with refluxing HNO₃ [10], (ii) refluxing with 1:1 H₂SO₄:HNO₃ [9], (iii) treatment with 1:1 H₂SO₄:HNO₃ under ultrasound irradiation [11], and (iv) refluxing with 3:1 H₂SO₄:HNO₃. In the case of methods (i)-(iii) the resulting fMWNTs were readily isolated by filtration, whereas the material prepared according to method (iv) could not be easily isolated by filtration or centrifugation. We speculate that the surface oxidation of the MWNTs is so effective in this case that the MWNT bundles are broken up into very small units (possibly individual nanotubes), a process which is presumably driven by the high degree of solvation of the oxidized nanotubes. Given typical MWNT dimensions (30-50 nm in diameter x 65 μm in length), this renders their isolation problematic; although use of a 20 nm filter does permit their isolation by filtration, the process is extremely time-consuming. For this reason, this activation method was not pursued in subsequent work.

Support materials characterization:

Characterization of the fMWNTs resulting from procedures (i)-(iii) was accomplished using nitrogen physisorption (for determination of the BET surface area), titration with NaOH (to quantify the concentration of acid groups present), elemental analysis (*via* combustion), and Transmission Electron Microscopy-Energy Dispersive X-ray Spectroscopy (TEM-EDS). Results of the elemental analysis are summarized in Table 2, EDS analysis is given in Table 3, and N₂ physisorption data and titration results are collected in Table 4.

Table 2. Elemental analysis (by combustion) of pristine and acid-treated MWNTs.

Sample code	Sample / treatment	%C	%H	%N	%S	%O ⁽¹⁾	% Ash
AS	As synthesized nanotubes	93.12	<0.01	0.19	-	<0.01	7.69
AT-1	HNO ₃ -treated (reflux, 4 h)	97.01	0.01	0.25	-	0.58	2.15
AT-2	1:1 H ₂ SO ₄ -HNO ₃ -treated (reflux, 4 h)	90.45	0.34	0.2	0.06	6.55	2.4
AT-3	1:1 H ₂ SO ₄ -HNO ₃ -treated (sonication, 2 h)	93.32	0.15	0.32	0.15	1.64	4.42
AT-4	1:1 H ₂ SO ₄ -HNO ₃ -treated (reflux, 4 h) ⁽²⁾	88.4	0.42	0.27	0.12	7.15	3.64

⁽¹⁾ Determined by difference, i.e., wt% O = 100 - wt% [C + H + N + S + ash]. ⁽²⁾ Repeat of AT-2 preparation using slightly modified conditions.

Table 3. EDS analysis of pristine and acid-treated MWNTs.⁽¹⁾

Sample code	Sample / treatment	%C	%S	%O	%Si ⁽²⁾
AS	As synthesized nanotubes	>99.5	-	n.d. ⁽³⁾	n.d.
AT-1	HNO ₃ -treated (reflux, 4 h)	>98.6	-	n.d.	0.9
AT-2	1:1 H ₂ SO ₄ -HNO ₃ -treated (reflux, 4 h)	90.3	1.3	7.9	0.5
AT-3	1:1 H ₂ SO ₄ -HNO ₃ -treated (sonication, 2 h)	95.3	2.4	1.6	0.8
AT-4	1:1 H ₂ SO ₄ -HNO ₃ -treated (reflux, 4 h)	88.4	0.12	7.15	n.d.

⁽¹⁾ Element concentrations in wt%; figures given represent the average of at least three measurements performed on different sample areas.

⁽²⁾ Impurity associated with the presence of silicone grease.

⁽³⁾ Not detected.

Table 4. Surface properties of pristine and acid-treated MWNTs.

Sample code	Sample / treatment	BET surface area (m ² /g)	Pore volume (cm ³ /g)	NaOH titration: acid eq. neutralized (meq/g)
AS	As synthesized nanotubes	42.1	0.182	0.02
AT-1	HNO ₃ -treated (reflux, 4 h)	51.2	0.160	0.40
AT-2	1:1 H ₂ SO ₄ -HNO ₃ -treated (reflux, 4 h)	54.3	0.242	1.11
AT-3	1:1 H ₂ SO ₄ -HNO ₃ -treated (sonication, 2 h)	46.5	0.182	0.59
AT-4	1:1 H ₂ SO ₄ -HNO ₃ -treated (reflux, 4 h)	59.2	0.272	0.77

Taken as a whole, these data present a consistent picture. The presence of oxygen in the activated nanotubes is indicative of surface oxygen-containing groups, while the detection of increased concentrations of nitrogen suggests the presence of nitro (-NO₂) groups (presumably resulting from electrophilic substitution reactions of NO₂⁺). Similarly, the use of H₂SO₄ during the activation procedure results in the incorporation of sulfur in the product MWNTs, presumably present as sulfonic acid groups (-SO₃H).

The results of aqueous titrations provided further evidence for the introduction of acidic groups onto the nanotubes. Given that NaOH was used as the titrant, the measured acid concentrations in each case correspond to the total number of carboxylic, phenolic and lactonic groups present (since each of these functionalities is titrated by NaOH [12]). Based on the measured acid site concentrations, the severity of the treatment follows the order 1:1 H₂SO₄-HNO₃/reflux > 1:1 H₂SO₄-HNO₃/ultrasound > HNO₃/reflux. This ordering is broadly supported by the results of elemental analysis as reflected in the measured oxygen concentrations (determined by TEM-EDS and combustion analysis). Acid treatment also results in a reduction in the ash content of the samples, indicative of acid-leaching of the residual iron particles present in the MWNTs (the MWNTs having been grown via an iron-catalyzed process [8] and the ash left by the combustion analysis being iron oxide formed from these residual iron particles).

N₂ physisorption measurements show an increase in the BET surface area of the MWNTs after activation, consistent with tube opening via acid attack at the semi-fullerene capped ends [9] and with the etching of the MWNTs outer surface. The latter phenomenon was confirmed by TEM. Figure 3 shows the etched outer wall of a MWNT subjected to treatment with refluxing 1:1 H₂SO₄-HNO₃.

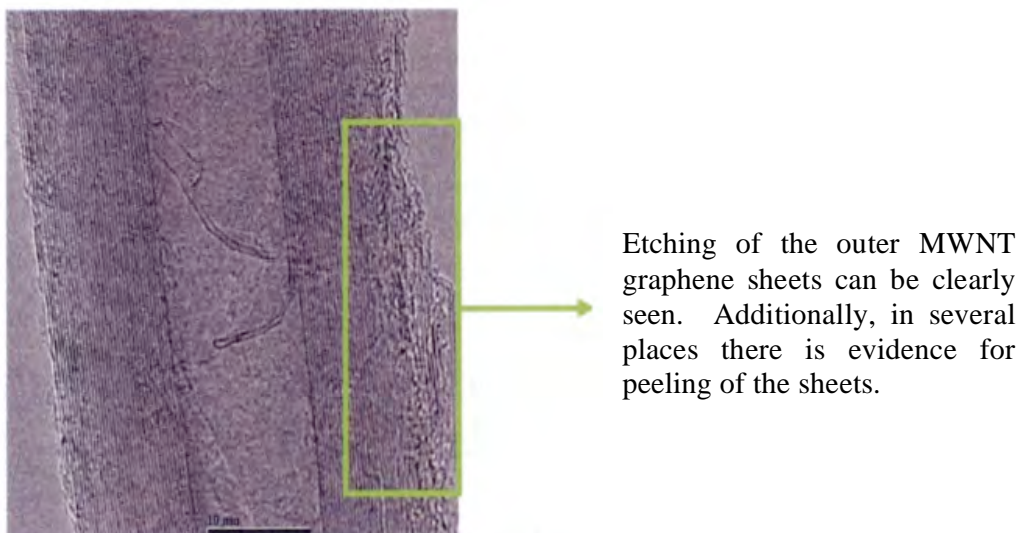


Figure 3. TEM image showing the disruption of the MWNT graphene structure as a result of acid treatment (1:1 H₂SO₄-HNO₃ reflux for 4 h).

Infrared studies were performed in order to determine which functionalities had been introduced onto the MWNTs. Figure 4 shows the Attenuated Total Reflectance Infrared (ATR IR) spectra of MWNTs activated by different acid treatments.

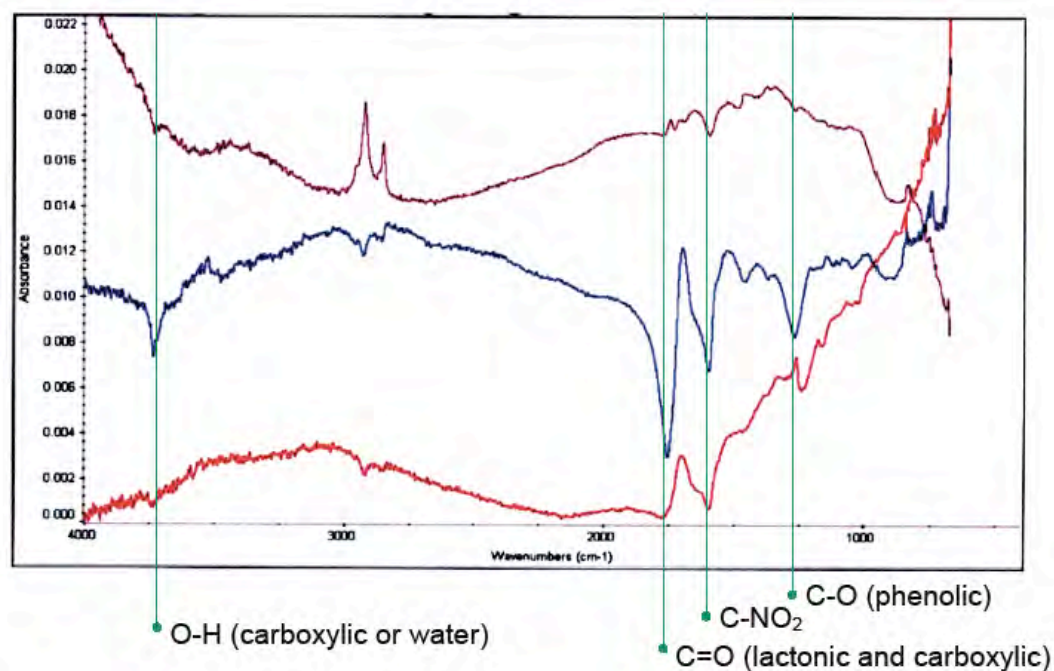


Figure 4. Background corrected ATR IR spectra of 1:1 H₂SO₄-HNO₃ treated MWNTs (top: 3 h sonication at room temperature; middle: 4 h reflux; bottom: 3 h sonication at 60 °C) showing the different functionalities introduced onto the MWNTs.

Four main peaks in the spectra can be correlated to oxygen containing functionalities introduced by the activation: the peak around 3740 cm^{-1} may be caused by the O-H stretch in a carboxylic acid functionality (although the possibility of this stretch being caused by physisorbed water cannot be discounted); the peak around 1750 cm^{-1} can be assigned to the C=O stretch in lactonic or carboxylic groups; several peaks in the $1500 - 1600\text{ cm}^{-1}$ region can be assigned to groups such as nitro, nitrito and aromatic C-C stretching; and the peak around 1260 cm^{-1} is most readily assigned to the C-O stretch in phenolic groups. It is also interesting to note that more intense peaks are observed in the sample that underwent a more aggressive activation, meaning that higher concentrations of functionalities are introduced by harsher acid treatments.

Finally, an activated carbon fiber monolith (made in house using P-200 activated Anshan fiber, with phenolic resin as the binder) was employed as the support in a reference catalyst (see Sections 3 and 4 below). This monolith, which is commercially available, was characterized using elemental analysis and N_2 physisorption. Tables 5 and 6 summarize the results of these measurements.

Table 5. Elemental analysis (by combustion) of the activated carbon fiber monolith.

Material	%C	%H	%N	%S	%O	%Ash
Carbon fiber monolith	94.99	0.61	0.8	1.21	0.68	1.71

Table 6. Physical properties of the carbon fiber monolith.

Material	BET surface area (m^2/g)	Pore volume (cm^3/g)	Mean pore radius (nm)
Carbon fiber monolith	728	0.342	0.94

The high surface area and the large pore volume shown by the activated carbon fiber monolith render it well suited for use as a catalyst support.

3. Catalyst preparation and characterization.

Catalyst preparation:

The preparation of a first set of MWNT-supported catalysts was performed using a standard literature method involving the chemical reduction of Pt salts in ethylene glycol [13], which shall be henceforth referred to as the polyol method and indicated with a letter “P” after the name of catalysts prepared by that route. In a typical preparation, aqueous solutions of Pt and a strong base (typically KOH) are mixed with ethylene glycol and the support dispersed in the resulting mixture through sonication. Heating this dispersion reduces the Pt in solution to Pt metal which deposits on the support. The product is then filtered, washed, and dried. In initial scouting experiments, two sources of heat were used: conventional heating (i.e., refluxing) and microwaves [14]. The use of microwave heating offered two main advantages: 1) it achieves excellent Pt dispersions, and 2) it reduces the reaction time from several hours to just a few minutes. However, this method was also found to have an important drawback: it yields rather inconsistent precious metal loadings. On the other hand, the use of conventional heating proved

to yield more consistent products loading-wise. Taking this important factor into account, it was decided that even though the preparation involving conventional heating is considerably more time consuming than the microwave-assisted one, the more consistent loadings achieved with conventional heating renders it the more suitable method. Nevertheless, the microwave-assisted preparations were useful to study the effect of the basification of the reaction mixture on the product, since the microwave-assisted process was also attempted without the addition of the base (following a literature report that high Pt dispersions could be obtained in the absence of base [15]).

The results of these various experiments are reported below. In the initial studies, Pt/MWNTs catalysts were prepared using both heating methods. Subsequently, these preparations were scaled up using the conventional heating route, and alloy catalysts were prepared using the same method. The catalysts synthesized included Pt, Pt-Rh, Pt-Ir and Pt-Rh-Ir on pristine MWNTs and Pt on acid activated MWNTs (all the catalysts were prepared with a target metal loading of 1 wt.%).

Further, reference catalysts, comprising Pt/Darco KB-B (Darco KB-B is a commercial, amorphous, activated carbon), Pt/Al₂O₃, and Pt/ZSM-5, were prepared using chemical reduction, standard impregnation, and ion exchange methods, respectively. However, when trying to test the Pt/Darco KB-B sample for NO reduction activity, a pressure drop was encountered over the catalyst bed which was sufficient to prevent the flow of reactants. This problem could not be solved by diluting the catalyst with glass beads and, therefore, the use of an activated carbon fiber monolith was examined as a potential solution. First, the monolith was characterized (*vide supra*) and deemed well suited for use as a catalyst support. Pt was then deposited onto the material by a method involving wet impregnation followed by H₂ reduction [16].

The preparation of a second set of MWNTs-based catalysts was also performed using wet impregnation followed by reduction with H₂. This method, henceforth to be called the impregnation method and indicated with letter "I" after the catalyst name, was examined due to the fact that, according to Inductively Coupled Plasma – Atomic Emission Spectroscopy (ICP-AES) analyses, the polyol method failed to deposit Rh and Ir on the MWNT support. Although it was eventually established that the source of this problem was of an analytical rather than a preparative nature (*vide infra*), it was decided to use the impregnation method to prepare MWNTs-based catalysts from that point on. This decision was taken due to three main factors: 1) the straightforwardness and the essentially quantitative yields of the impregnation method, 2) the promising performance of the resulting catalysts in NO reduction with propene, and 3) the lower cost of the chemicals (other than the precious metal precursors) involved.

Catalyst characterization:

ICP-AES was used for the determination of the metal loadings of the first set of catalysts prepared *via* the polyol method. In principle, metal loadings can be determined by either analyzing the filtrate from the preparation for residual metal in solution (and then calculating the loading on the catalyst by difference), or by directly analyzing the solid product after digestion in an appropriate medium (e.g., ashing the catalysts in a muffle furnace at 700 °C for one hour and then dissolving the resulting ash in aqua regia). In initial experiments, the use of both methods was investigated; while the two methods gave similar results in many cases, discrepancies were also observed. For this reason, the results from the digestion method were analyzed statistically

to determine the method's percent recovery and precision. These factors were found to be satisfactory, such that the direct method was used for the determination of metal loadings.

Table 7 shows the metal loadings determined for the scaled-up catalyst preparations.

Table 7. Precious metal loadings of the catalysts prepared via the polyol method (using conventional heating) determined by ICP-AES.

Sample	Pt (wt.%)	Rh (wt.%)	Ir (wt.%)	K (wt.%)
Pt/pristine MWNTs	0.953	N/A	N/A	Below detection
Pt-Rh/pristine MWNTs	0.358	0.230	N/A	Below detection
Pt-Ir/pristine MWNTs	0.281	N/A	0.178	Below detection
Pt-Rh-Ir/pristine MWNTs	0.177	0.112	0.119	Below detection
Pt/acid activated MWNTs	1.185	N/A	N/A	0.381

For the Pt/MWNTs catalysts, the Pt loadings were found to be within ± 0.1 wt% of the target loading of 1 wt%. However, for the Rh- and Ir-containing catalysts, metal loadings were found to be roughly half of the target loadings. At the time, the reason for this was unclear, given that it was thought that the source of the problem was preparative (as opposed to analytical) and that during the preparation Ir^{3+} should be easier to reduce than PtCl_6^{2-} (while the electrode potential of Rh^{3+} is similar to that of PtCl_6^{2-}). Therefore, an alternative route was examined for the preparation of the MWNTs-based catalysts, based on wet impregnation, followed by reduction under hydrogen [16]. In parallel, in order to investigate whether the origin of this discrepancy was of analytical or preparative nature, it was decided to submit two representative samples to an outside laboratory for analysis *via* an alternative technique, namely Proton Induced X-ray Emission Analysis (PIXE). Additionally, one of these samples was also subjected to Inductively Coupled Plasma – Mass Spectrometry (ICP-MS) for comparison purposes. The results of these analyses (presented in Table 8), show the ICP measurements to be inconsistent, while PIXE places the precious metal loadings quite close to those targeted (2.0 wt.% total metal loading).

Table 8. Elemental analysis data (in wt.%) for two catalysts prepared via the polyol analyzed by different techniques.

Catalyst	ICP-AES			ICP-MS			PIXE		
	Pt	Rh	Ir	Pt	Rh	Ir	Pt	Rh	Ir
Pt-Rh/pristine MWNTs	1.05	0.43	NA	0.937	1.42	NA	1.078	0.923	NA
Pt-Rh-Ir/pristine MWNTs	0.51	0.16	0.15	NA	NA	NA	0.775	0.797	0.745

Since both ICP techniques involve preparative steps before the actual analysis and PIXE does not, these preparative steps are believed to be the source of the observed discrepancies. Indeed, two phenomena occurring during the digestion of the catalysts might be invoked: 1) the formation of volatile oxides of Rh and Ir during the ashing of the sample, and 2) the dissolution of Pt by aqua regia being favored over that of Rh and Ir. Based on the foregoing, the elemental analysis of prepared catalysts was routinely performed in the remainder of the project using PIXE (Elemental Analysis Corp., Lexington, KY). Given that the degree in which the results of the PIXE analyses (measured loadings) differ from the targeted metal loadings (nominal

loadings) is within the analytical error (~10%), the loadings reported in this document are nominal loadings unless otherwise indicated.

In the case of the Pt/Al₂O₃ and Pt/ZSM-5 reference catalysts, the Pt loading was determined by means of X-ray Fluorescence (XRF) and found to be 1.13 wt.% and 1.0 wt%, respectively.

Another analytical problem was encountered when trying to determine precious metal dispersions. Hydrogen chemisorption is the most commonly used method for establishing mean metal particle sizes in heterogeneous catalysts. However, due to the very low density of the MWNT support materials employed, only a small amount of material could be placed in the sample vessel. This lowered the measurement accuracy, thus making H₂ chemisorption measurements alone insufficient to determine precious metal dispersion in MWNTs-based catalysts. Therefore, TEM observations were coupled to H₂ chemisorption measurements as a means to achieve this goal. TEM has one important advantage over H₂ chemisorption: whereas the latter method is only useful for determining the average metal particle size, TEM is able to provide both the average metal particle size and the metal particle size distribution of a given catalyst. On the other hand, H₂ chemisorption also has an important advantage over TEM: the former is a bulk technique, whereas the latter is only able to analyze a minuscule portion of the sample. Hence, the use of these two techniques in combination not only yields more information but also more reliable data. H₂ chemisorption results for Pt dispersion and average Pt particle size of various catalysts are shown in Table 9.

Table 9. Hydrogen chemisorption results showing the dispersion and average diameter of Pt particles on different substrates (Pt loading = 1 wt.%).

Catalyst	Pt/H-ZSM-5	Pt/Darco KB-B	Pt/pristine MWNTs	Pt/acid treated MWNTs*	Pt/Al ₂ O ₃
Dispersion (%)	67.2	66.0	11.1	83.4	56.9
Average particle diameter (nm)	1.8	2.0	10.4	1.4	2.1

* Acid treatment performed with a 1:1 mixture of H₂SO₄ and HNO₃ / 4 hour reflux.

For the reference catalysts, chemisorption experiments show good results, i.e., high dispersions, corresponding to small particles (<2.5 nm). They also show that better dispersions can be achieved using 1:1 H₂SO₄/HNO₃ treated MWNTs as the support than with the use of pristine nanotubes. This was confirmed by TEM observations (as shown in Section 5, page 29).

In the case of the Pt/Darco KB-B reference sample, Scanning Transmission Electron Microscopy measurements (STEM-Z contrast analyses) showed good agreement with the results of H₂ chemisorption, an average particle size of 2 nm being indicated by H₂ chemisorption versus particles of between 1 and 3 nm that can be seen in transmission electron micrographs (see Figure 5).

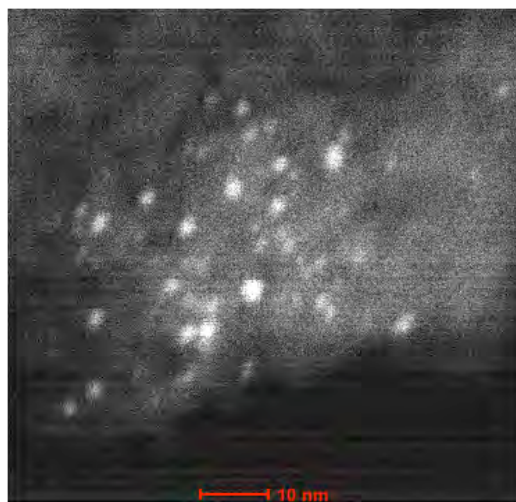


Figure 5. STEM-Z image showing Pt particles (in white) deposited on Darco KB-B.

The products of the microwave-assisted process without basification were also observed by TEM (not shown); the observed Pt dispersion was very poor, with the consequence that in all subsequent polyol preparations the basification step was employed.

Thermogravimetric analyses were performed in order to determine the thermal stability of the catalyst supports under different gas mixtures (see Figure 6 for results obtained under oxygen and Table 10 for results obtained under oxygen both in the presence and absence of NO).

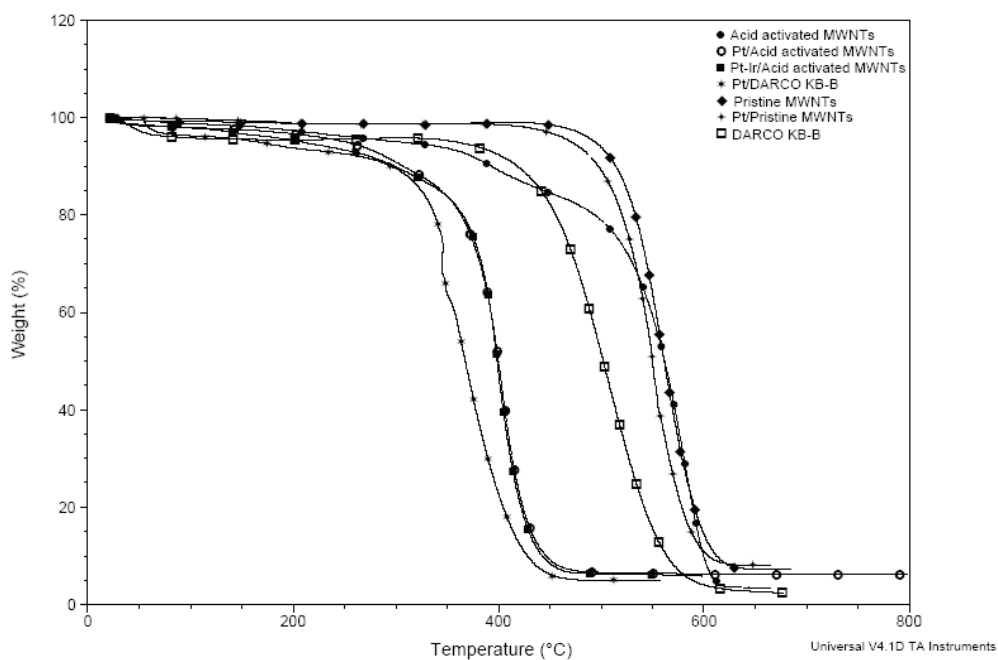


Figure 6. TGA plot of different carbon supports with and without Pt under a gas mixture of 10% O₂/balance N₂ (ramp= 5 °C/min).

Table 10. Differential thermogravimetric maxima for selected samples (measured under two different gas mixtures).

Sample	dTG max. under 10% O ₂ /balance N ₂ (°C)	dTG max. under 500 ppm NO + 9.5% O ₂ /balance N ₂ (°C)
Darco KB-B	500	520
Pristine MWNTs	560	570
Acid Treated MWNTs	565	580
Carbon fiber monolith	600	Not measured
Pt/Darco KB-B	365	380
Pt/pristine MWNTs	550	550
Pt/Acid Treated MWNTs	400	400
Pt-Ir/Acid Treated MWNTs	400	410
Pt/Carbon fiber monolith	560	Not measured

Three main trends were observed:

- 1) The Darco KB-B activated carbon support combusts at lower temperatures than the MWNTs; specifically, the differential thermogravimetric (dTG) maximum for Darco KB-B occurs at a temperature 50 °C lower than that of the MWNTs, regardless of whether NO is present in the gas mixture or not.
- 2) The activated MWNTs experience a weight loss due to decarboxylation and dehydration in the temperature range ~350-500 °C. However, combustion of the nanotubes themselves occurs at temperatures comparable to the untreated MWNTs.
- 3) Deposition of Pt and Pt alloys on the various carbon supports results in a lowering of the combustion temperature in all cases. For the activated carbon and acid activated nanotubes this effect is significant, the dTG maximum being lowered by as much as 180 °C (relative to the bare supports). Clearly, the supported Pt phase plays a major role in catalyzing the oxidation of these defect-rich supports. In the case of the untreated MWNTs, the dTG maximum was lowered by only 20 °C in the worst case, reflecting the lack of defects in the outer graphene sheets of the pristine MWNTs, and, consequently, their greater stability towards oxidation.

Given that the carbon fiber monolith showed the highest resistance to oxidation among the selected materials, its use as a carbonaceous reference support is validated. Notably, the deposition of Pt onto this support lowered its dTG maximum to a value comparable to that of Pt/pristine MWNTs. On this basis, untreated MWNTs appeared to be the support of choice, providing that an acceptable metal dispersion could be obtained.

The Pt/activated carbon fiber monolith reference catalyst was also characterized *via* PIXE, H₂ chemisorption and TEM before being tested for deNO_x activity. Both Pt loading (a nominal 2 wt.% which was confirmed by PIXE measurements) and Pt dispersion (an average Pt particle size of ~1.1 nm was measured by H₂ chemisorption) were found to be satisfactory. Unfortunately, TEM was not able to yield good micrographs since the sample preparation method proved to be rather destructive for this particular catalyst.

The characterization of the 2 wt.% Pt/Al₂O₃ reference catalyst was expanded to include H₂ chemisorption and TEM measurements. An average Pt particle size of ~1 nm was measured by means of the first technique. Although this Pt particle size could not be confirmed by means of TEM due to the poor contrast between the support and the metal, the EDS mode of the microscope was used for the chemical analysis of the material. Figure 7 shows the appearance of the sample under the microscope and the EDS spectrum of the region shown in the micrograph. Peaks corresponding to Al, O, and Pt can be observed, which confirms the presence of Al₂O₃-supported Pt.

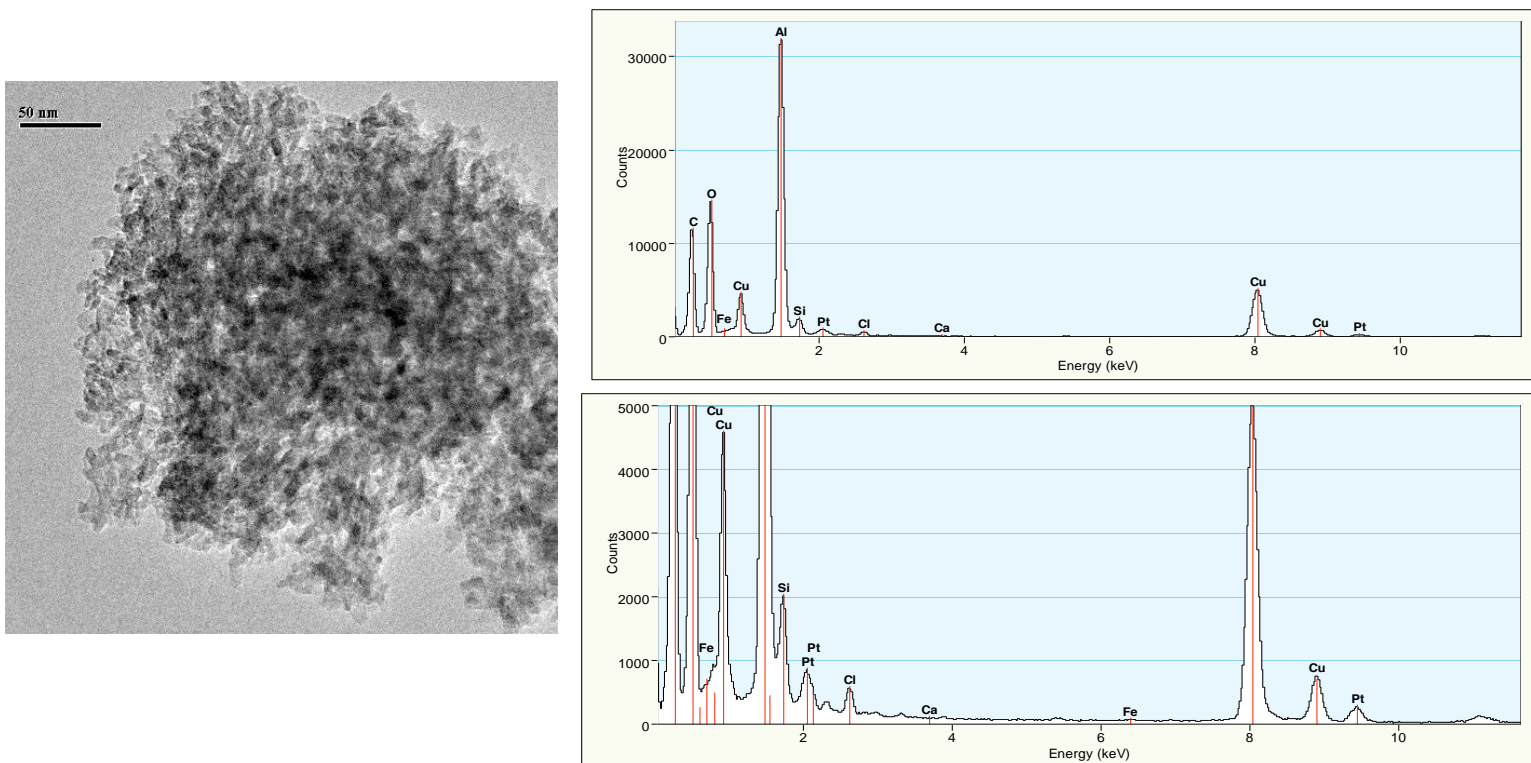


Figure 7. TEM image of Pt/Al₂O₃, corresponding EDS spectrum (top) and a close-up of the low intensity peaks in the spectrum (bottom). Cu and C peaks are due to the TEM grid

4. Catalyst screening in a microflow reactor.

Microflow reactor construction:

For the purpose of catalyst screening, a dedicated reactor was constructed. On-line analyzers were installed (for measurement of NO, NO₂, N₂O and SO₂) and mass flow controllers and analyzers calibrated. Figure 8 shows a schematic of the microflow reactor and Figure 9 is a photograph of the apparatus.

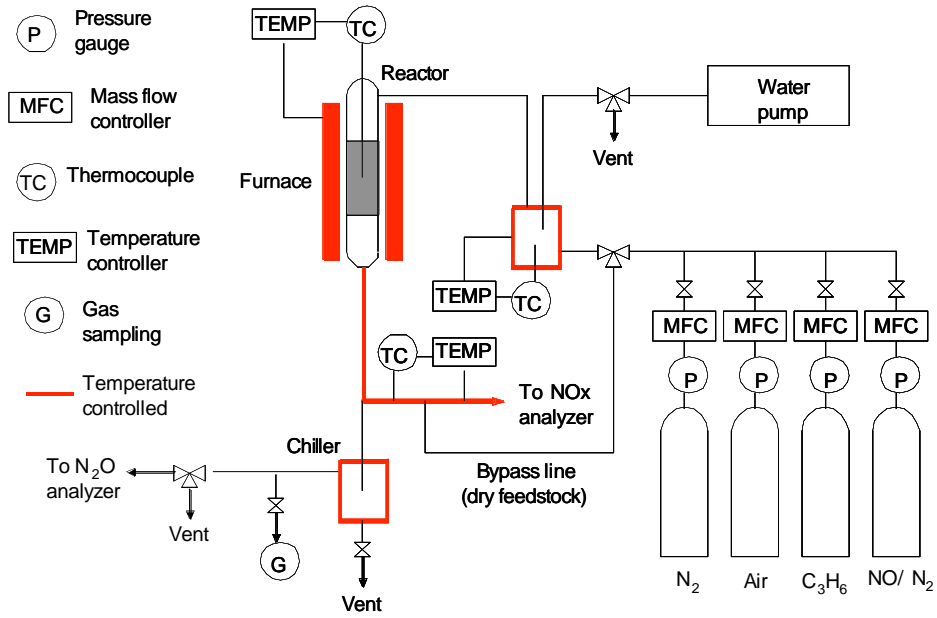


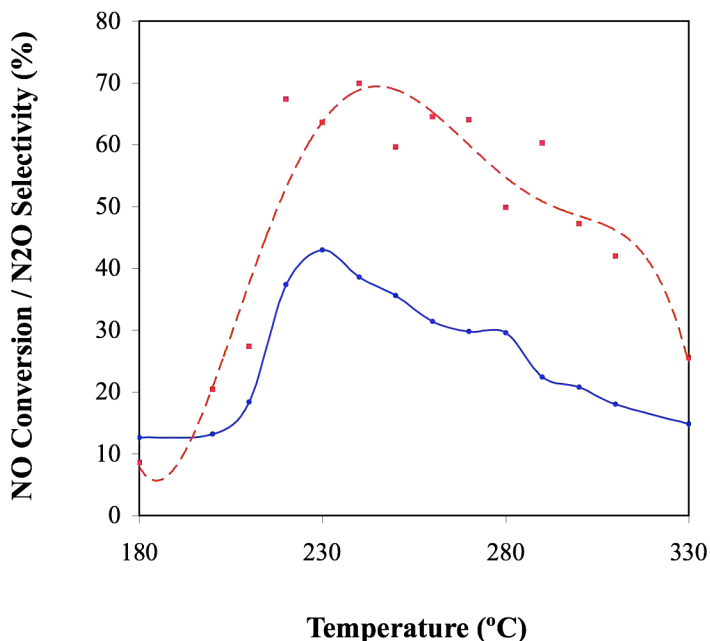
Figure 8. Reactor schematic.



Figure 9. Microflow reactor.

Catalyst screening:

The Pt/alumina reference catalyst was the first to be screened for NO reduction, using propene as the reductant. The purpose of this was two-fold: first, since the behavior of this catalyst is well known, it was used to validate the performance of the microflow reactor; second, the performance of this catalyst provided a reference against which the performance of our other catalysts could be compared. The results obtained with the reference catalyst are shown in Figure 10. Note that in this figure, and subsequent figures in this report, “NO conversion” refers to the conversion of NO to reduction products; i.e., N₂ and N₂O.



—●— NO conversion (%) 1 wt.% Pt/Al₂O₃ ···■··· Selectivity towards N₂O (%) 1 wt.% Pt/Al₂O₃

Figure 10. Plot showing the performance of 1 wt.% Pt/Al₂O₃ in NO reduction with propene. Feed composition: 500 ppm NO, 500 ppm C₃H₆, 10% O₂ and 10% H₂O, balance nitrogen. Gas flow: ca. 50,000 L gas · L cat⁻¹ · h⁻¹.

It can be seen that a maximum NO conversion of 43% is achieved at 230 °C and that at this temperature the selectivity towards N₂O is ca. 74%. These results are comparable to those reported by other workers for Pt/Al₂O₃ catalysts [17-21], albeit small differences are observed due to the differences in experimental conditions used (e.g., C₃H₆ and NO concentration, precious metal loading and gas flow).

Results for 1 wt.% Pt/fMWNTs are shown in Figure 11.

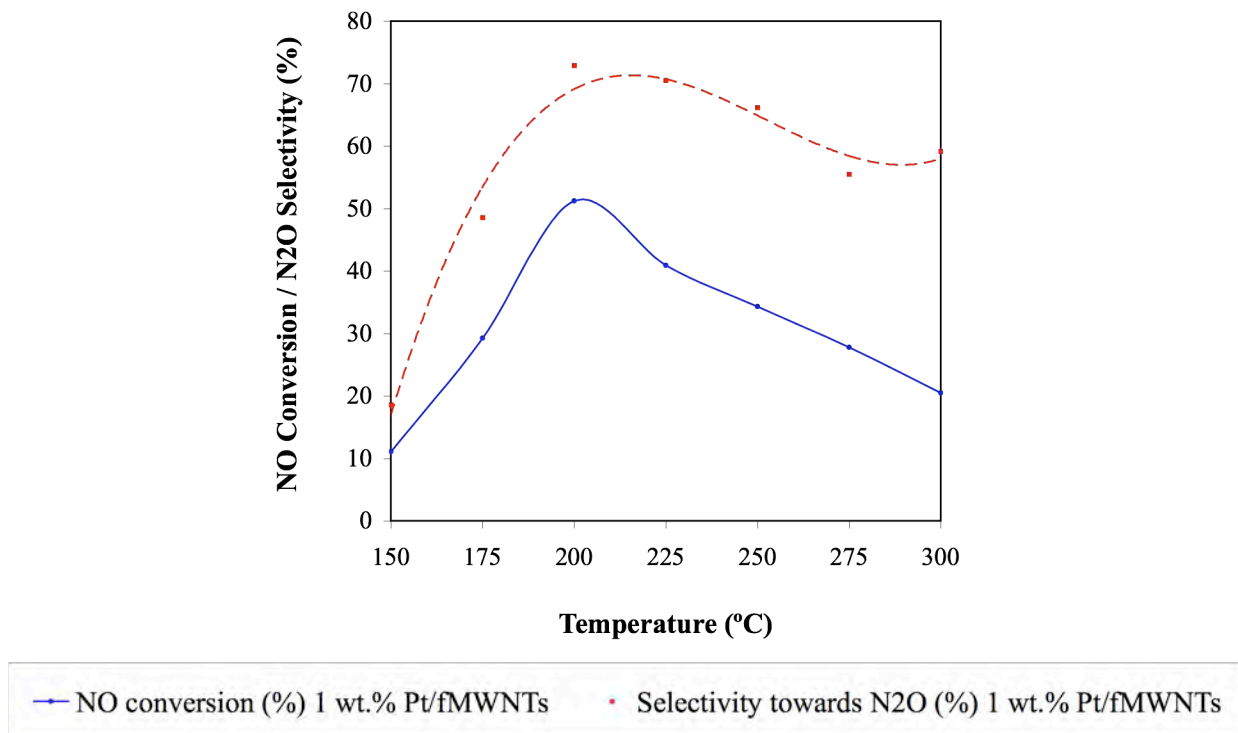


Figure 11. Plot showing the performance of 1 wt.% Pt/fMWNTs in NO reduction with propene. Feed composition: 500 ppm NO, 500 ppm C₃H₆, 10% O₂ and 10% H₂O, balance nitrogen. Gas flow: ca. 50,000 L gas · L cat⁻¹ · h⁻¹.

Relative to the Pt/Al₂O₃ reference catalyst, the Pt/activated MWNT material shows a higher peak NO conversion (50% versus 43%), while the temperature corresponding to this maximum is shifted towards lower temperature (~200 °C versus ~230 °C). These findings support previous reports [22, 23] suggesting that Pt/C catalysts are more active for NO reduction than Pt supported on metal oxides. Consideration of the selectivity to N₂O reveals that the Pt/activated MWNT and Pt/Al₂O₃ catalysts show near identical behavior, suggesting that the support has little or no influence on product selectivity (i.e., N₂ or N₂O).

Consideration of the data for a 0.35 wt.% Pt - 0.25 wt.% Rh/MWNTs catalyst (plot not shown) revealed several significant findings. Firstly, the maximum NO conversion level (21%) was found to be significantly lower than for the above Pt catalysts, while the temperature corresponding to the maximum was shifted to ≥ 325 °C. The low activity of this catalyst was not unexpected, given the low metal loading. However, the large shift in the temperature window for activity appeared to be associated with the presence of Rh. Secondly, the selectivity to N₂, as opposed to N₂O, appears to be far superior to that of the monometallic Pt catalysts. This was an encouraging result, albeit that it needed to be confirmed at higher NO conversion levels. To this end, work was aimed at preparing Pt and alloy catalysts with higher total metal loadings (2 wt.%), so as to allow a more accurate comparison (see Section 5 below). In turn, reference catalysts with loadings comparable to those of the new MWNTs-based catalysts were prepared and tested. Figure 12 shows the behavior of the 2 wt.% Pt/activated carbon fibers reference catalyst in NO reduction with propene and compares it to that of the 2 wt.% Pt/Al₂O₃ material.

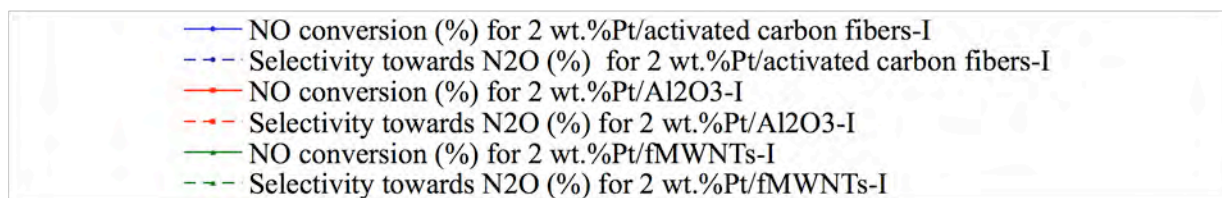
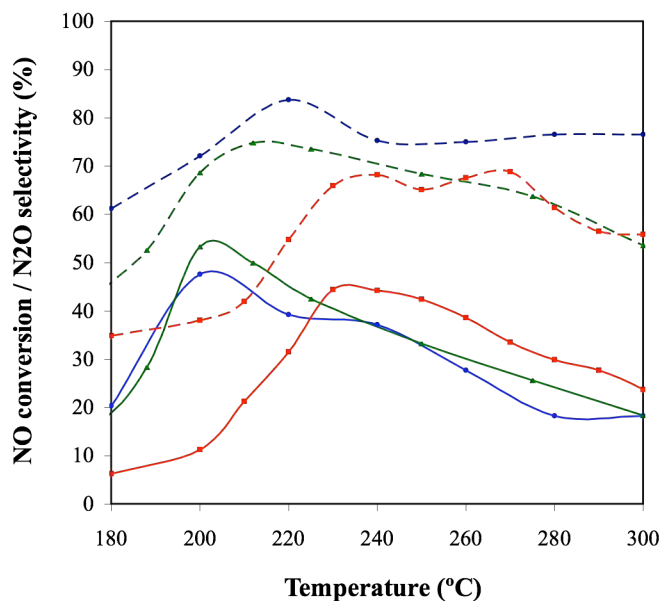


Figure 12. Combined plot comparing the performance of 2 wt. % Pt/fMWNTs-I with that of 2 wt.% Pt/activated carbon fibers-I with and 2 wt.% Pt/Al₂O₃-I reference catalysts in NO reduction with propene. Feed composition: 500 ppm NO, 500 ppm C₃H₆, 10% O₂ and 10% H₂O, balance nitrogen. Gas flow: ca. 50,000 L gas · L cat⁻¹ · h⁻¹.

From Figure 12, it can be seen that both reference catalysts show a similar maximum NO conversion of ca. 45%. However, there are three main differences in the performance of Pt/activated carbon fibers with respect to that of Pt/Al₂O₃: 1) a lower temperature of maximum NO conversion (~25 °C lower), 2) a wider deNO_x temperature window, and 3) a higher selectivity towards N₂O. The figure also shows the activity of Pt/fMWNTs to be superior to that of both reference catalysts. Given that both reference catalysts and the fMWNTs-based catalyst share the same Pt loading and dispersion, these differences in activity can only be attributed to a catalyst support effect. This observation is particularly interesting, given that the influence of the support on lean NO_x HC-SCR finds both supporters [24-27] and detractors [28-30] in the scientific literature. Nevertheless, an important body of work supports the idea that catalytic behavior depends, at least to some extent, on the nature of the support, since a degree of support acidity has been found to improve deNO_x activity and/or N₂-selectivity [22, 25,31-37], particularly when using alkanes as reductant. In other words, the higher activity of the carbon-based catalysts in comparison with Pt/Al₂O₃ may be a consequence of the higher acidity of these supports. An additional possibility is that the oxidation state of the Pt plays a role in determining catalyst activity and selectivity, Pt supported on carbon likely being in a more reduced state than Pt supported on an oxide such as alumina. Given that dissociative adsorption of NO on Pt is

thought to be one of the main pathways for NO reduction in the presence of propene [26,27], and that a metallic surface, largely free of adsorbed oxygen, should be able to adsorb and dissociate NO more effectively than an oxidic Pt surface, Pt supported on carbon can be expected to be more active in NO reduction than Pt/Al₂O₃. In order to probe this hypothesis, X-ray Photoelectron Spectroscopy (XPS) studies aimed at investigating the oxidation state in these two types of catalyst were planned. These and other *in situ* spectroscopic studies (Task 6 within this project) were carried out in parallel to the optimization of MWNTs-based catalysts (Task 5). However, in the present report, the order in which the results of such tasks are presented is reversed to enhance the readability of the document.

5. Catalyst optimization.

Experiments were performed in order to determine which support material (pristine nanotubes or functionalized nanotubes), catalyst preparation method, and metal or combination of metals yields catalysts with the best performance; i.e., high deNO_x activity over a wide temperature window accompanied by high selectivity towards N₂. This was done by sequentially changing these variables and studying the effect on catalyst performance.

Effect of the catalyst support:

First, 2 wt.% Pt/MWNTs and 2 wt.% Pt/fMWNTs catalysts were prepared *via* wet impregnation followed by reduction with H₂ [16]. PIXE analysis confirmed the nominal Pt loadings of both catalysts. Subsequently, the samples were tested in a microflow reactor to determine their deNO_x performance. The feed composition was 500 ppm NO, 500 ppm C₃H₆, 10% O₂ and 10% H₂O, the balance gas being nitrogen. A gas flow corresponding to ca. 50,000 L gas · L cat⁻¹ · h⁻¹ was used. Figure 13 compares the performance of these two catalysts.

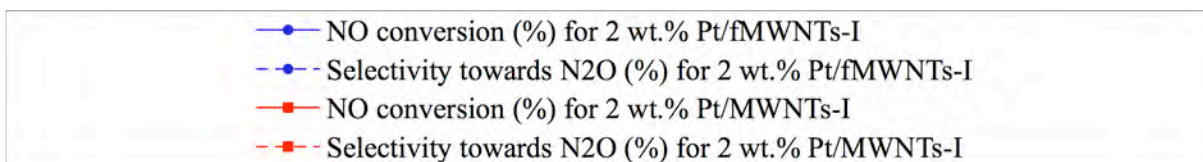
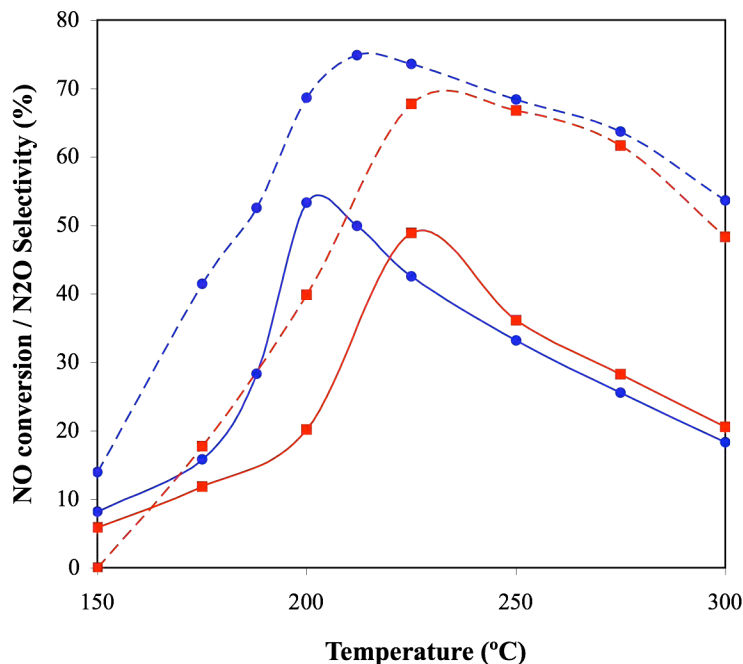


Figure 13. Combined plot comparing the performance of Pt/MWNTs-I with that of Pt/fMWNTs-I in NO reduction with propene. Feed composition: 500 ppm NO, 500 ppm C₃H₆, 10% O₂ and 10% H₂O, balance nitrogen. Gas flow: ca. 50,000 L gas · L cat⁻¹ · h⁻¹.

Evidently, the support does not have an appreciable impact on either the maximum deNO_x activity or on the selectivity towards N₂ shown by the catalysts. However, the use of fMWNTs as a catalyst support does have two effects: 1) it shifts the maximum NO conversion towards lower temperatures (*ca.* 30 °C) relative to the Pt/MWNTs catalyst; and 2) it slightly widens the deNO_x temperature window. It is interesting to note that for bi-metallic catalysts (not shown), this temperature shift is even more accentuated (*ca.* 50 °C).

Effect of the catalyst preparation method:

Having established the favorable properties of fMWNTs as a catalyst support, Pt was deposited onto fMWNTs *via* the polyol method [38], in order to study the effect of the preparation method on catalyst performance. The nominal 2 wt.% Pt loading of the resulting catalyst was confirmed by PIXE analysis. Figure 14 compares the performance of the 2 wt.% Pt/fMWNTs catalysts prepared by the two different methods. The only difference seems to lie in the temperature of the maximum NO conversion, which is *ca.* 20 °C lower for the catalyst prepared by impregnation. Shifts of similar magnitude can also be observed for the bi-metallic catalysts (not shown). Figure 14 also compares the performance of catalysts prepared by the impregnation method using different supports (pristine MWNTs vs. fMWNTs).

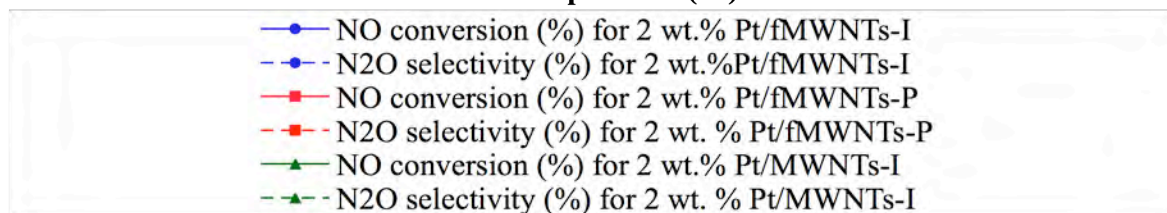
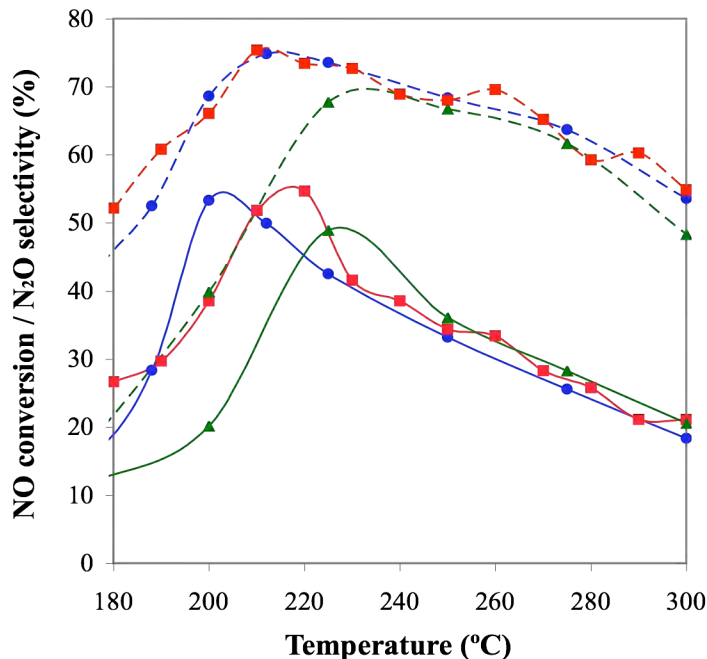


Figure 14. Combined plot comparing the performance of 2 wt.% Pt/fMWNTs-I, 2 wt.% Pt/fMWNTs-P and 2 wt.% Pt/MWNTs-I in NO reduction with propene. Feed composition: 500 ppm NO, 500 ppm C₃H₆, 10% O₂ and 10% H₂O, balance nitrogen. Gas flow: ca. 50,000 L gas · L cat⁻¹ · h⁻¹.

Experiments were then performed in order to understand why the use of fMWNTs as the catalyst support and impregnation as the catalyst preparation method yield catalysts with improved NO_x reduction performance. The particle size distributions of representative catalysts were determined by measuring the diameter of 200 particles from micrographs obtained with a Transmission Electron Microscope. Figure 15 shows the particle size distribution histograms of the catalysts.

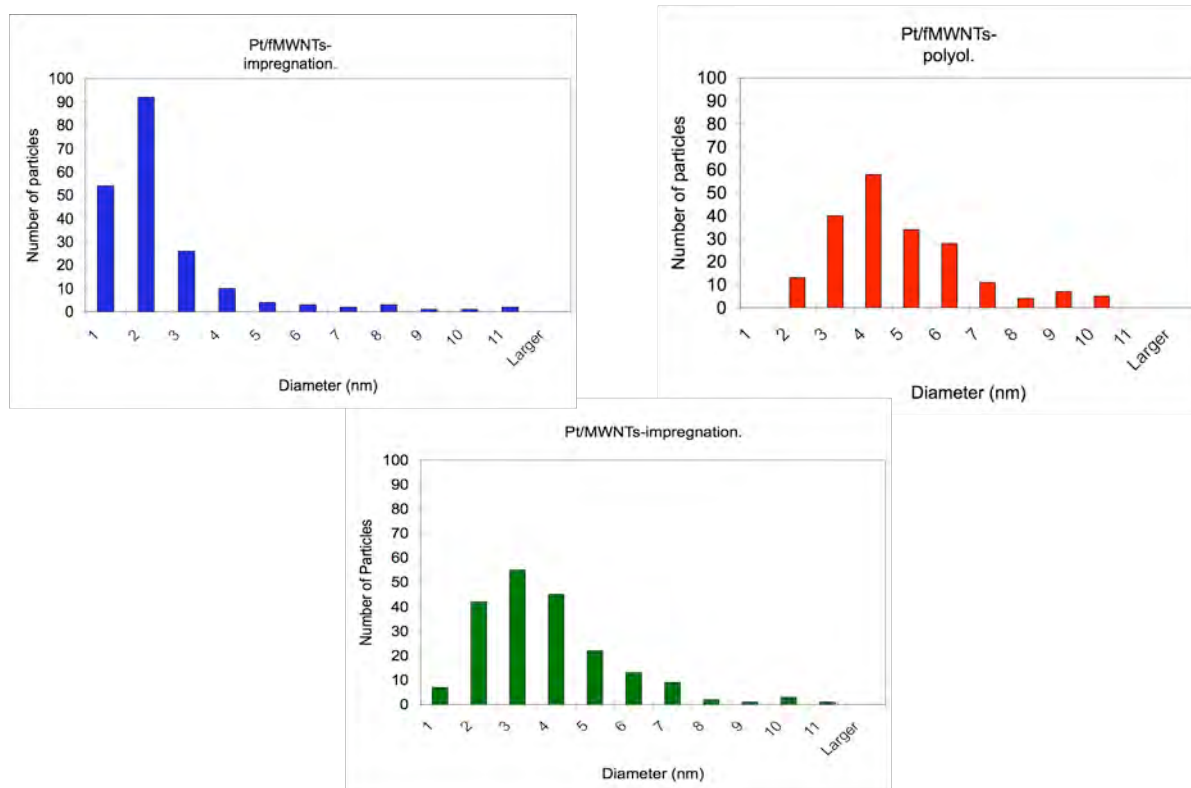


Figure 15. Particle size distribution histograms of 2 wt.% Pt/fMWNTs-I, 2 wt.% Pt/fMWNTs-P and 2 wt.% Pt/MWNTs-I (200 particles measured per histogram).

Two conclusions can be drawn from Figures 14 and 15: 1) the use of fMWNTs as the support and impregnation as the preparation method yields catalysts with higher metal dispersions than those obtained using pristine MWNTs and the polyol method, and 2) although the catalyst with the highest Pt dispersion is the most active, there does not appear to be a direct correlation between metal dispersion and catalyst performance. This last point is particularly interesting, since there is an on-going debate regarding the effect of Pt dispersion on the performance of Pt catalysts. While some authors find no correlation between Pt dispersion and NO_x reduction performance [22,23,39,40], other authors propose that Pt dispersion has a noticeable influence on deNO_x activity and/or N_2 -selectivity [27,40-43]. Further, it seems that the extent of such influence depends on both the nature of the support and the reaction under study (propene oxidation, NO oxidation, NO dissociation or NO reduction) [42,44-47]. In order to probe the extent of this influence in MWNT-supported catalysts, STEM and XPS experiments were performed (see Section 6 below).

Finally, inspired by a recent report in the literature dealing with the removal of oxidation debris from acid-treated MWNTs [48], we decided to investigate the effect of a base washing step on the functionalized multi-walled nanotubes (fMWNTs). Acid treatment of MWNTs was performed in order to produce fMWNTs, which were then suspended in 0.01 M NaOH *via* sonication. This suspension was then centrifuged and the supernatant was decanted. The solid was next re-suspended in de-ionized water, centrifuged and decanted. A wash with 0.01 M HCl,

followed by a final wash with de-ionized water, was performed before allowing the product (denoted hereafter bfMWNTs) to dry in a vacuum oven. Both the fMWNTs used as starting material and the bfMWNTs product were characterized by means of TEM and TGA. Figure 16 shows representative micrographs of these two materials.

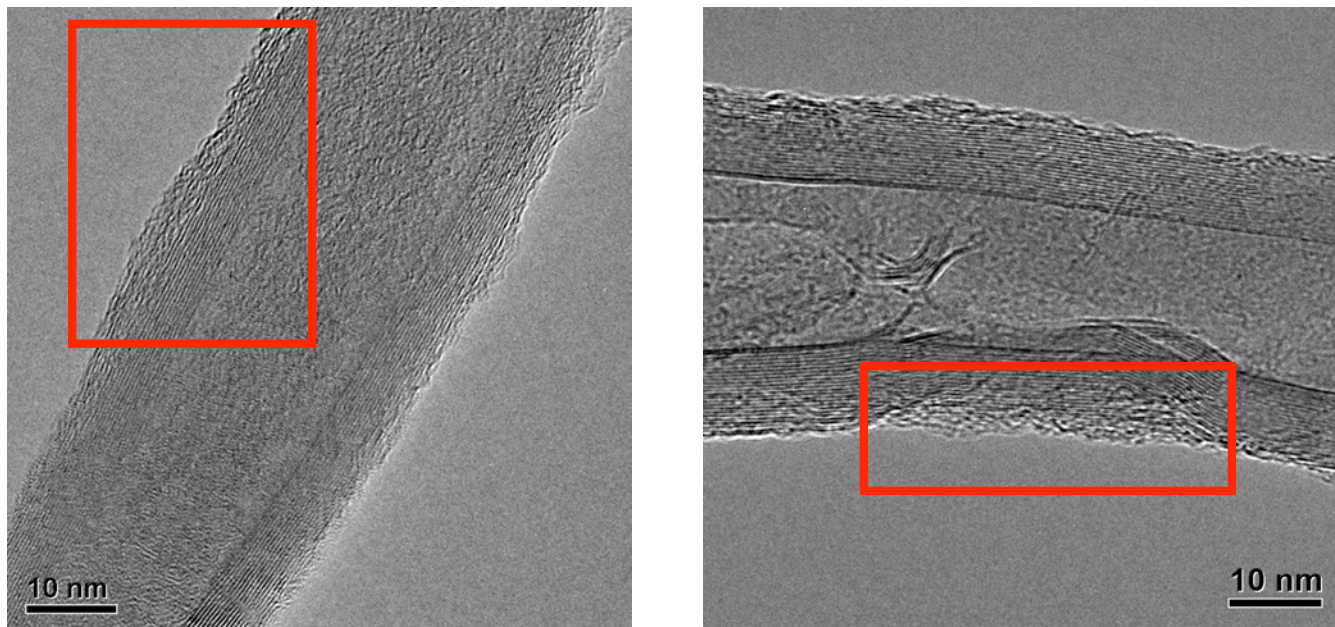


Figure 16. TEM micrographs of fMWNTs (left) and bfMWNTs (right) with oxidation debris highlighted by the red rectangles.

It appears to be the case that the amount of residual oxidation debris is lessened by the base washing step. However, as the highlighted region of the micrograph of a bfMWNT shows, the produced material is not debris-free. Given that TEM is not a bulk technique, TGA experiments were performed in which both fMWNTs and bfMWNTs were combusted under an atmosphere of 10% O₂ (balance N₂) using a temperature ramp of 5 °C/min. The resulting plots are shown in Figure 17.

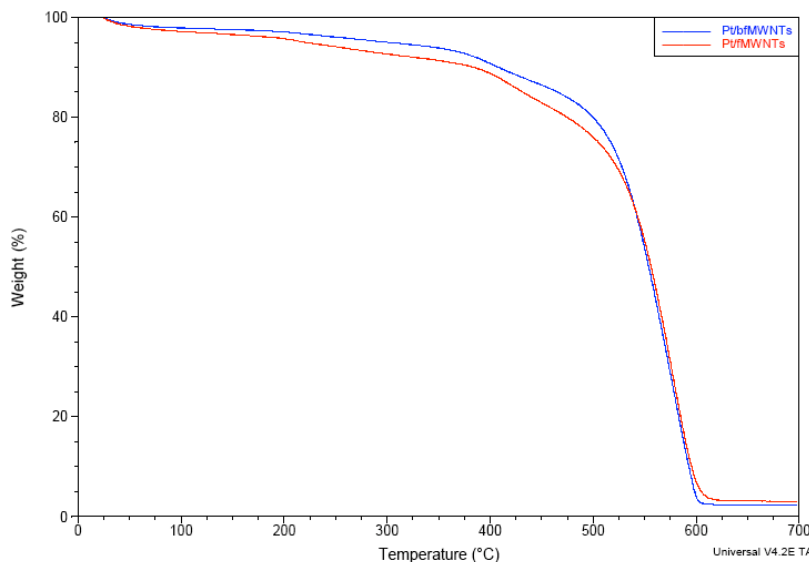


Figure 17. Combined TGA plot for fMWNTs and bfMWNTs under an atmosphere of 10% O₂ (balance N₂). Ramp = 5 °C/min.

From the figure, it is apparent that some of the oxidation debris, which is combusted at relatively low temperatures compared to the actual MWNTs, is successfully removed by the base wash. Elemental analysis of fMWNTs and bfMWNTs, shown in Table 11, appears consistent with this conclusion.

Table 11. Elemental analysis (by combustion) of fMWNTs and bfMWNTs.

Material	Ash (%)	Moisture (%)	Carbon (%)	Hydrogen (%)	Nitrogen (%)	Oxygen (%)
fMWNTs	1.13	3.09	85.66	0.62	0.22	12.37
bfMWNTs	2.41	1.68	87.97	0.51	0.28	8.83

As can be seen from the table, there is a significantly lower oxygen content in the base-washed material, which further points to the successful removal of highly functionalized matter from the surface of the fMWNTs.

In order to determine the effect on precious metal deposition of removing oxidation debris, and the effect on the performance of the resulting catalyst, both a 2 wt.% Pt/fMWNTs catalyst and a 2 wt.% Pt/bfMWNTs catalyst were prepared, characterized, and screened for activity in NO reduction with propene. As can be seen in Figure 18, which compares the particle size distribution of these two catalysts, the base wash of the support seems to have no effect on the particle size obtained after Pt deposition.

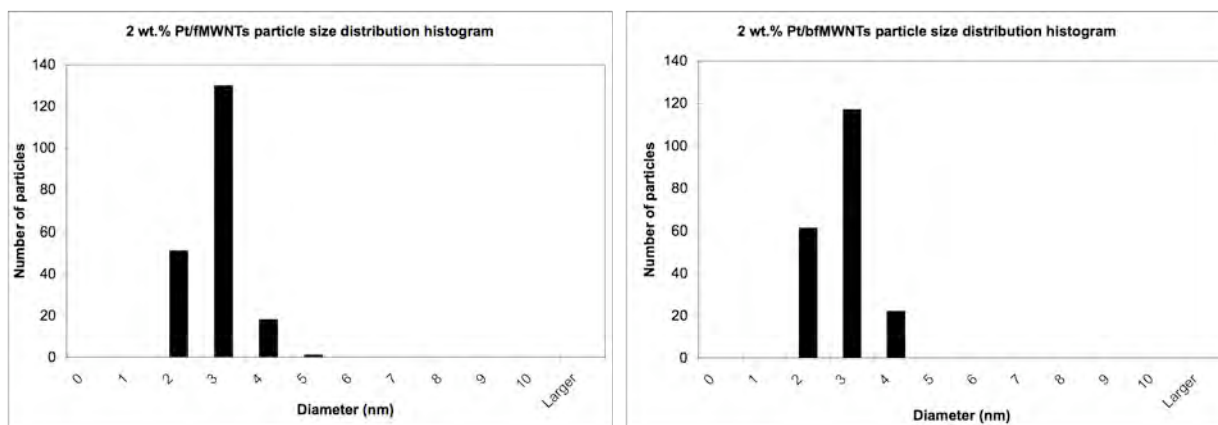


Figure 18. Particle size distribution histograms for 2 wt.% Pt/fMWNTs (left) and 2 wt.% Pt/bfMWNTs (right) (200 particles measured per histogram).

This result, combined with the conclusions drawn from the elemental analyses, suggests that after removal of the oxidation debris, the concentration of surface groups (mainly $-\text{COOH}$ and $-\text{OH}$) remains sufficient to ensure that a high metal dispersion is obtained.

In order to determine the effect of removing the oxidation debris on the performance of the resulting catalyst, a 2 wt.% Pt/bfMWNTs catalyst was screened for activity in NO reduction with propene, as well as a 2 wt.% Pt/fMWNTs catalyst for comparison purposes. Figure 19 compares the performance of these two catalysts.

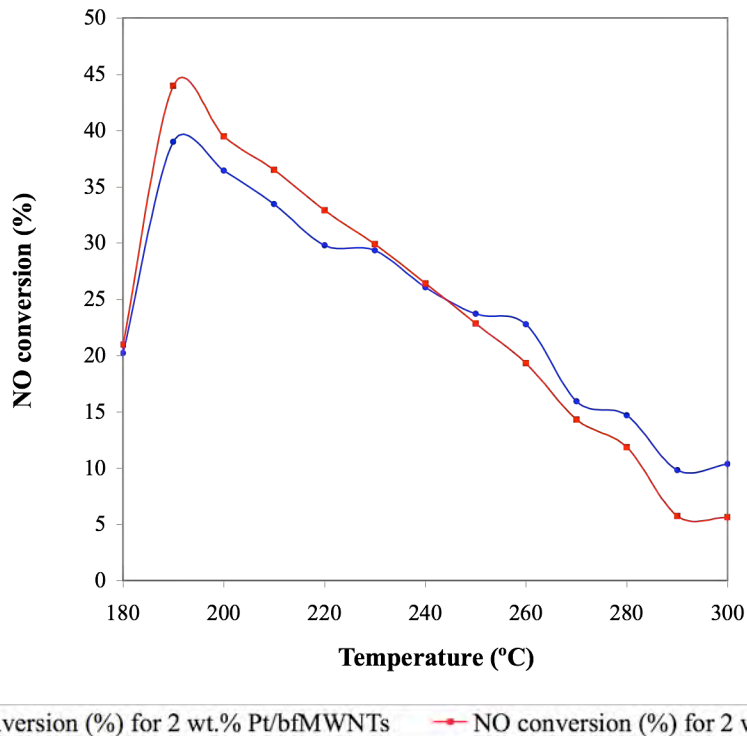


Figure 19. Combined plot comparing the performance of 2 wt.% Pt/fMWNTs with that of 2 wt.% Pt/bfMWNTs in NO reduction with propene. Feed composition: 500 ppm NO, 500 ppm C₃H₆, 10% O₂ and 10% H₂O, balance nitrogen. Gas flow: ca. 50,000 L gas · L cat⁻¹ · h⁻¹.

From these results, it is apparent that both catalysts show fairly similar deNO_x activities and the same can be said with respect to the selectivity towards N₂O (not shown). This is to be expected, given that the characterization of these catalysts revealed no significant differences between them.

Effect of the reductant concentration:

Experiments were performed in order to determine the effect of the propene concentration on catalyst performance. Figure 20 is a combined plot comparing the performance of a 2 wt.% Pt/fMWNTs-P catalyst under different propene:NO ratios.

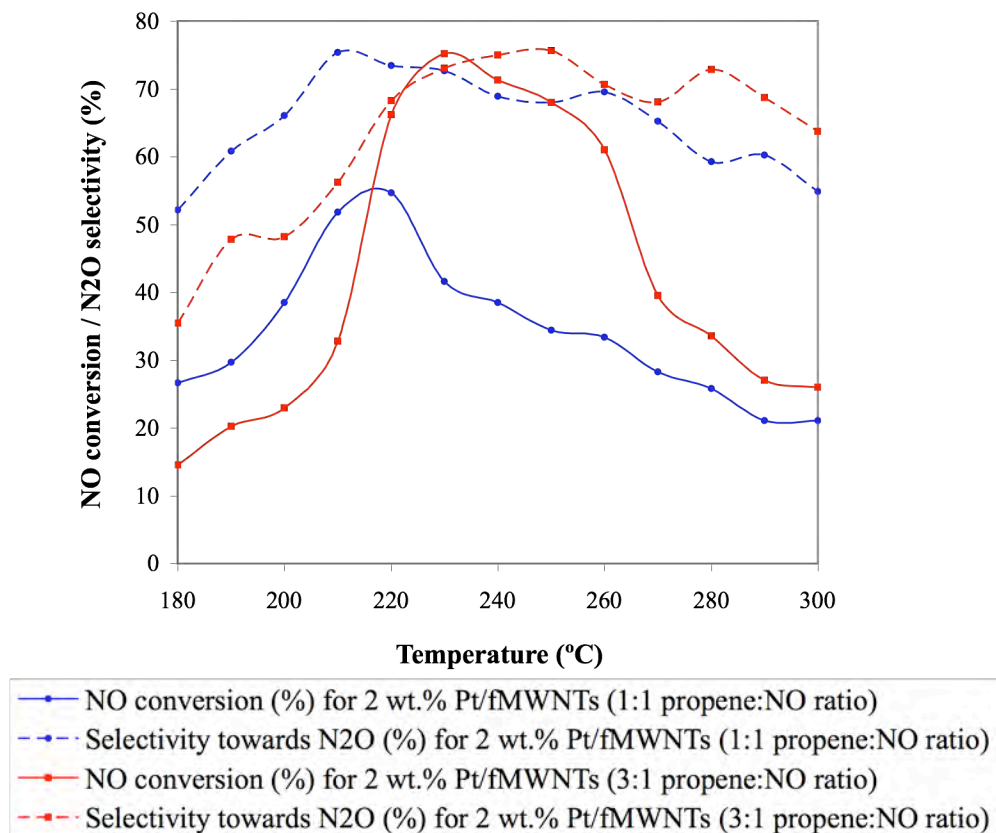


Figure 20. Combined plot comparing the performance of 2 wt.% Pt/fMWNTs in NO reduction with propene under different propene:NO ratios. Feed composition: 500 ppm NO, 500 or 1500 ppm C₃H₆, 10% O₂ and 10% H₂O, balance nitrogen. Gas flow: ca. 50,000 L gas · L cat⁻¹ · h⁻¹.

It can be clearly observed that although the selectivity is almost totally independent of the propene concentration, the deNO_x activity increases considerably upon changing the propene:NO mole ratio from 1:1 to 3:1. This effect is not unexpected, given that NO reduction by propene competes with the total oxidation of the latter by oxygen. Therefore, any increase in propene concentration should lead to a higher amount of propene available for NO reduction. Simultaneously, the deNO_x activity also shows a slight temperature shift toward higher temperatures (ca. 10 °C).

Effect of promotion with Rh and/or Ir:

In addition to Pt, bimetallic Pt-containing catalysts of the type Pt-Rh [1,2] and Pt-Ir [3-6] have been reported to be active in NO_x reduction with hydrocarbons. With this in mind, and taking into account our findings regarding the effects of the catalyst support and the catalyst preparation method on deNO_x performance, Pt/fMWNTs, Pt-Rh/fMWNTs and Pt-Ir/fMWNTs catalysts with 2 wt.% total metal loading were prepared *via* impregnation. Figure 21, which compares the performance of these three formulations, illustrates how the monometallic catalyst shows a higher NO conversion than the bimetallic preparations.

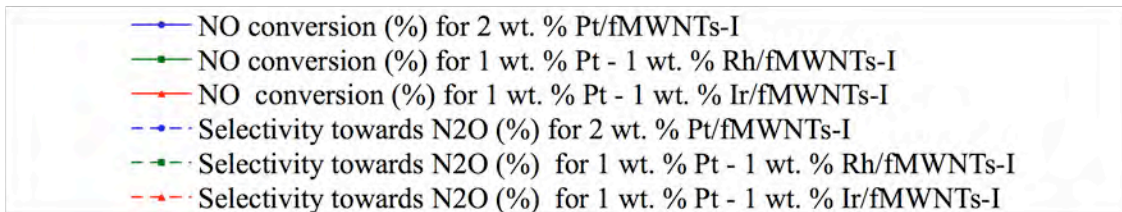
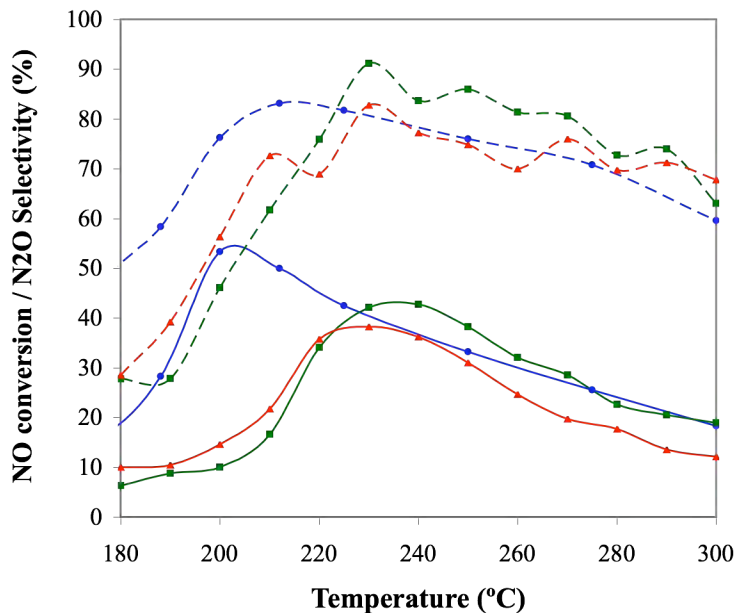
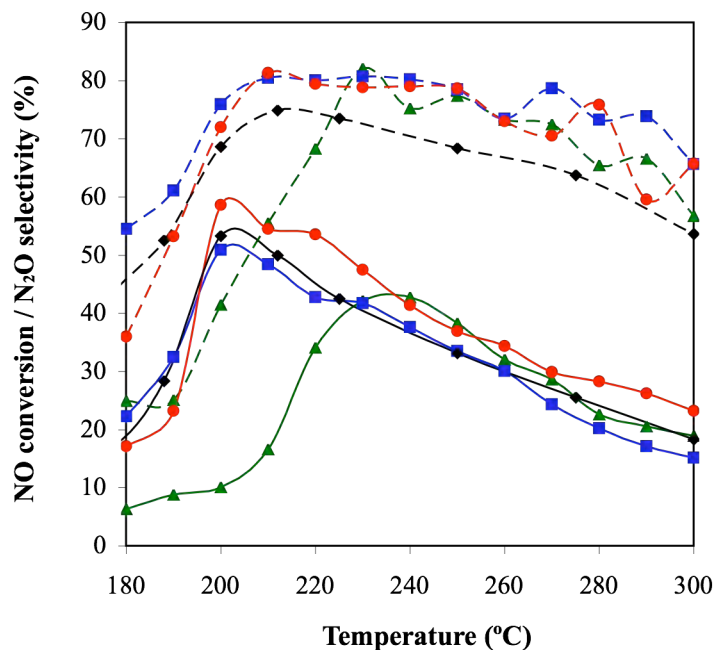


Figure 21. Combined plot comparing the performance of 2 wt.% Pt/fMWNTs-I, 1 wt.% Pt – 1 wt.% Rh/fMWNTs-I and 1 wt. % Pt – 1 wt.% Ir/fMWNTs-I in NO reduction with propene. Feed composition: 500 ppm NO, 500 ppm C₃H₆, 10% O₂ and 10% H₂O, balance nitrogen. Gas flow: ca. 50,000 L gas · L cat⁻¹ · h⁻¹.

Additionally, the temperature at which the monometallic catalyst shows its maximum activity is *ca.* 30 °C lower than that of the bimetallic catalysts and *ca.* 50 °C lower than that of a trimetallic preparation (not shown). Further, given that the same trends were observed when the formulations were prepared by the polyol method or when pristine MWNTs were used as catalyst support, this behavior is clearly metal-dependent.

While the Pt-Rh/fMWNTs catalyst represents the bimetallic formulation with the best NO reduction activity, its performance is inferior to that of the corresponding Pt-only catalyst. However, since all our bimetallic formulations had been prepared aiming for a 1:1 weight ratio between the two metallic components, the effect of the metal ratio on deNO_x activity was of interest. A loading study was performed in which two Pt rich Pt-Rh catalysts with a 2 wt.% total metal loading were prepared using fMWNTs as the support and impregnation as the preparation method. One of these catalysts had a 3:1 Pt to Rh weight ratio, while in the other these metals were in a 9:1 proportion. Figure 22 compares the deNO_x activity of the Pt-Rh catalysts with that of the corresponding Pt-only catalyst.



- ▲— NO conversion (%) for 1 wt.% Pt - 1 wt.% Rh/fMWNTs-I
- -▲- - N2O selectivity (%) for 1.0 wt. % Pt - 1.0 wt. % Rh/fMWNTs-I
- NO conversion (%) for 1.8 wt.% Pt - 0.2 wt.% Rh/fMWNTs-I
- -■- - N2O selectivity (%) for 1.8 wt. % Pt - 0.2 wt. % Rh/fMWNTs-I
- NO conversion (%) for 1.5 wt.% Pt - 0.5 wt.% Rh/fMWNTs-I
- -●- - N2O selectivity (%) for 1.5 wt. % Pt - 0.5 wt. % Rh/fMWNTs-I
- ◆— NO conversion (%) for 2 wt.% Pt/fMWNTs-I
- -◆- - N2O selectivity (%) for 2.0 wt. % Pt/fMWNTs-I

Figure 22. Combined plot comparing the performance of Pt/fMWNTs-I to that of Pt-Rh/fMWNTs-I with different Pt:Rh ratios in NO reduction with propene. Feed composition: 500 ppm NO, 500 ppm C₃H₆, 10% O₂ and 10% H₂O, balance nitrogen. Gas flow: ca. 50,000 L gas · L cat⁻¹ · h⁻¹.

From this figure, it is apparent that the catalyst with a 3:1 Pt:Rh ratio shows improved behavior compared to that of the Pt-only catalyst and represents the most active formulation prepared in the project. Table 12 summarizes and compares the reactor data for selected Pt-only and Pt-Rh catalysts.

Table 12. NO conversion data for selected Pt and Pt-Rh catalysts.

Catalyst ¹	Temp. of max. NO conversion T_{\max} (°C)	Conversion to N ₂ at T_{\max} (%)	Conversion to N ₂ O at T_{\max} (%)	Conversion to NO ₂ at T_{\max} (%)	NO conversion FWHM ² (°C)	TOF ³ (10 ⁻³ s ⁻¹)
Pt/MWNTs-I	225	30.5	18.4	4.0	75.0	8.9
Pt/fMWNTs-I	205	33.0	20.4	1.7	80.0	6.8
Pt/fMWNTs-P	220	32.4	22.3	17.4	87.0	13.0
1:1 Pt-Rh/fMWNTs-I	235	24.9	17.9	0.8	65.0	5.6
3:1 Pt-Rh/fMWNTs-I	200	35.2	23.4	1.4	75.0	7.9
9:1 Pt-Rh/fMWNTs-I	200	28.4	21.5	7.6	85.0	6.6

¹2.0 wt.% total metal loading for each catalyst.

²Full Width at Half Maximum.

³Turn Over Frequency defined as the number of NO molecules converted to N₂ and N₂O per surface precious metal atom per second.

It is important to note that the turnover frequencies (TOFs) reported in this table were calculated using the median particle diameter of particles observable under TEM (>1 nm). Since the existence of sub-nanometer particles has been proven by means of STEM (see below) and all of the calculated TOFs fall within a very narrow range, these values should be approached with caution.

Figure 23 shows the particle size distribution histograms of the three Pt-Rh catalysts. These histograms were built and compared in order to determine whether catalyst performance was influenced by particle size.

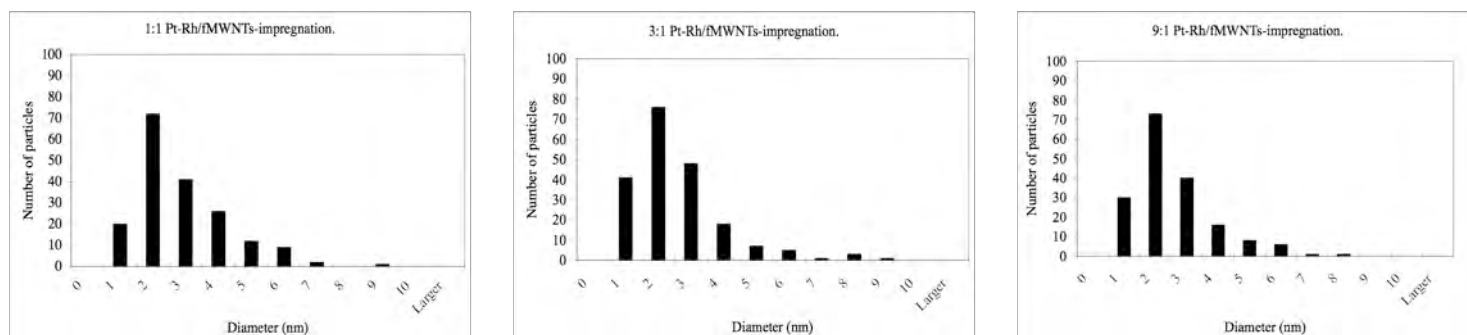


Figure 23. Particle size distribution histograms for 1.0 wt.% Pt – 1.0 wt.% Rh/fMWNTs-I (left), 1.5 wt.% Pt – 0.5 wt.% Rh/fMWNTs-I (center) and 1.8 wt.% Pt – 0.2 wt.% Rh/fMWNTs-I (right) (200 particles measured per histogram).

In all three cases, the particle size distribution was centered on particles between 2 and 3 nm in diameter and, in general, the histograms look quite similar. This suggests that the deNO_x activity of Pt-Rh/fMWNTs catalysts depends largely on the ratio in which the metals are present (without totally ruling out the influence of the metal dispersion on catalytic activity). This observation is consistent with a literature report, in which a 0.75 wt.% Pt – 0.25 wt.% Rh/Al₂O₃ catalyst was found to show the highest activity for NO conversion (~60% at 250 °C) in a series of Pt-Rh catalysts with different Pt:Rh ratios [49]. However, this reference also reports an improvement in N₂ selectivity for the 3:1 Pt-Rh catalyst compared to that of the corresponding Pt-only formulation; such an improvement is not observed in our fMWNTs-based catalysts.

Finally, Figure 24 shows the particle size distribution histograms of the 2 wt.% Pt/fMWNTs-I and the 1.5 wt.% Pt – 0.5 wt.% Rh/fMWNTs-I catalysts both before and after these catalysts were screened.

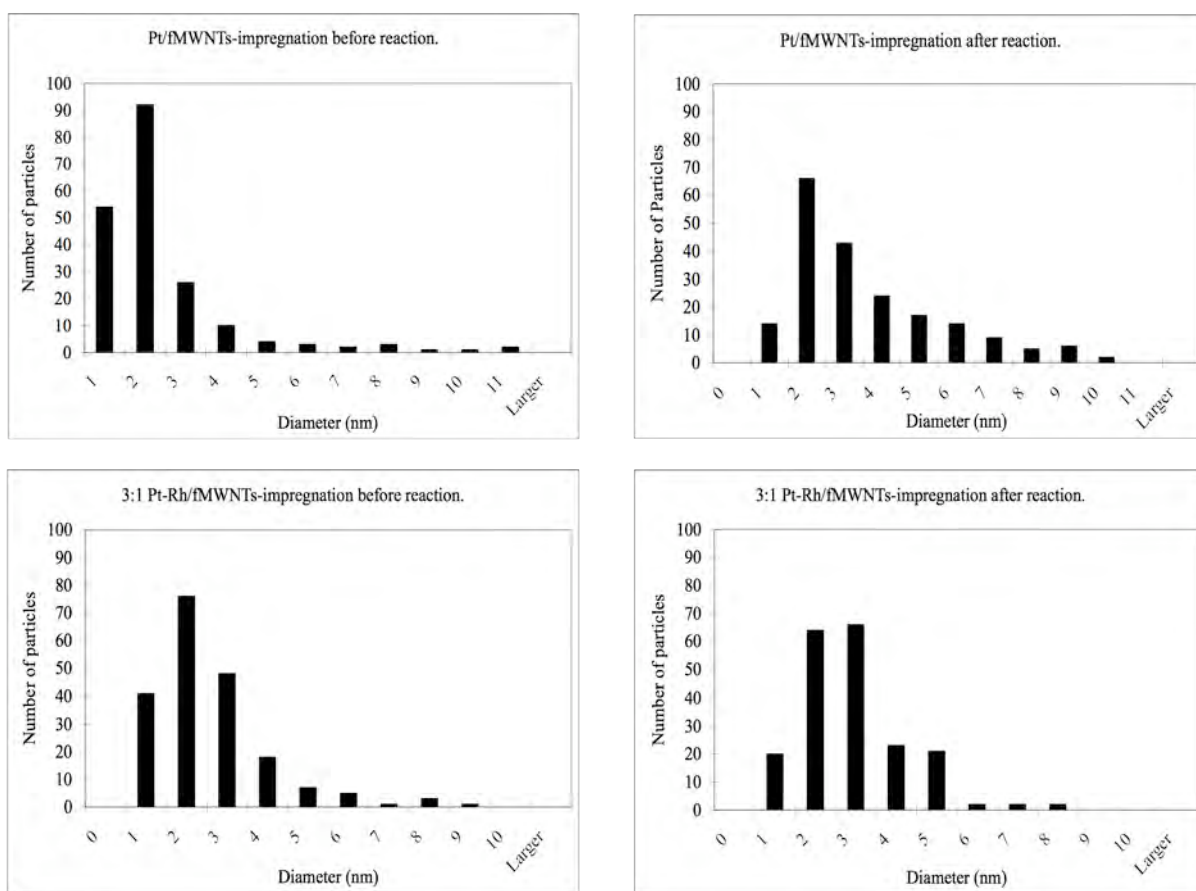


Figure 24. Particle size distribution histograms for fresh 2 wt.% Pt/fMWNTs-I (top left), 2 wt.% Pt/fMWNTs-I after exposure for ~12 h to reaction conditions (top right), fresh 1.5 wt.% Pt – 0.5 wt. % Rh/fMWNTs (bottom left) and 1.5 wt.% Pt – 0.5 wt. % Rh/fMWNTs after exposure for ~12 h to reaction conditions (bottom right) (200 particles measured *per* histogram). Reaction conditions: 500 ppm NO, 500 ppm C₃H₆, 10% O₂ and 10% H₂O, balance nitrogen; GHSV= ca. 50,000 h⁻¹; T= 150-300 °C.

A comparison between these histograms permits an assessment of the extent of metal particle growth resulting from exposure to the reaction conditions. Although the particle size distributions of the used catalysts did shift towards larger particles, these shifts corresponded to a particle growth of only 1-2 nm. Further, particle growth was found to be very similar for both the mono and the bimetallic catalyst.

With the aim of further optimizing the 1.5 wt.% Pt – 0.5 wt.% Rh/fMWNTs catalyst (the best formulation found so far), an alternative preparation method was attempted based on a recent patent [50] describing the preparation of Pt-Rh three-way catalysts. In this method, the support is first dispersed in water and the appropriate amount of ethanolamine platinum (IV) hexahydroxide is added to the resulting suspension. The pH is adjusted to 6.0 with dilute aqueous ammonia solution to precipitate the Pt. After this, the appropriate amount of $\text{Rh}(\text{NO}_3)_3$ is added and the pH is adjusted to 7.0 to precipitate the Rh. Finally, the suspension is centrifuged, the supernatant decanted, and the solid dried. Following this procedure, two catalyst batches were produced: one was tested for de NO_x activity as-prepared, while the other was exposed to a flow of H_2 at 400 °C for 3 h (a reduction step not included in the patent) prior to testing. Figure 25 shows the de NO_x performance of these two catalysts and compares it with that of a catalyst prepared *via* impregnation.

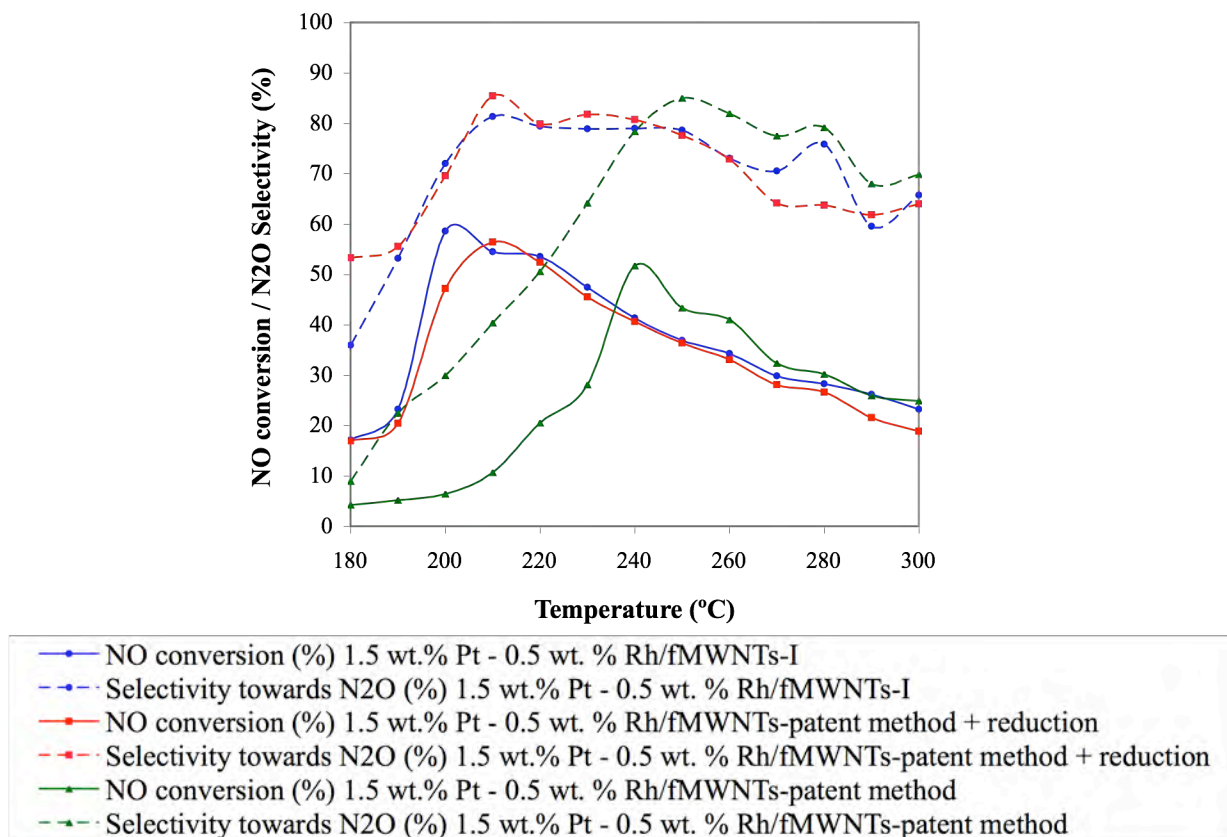


Figure 25. Combined plot showing the performance of three 1.5 wt.% Pt – 0.5 wt.% Rh/fMWNTs catalysts prepared by different methods. Feed composition: 500 ppm NO, 500 ppm C₃H₆, 10% O₂ and 10% H₂O, balance nitrogen. Gas flow: ca. 50,000 L gas · L cat⁻¹ · h⁻¹.

As can be seen from the figure, neither of these newly prepared catalysts surpassed the NO reduction performance of the catalyst previously prepared by impregnation. However, it is interesting to note that of the two catalysts prepared by the patent method, only the one that was reduced showed an activity similar to that of the catalyst prepared by impregnation. On the other hand, the unreduced catalyst's deNO_x activity went from almost zero across the whole temperature range to that shown in Figure 25 after a couple of hours under reaction conditions. This suggests that a slow *in situ* reduction of the Pt was taking place which in turn indicates that Pt is required to be in the metallic state to catalyze the HC-SCR reaction.

Sodium promotion:

The effects of Na⁺ addition on the performance of Pt/Al₂O₃ HC-SCR catalysts have recently been reported in the literature [51,52]. These effects, which include not only an increase in the deNO_x activity but also an improvement in catalyst selectivity towards N₂ when propene is used as the reductant, are thought to have their origin in the electrostatic field induced by the sodium cation, which strengthens the Pt-electron acceptor (NO and O₂) bonds while weakening the Pt-electron donor (C₃H₆) bonds, as well as weakening the N-O bond in adsorbed NO molecules [53].

Based on these observations, the promoting effect of Na^+ was studied for Pt/fMWNTs and Pt-Rh/fMWNTs catalysts. Three Pt-Na/fMWNTs catalysts with different Pt:Na weight ratios (2:1, 2:5 and 2:10) were prepared by a method involving two sequential impregnations followed by Na precursor decomposition under He and Pt reduction under H_2 [52]. These catalysts were then tested for de NO_x activity using propene as reductant. Of these, the 2:10 catalyst showed the highest activity, the performance of 2:1 and 2:5 catalysts being poor. This can be rationalized on the basis that while adsorption of both oxygen and NO is enhanced by Na^+ promotion, oxygen adsorption is favored since it is a stronger electron acceptor than NO. Therefore, for a given Pt loading and reductant concentration, the sodium loading has to be sufficiently high to enhance NO adsorption, while ensuring that oxygen adsorption is not taken to a regime at which the catalyst is poisoned [51]. As shown in Figure 26, the 2 wt.% Pt – 10 wt.% Na/fMWNTs catalyst shows a NO conversion of between 20 and 30% over the 130 to 300 °C temperature range.

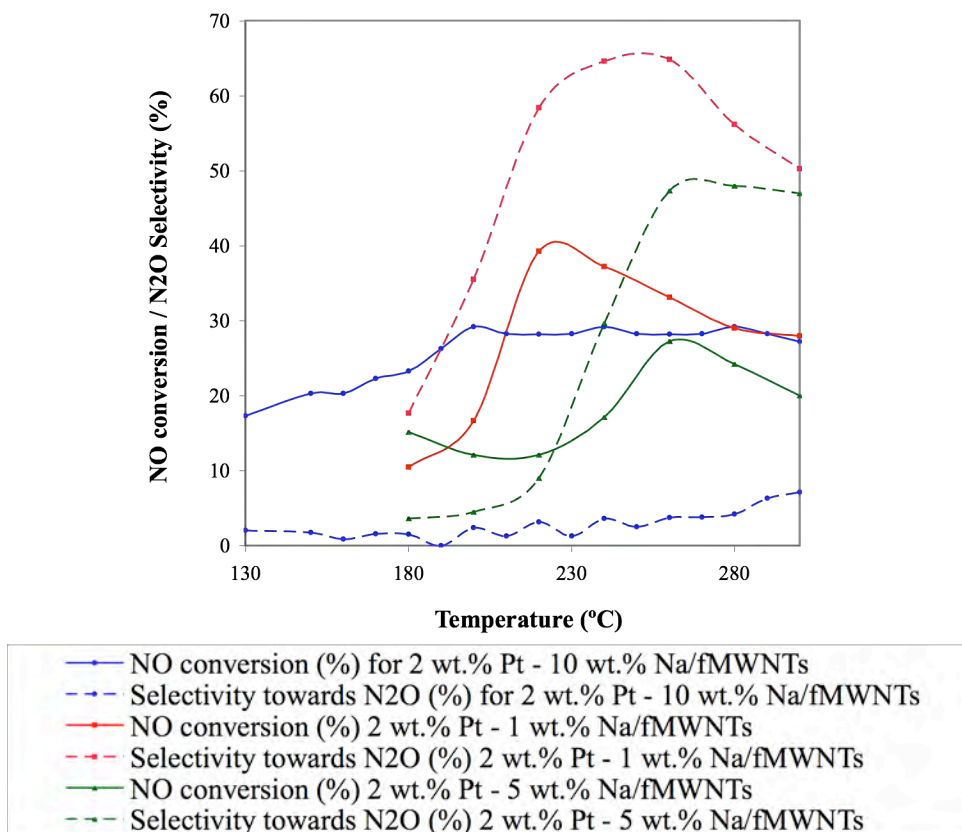


Figure 26. Plot showing the performance of 2 wt.% Pt – 10 wt.% Na/fMWNTs-I, 2 wt.% Pt – 1 wt.% Na/fMWNTs-I and 2 wt.% Pt – 5 wt.% Na/fMWNTs-I in NO reduction with propene. Feed composition: 500 ppm NO, 500 ppm C_3H_6 , 10% O_2 and 10% H_2O , balance nitrogen. Gas flow: ca. $50,000 \text{ L gas} \cdot \text{L cat}^{-1} \cdot \text{hr}^{-1}$.

Further, the NO reduction product seems to be almost exclusively N_2 . The de NO_x activity shown by this catalyst is comparable to that reported in the literature for Pt-Na/ Al_2O_3 catalysts with

similar Pt:Na ratios. However, the N₂-selectivity shown by the 2 wt.% Pt – 10 wt.% Na/fMWNTs catalyst is considerably superior to that shown by both unpromoted Pt/fMWNTs and Na⁺-promoted Pt/Al₂O₃ catalysts.

Two alternative ways of preparing a 2 wt.% Pt – 10 wt.% Na/fMWNTs catalyst were also attempted: 1) Pt and Na precursors were impregnated onto the support simultaneously before being reduced with H₂, and 2) the Pt precursor was impregnated and reduced before the Na precursor was impregnated and decomposed. Unfortunately, both catalysts showed disappointingly low NO reduction activity. TEM measurements were then performed in an attempt to understand the influence of the catalyst preparation method on the observed catalyst behavior. In general, two main features were observed in all of the samples: 1) large MWNTs aggregates that, when analyzed *via* EDS, were shown to contain Pt and a significant amount of sodium, and 2) regions in which small bundles of MWNTs (or even individual MWNTs) could be observed which resembled the appearance of the corresponding sodium-free catalysts, and which were indeed confirmed to be free of sodium by EDS. Representative micrographs of these two types of regions in the 2 wt.% Pt – 10 wt.% Na/fMWNTs-I catalyst are shown in Figure 27 and Figure 28, respectively.

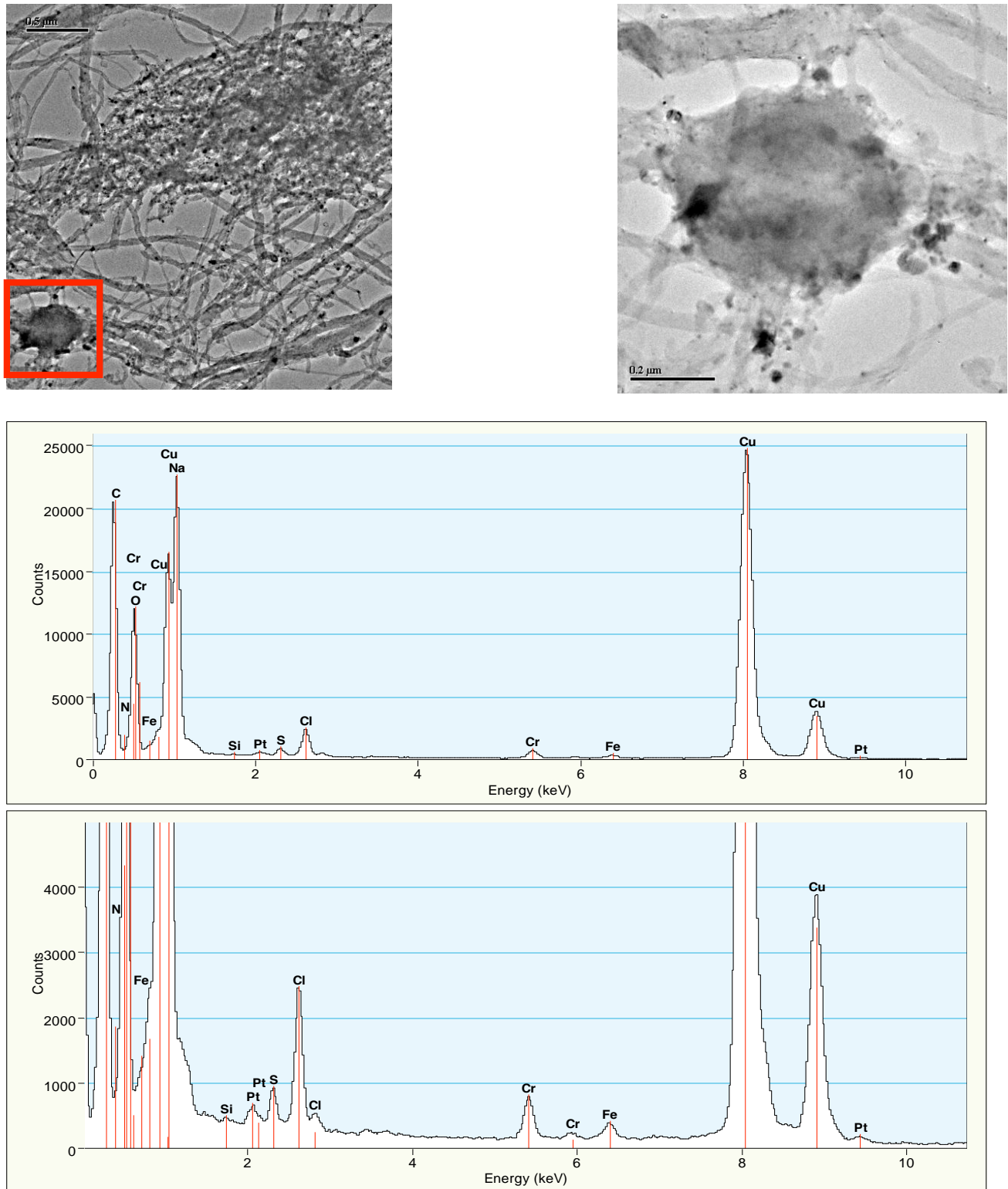


Figure 27. TEM micrograph of a region containing a MWNTs aggregate (left) within a 2 wt.% Pt – 10 wt.% Na/fMWNTs-I catalyst, a close-up of the highlighted area (right), EDS spectrum of the highlighted area (top) and a close-up of the low intensity peaks of the spectrum (bottom).

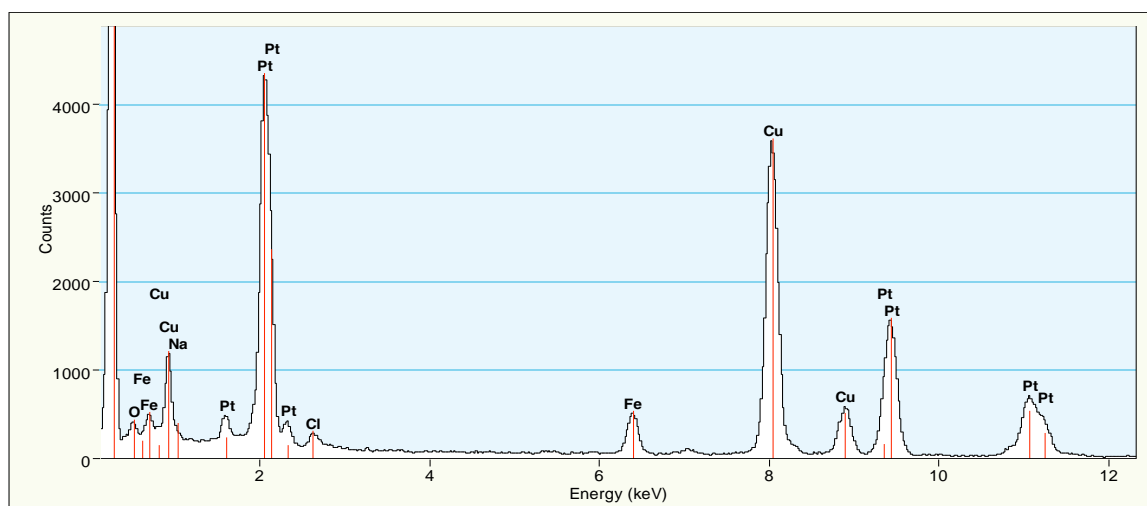
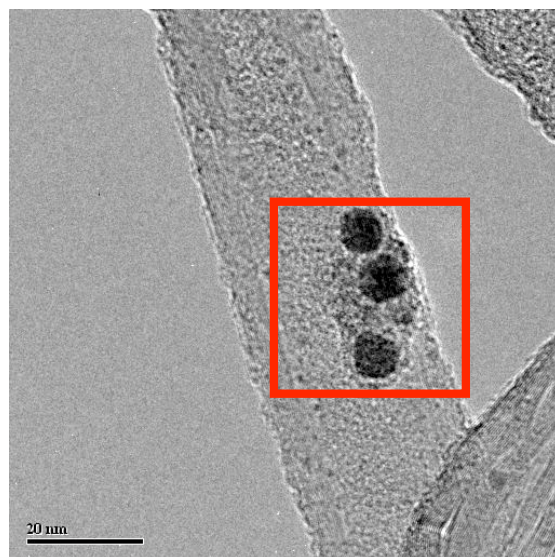


Figure 28. TEM micrograph of a region containing well dispersed MWNTs within a 2 wt.% Pt – 10 wt.% Na/fMWNTs-I catalyst and EDS spectrum of the highlighted area.

Since these two features were observed in all Pt-Na catalysts analyzed by TEM, the effect of the catalyst preparation method on catalyst performance cannot be explained on the basis of TEM data. There is also an apparent contradiction between the observations made with the TEM and the catalytic behavior of the 2 wt.% Pt – 10 wt.% Na/fMWNTs-I catalyst: if indeed this catalyst has sodium-free regions, a higher selectivity towards N_2O , closer to the one observed for sodium-free catalysts, would be expected. In fact, it can be argued that these sodium-free regions are actually a product of the TEM sample preparation method, in which the material is dispersed by sonication in a volatile organic solvent, i.e., agglomeration of the Na^+ phase may occur during this process. Consequently, an alternative sample preparation method was used in STEM experiments performed to understand the effect of the preparation method on catalyst performance (see Section 6, pages 57-59).

The method that yielded the best performing Pt-Na catalyst was also used to prepare a 1 wt.% Pt – 1 wt.% Rh – 10 wt.% Na/fMWNTs catalyst. However, when tested, it showed rather poor NO reduction activity. This result was not completely unexpected, since it has been reported in the literature that Rh catalysts are inhibited by the presence of sodium. This is because, contrary to the case of Pt, propene is not strongly adsorbed on Rh and an excessive promotion of oxygen adsorption due to the presence of sodium leads to the inhibition of propene adsorption and oxidation [54].

Examination of alternative metals and metal promoters:

In order to study whether metals other than Rh and Ir could improve deNO_x activity and/or selectivity, a number of catalysts in which Pt was alloyed with alternative metals were prepared and tested. The support and preparation method for these catalysts was the same in all cases; *viz.*, fMWNTs and impregnation, respectively. Pd, Co and Ag were alloyed with Pt in a 1:1 weight ratio, however, the performance of these catalysts in the 180-300 °C temperature range proved to be considerably inferior to that shown by the corresponding Pt-only catalyst.

Given that Ag/Al₂O₃ has been reported to be one of the most active catalysts for NO_x reduction by hydrocarbons [55], a Ag/fMWNTs catalyst was prepared *via* the impregnation method. Since it is believed that Ag⁰ is the catalytically active phase in this reaction and the use of fMWNTs as support should keep the metal in a more reduced state (as compared to oxidic supports), the preparation and screening of this catalyst was of particular interest. Unfortunately, this catalyst showed little or no activity in the 180-300 °C temperature range, independent of the reductant used (propene, decane and ethanol were tested).

It has also been reported in the literature [56,57] that the addition of Rh to Ag/Al₂O₃ catalysts greatly improves their performance in NO_x reduction. A 1.8 wt.% Ag – 0.2 wt.% Rh/fMWNTs catalyst was therefore prepared; however, the catalytic behavior of the material was also disappointing, regardless of the reductant used.

6. Spectroscopic studies.

STEM and XPS studies:

When analyzing the 1 wt.% Pt – 1 wt.% Ir/fMWNTs-I catalyst *via* TEM, several parts of the sample exhibited a “spotted” appearance. Given that these “spots” could actually be clusters of just a few metal atoms, more detailed STEM studies were subsequently performed. When these regions were analyzed by EDS, peaks corresponding to the deposited metals were observed. Figure 29 shows the TEM micrograph, the STEM micrograph (under contrast mode) and the EDS spectrum of one of these regions.

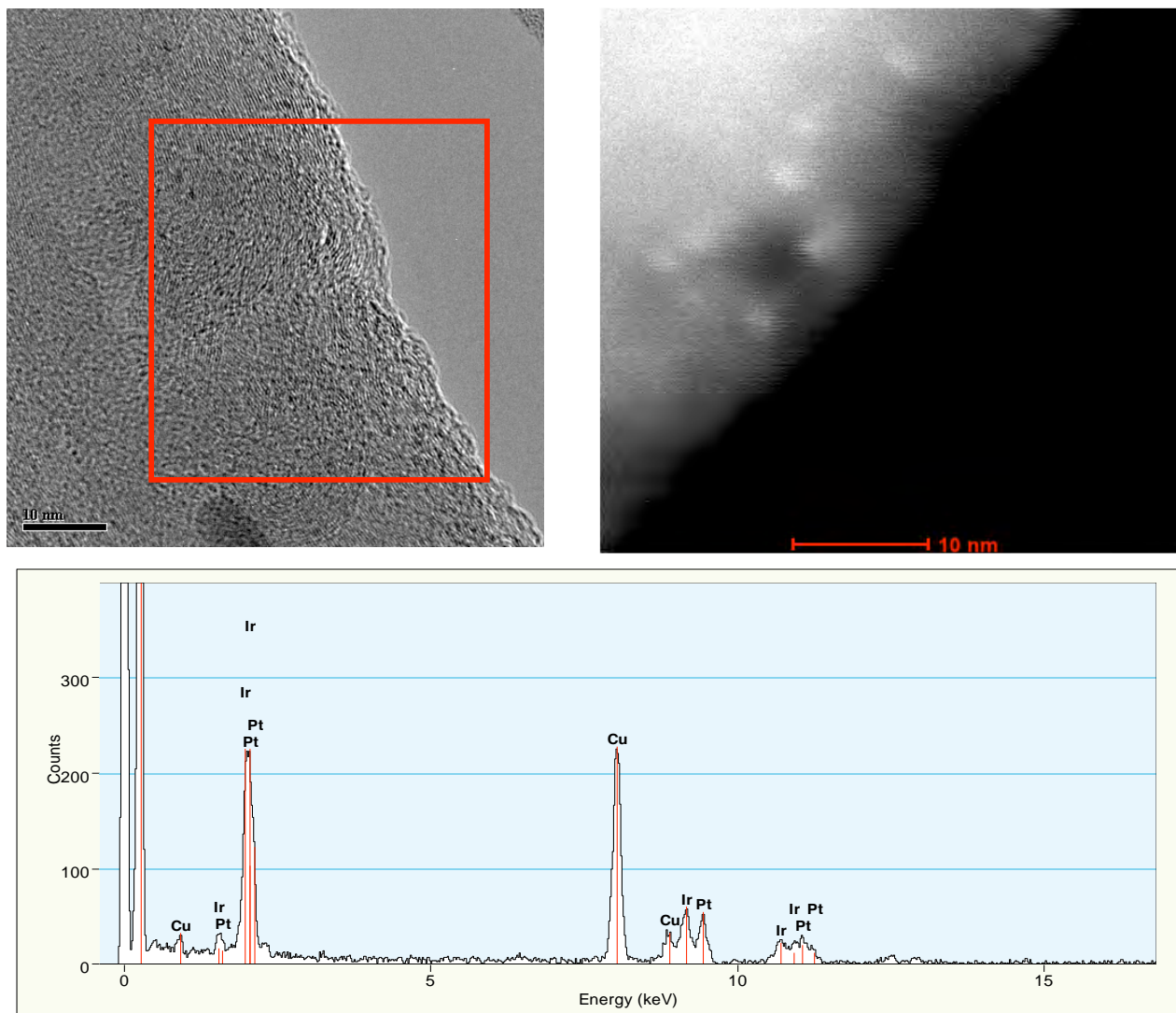


Figure 29. TEM micrograph of Pt-Ir/fMWNTs-I (upper left), STEM (under contrast mode) micrograph of approximately the same region of the sample (upper right) and EDS spectrum showing peaks corresponding to both Pt and Ir (bottom).

This seemed to confirm the presence of small metal clusters. However, whether these clusters are mono or bimetallic in the case of bimetallic catalysts had yet to be determined. In order to verify whether it is possible to establish the elemental composition of particles of approximately 1 nm in diameter by means of EDS, a 2 wt.% Pt/fMWNTs-I catalyst was first analyzed *via* STEM-EDS. Figure 30 shows 4 micrographs of approximately the same region of this catalyst taken at different magnifications.

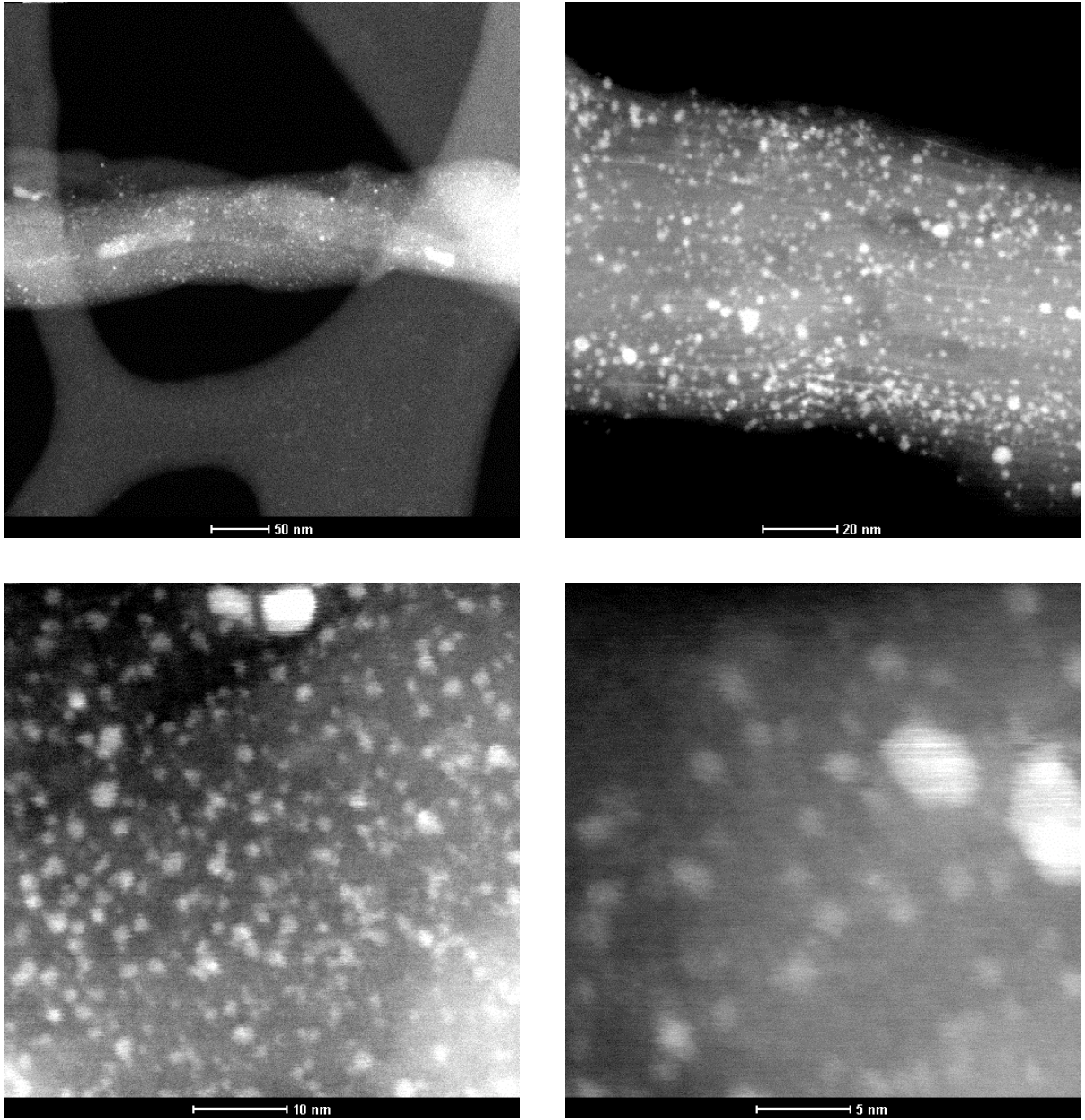


Figure 30. STEM micrographs under different magnifications of approximately the same region of 2 wt.% Pt/fMWNTs-I.

Figure 31 shows another STEM micrograph of the same sample, along with the energy-dispersive X-ray spectrum of the region indicated by the red square.

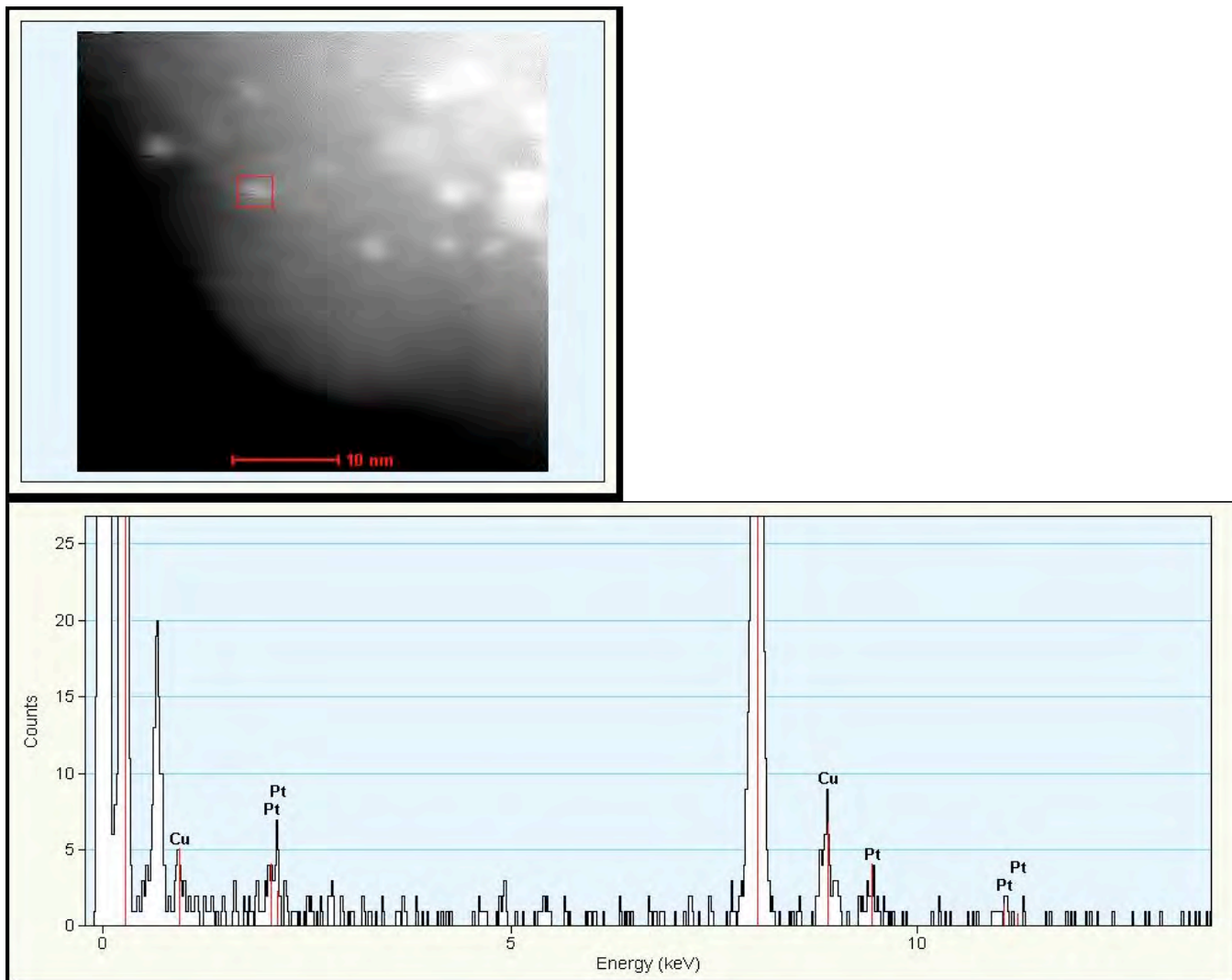


Figure 31. STEM micrograph of 2 wt.% Pt/fMWNTs-I and EDS spectrum of the region highlighted in the micrograph.

These figures confirm two things: 1) the median particle diameter of the 2 wt.% Pt/fMWNTs-I catalyst is between 2 and 3 nm, which is consistent with the particle size distribution histogram of the sample; and 2) it is indeed possible to use STEM-EDS in order to determine the elemental composition of small particles (<2 nm), at least in monometallic catalysts. Analyses were then focused on the 1 wt.% Pt – 1 wt.% Rh/fMWNTs-I bimetallic catalyst. Figure 32 shows a STEM micrograph of this catalyst and the EDS spectrum of the highlighted region.

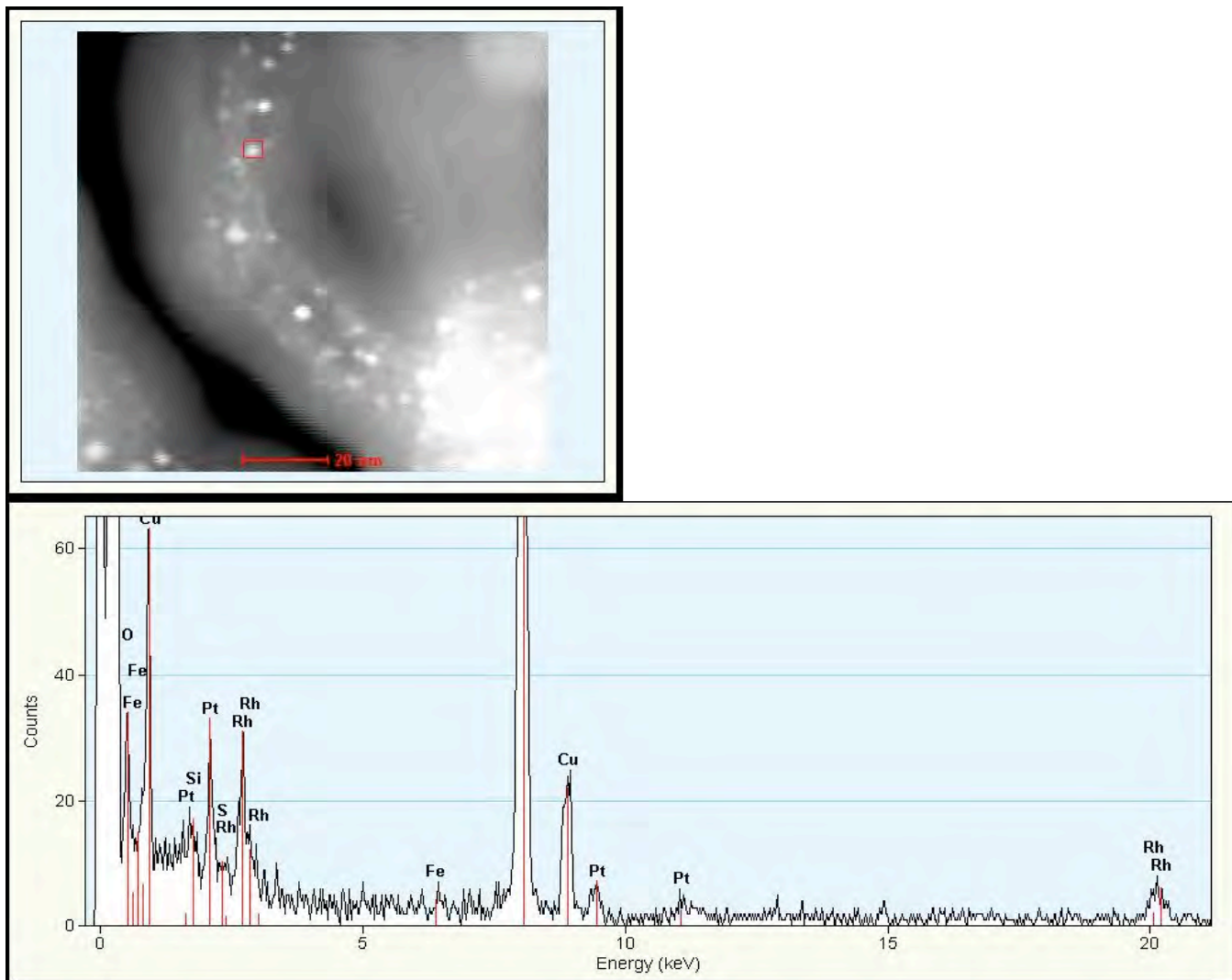


Figure 32. STEM micrograph of 1 wt.% Pt - 1 wt.% Rh/fMWNTs-I and EDS spectrum of the highlighted region.

The figure confirms that for the Pt-Rh bimetallic catalysts, particles as small as 1 nm are true Pt-Rh alloys, which is consistent with the shape of the deNO_x curves shown by these formulations. However, given that TEM is not a bulk technique and that only a small number of bimetallic particles were analyzed, these results are not conclusive with respect to whether the Pt:Rh ratio is fixed at the stoichiometric value in all particles, as opposed to varying from one particle to the next. It is also worth noting that for the bimetallic catalysts, STEM observations are in agreement with the particle size distribution histograms determined from TEM data.

In the scientific literature, two main variables have been invoked when trying to rationalize the catalytic performance of Pt HC-SCR catalysts: metal dispersion and support acidity. Burch [41] and Demicheli [40] have both concluded that high metal dispersion leads to less active catalysts in terms of turnover frequencies (TOFs). However, Denton and co-workers [42] have shown that lower dispersions do not translate into higher NO_x conversions due to the fact that decreasing

dispersion results in less (if more active) available sites. Thus, NO_x conversion seems to be independent of metal dispersion [23]. On the other hand, the acidity of the support has been found to be crucial to NO_x conversion. According to García-Cortés and co-workers [22], this is because hydrocarbon combustion, which is directly dependent on the acidity of the support, determines the level of activity and temperature window for the deNO_x reaction. Hence, acidic supports should be instrumental in the optimization of HC-SCR catalysts.

An additional factor which may influence the NO_x reduction activities of supported metal catalysts, but which to date has not been widely considered, is the oxidation state of the metal. Therefore, in this work four representative catalysts (2 wt.% Pt/ Al_2O_3 , 2 wt.% Pt/MWNTs, 2 wt.% Pt/fMWNTs and 1 wt.% Pt – 1 wt.% Rh/fMWNTs) were analyzed *via* XPS in order to investigate the electronic state of the metals present. It is well known that as Pt particles become smaller, they show an increasing tendency to exist as the oxide, PtO. Thus, two different binding energies were expected in the X-ray photoelectron spectrum of each catalyst: 1) for large particles (>1 nm), a binding energy corresponding to Pt in its metallic state (Pt^0); and 2) for small particles (<1 nm), a binding energy corresponding to PtO (Pt^{2+}) [58]. Unfortunately, the total metal loadings of the catalysts proved to be too low for XPS to quantify the amount of Pt present in each oxidation state. Consequently, catalysts with higher metal loadings were prepared and analyzed.

Given that the metal particle size can greatly influence the degree of PtO formation, the metal dispersions of catalysts between which a comparison is to be made should be as close as possible. Therefore, as a first step, a metal loading was chosen which would allow similar dispersions on MWNTs, fMWNTs and Al_2O_3 supports. Three Pt/ Al_2O_3 reference catalysts with different loadings (5 wt.%, 10 wt.% and 20 wt.%) were prepared (by impregnation) and their loadings were confirmed by XRF. Table 13 shows the metal dispersion and average Pt particle size of the catalysts, determined *via* H_2 -chemisorption, and compares them with the 2 wt.% Pt/ Al_2O_3 formulation.

Table 13. Metal dispersion and average particle size of model Pt/ Al_2O_3 reference catalysts.

Catalyst	Dispersion (%)	Average particle size (nm)
2 wt.% Pt/ Al_2O_3	100.0	1.0
5 wt.% Pt/ Al_2O_3	77.7	1.5
10 wt.% Pt/ Al_2O_3	57.4	2.1
20 wt.% Pt/ Al_2O_3	14.8	8.0

Taking these values into account, and the fact that for MWNTs-based catalysts the average particle size is consistently close to 2.0 nm, the 10 wt.% total metal loading was chosen and three representative catalysts (Pt/MWNTs, Pt/fMWNTs and 3:1 Pt-Rh/fMWNTs) were prepared *via* impregnation targeting this loading. The particle size distribution histograms of these three MWNTs-based catalysts, along with that of the Al_2O_3 -supported catalyst (all shown in Figure 33), were then obtained by means of TEM.

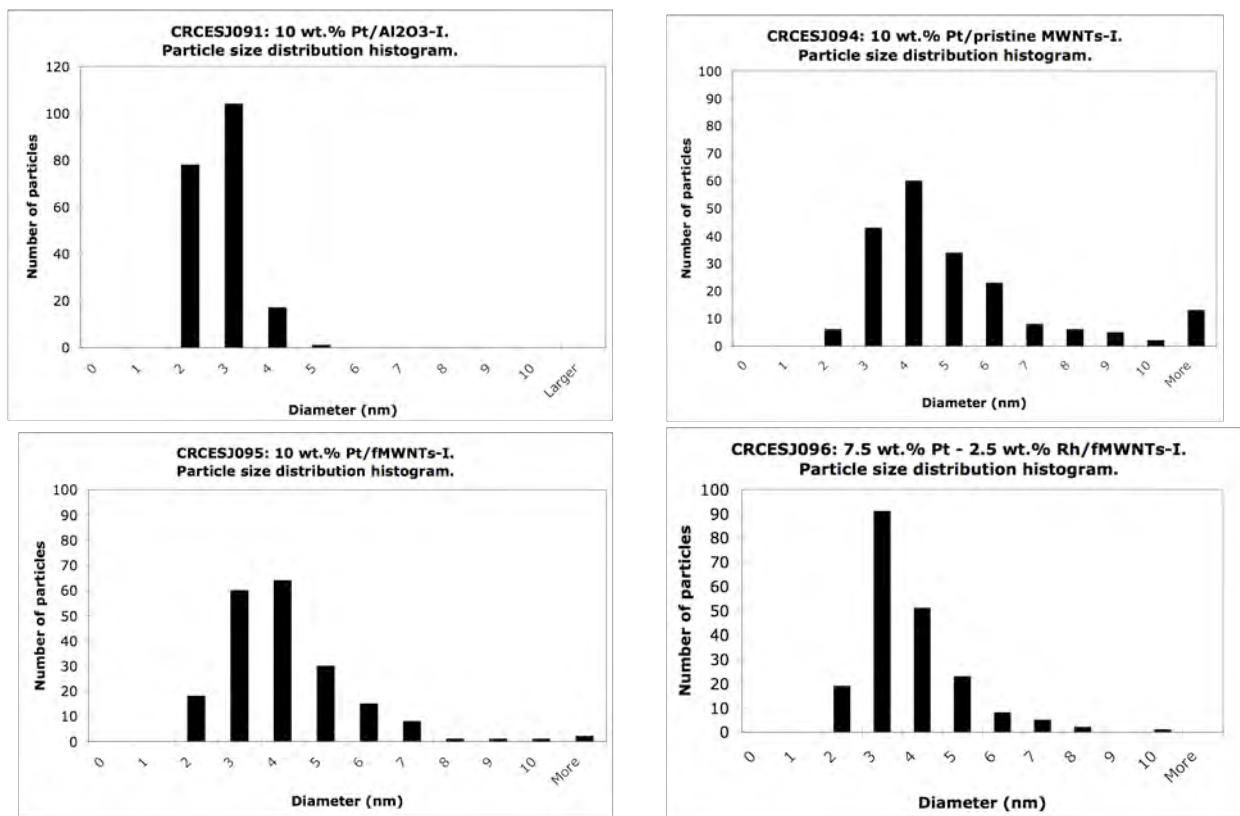


Figure 33. Particle size distribution histograms for 10 wt.% Pt/Al₂O₃ (top left), 10 wt.% Pt/MWNTs (top right), 10 wt.% Pt/fMWNTs (bottom left) and 7.5 wt.% Pt – 2.5 wt.% Rh/fMWNTs (bottom right) (200 particles measured per histogram).

As can be seen from Figure 33, all the particle size distribution histograms have their maxima in the 3-5 nm range. This validated the use of these catalysts for the XPS studies, which were subsequently carried out at an outside laboratory. Figure 34 shows an expanded view of the Pt 4d region in the XPS spectrum of the 10 wt.% Pt/Al₂O₃ reference catalyst.

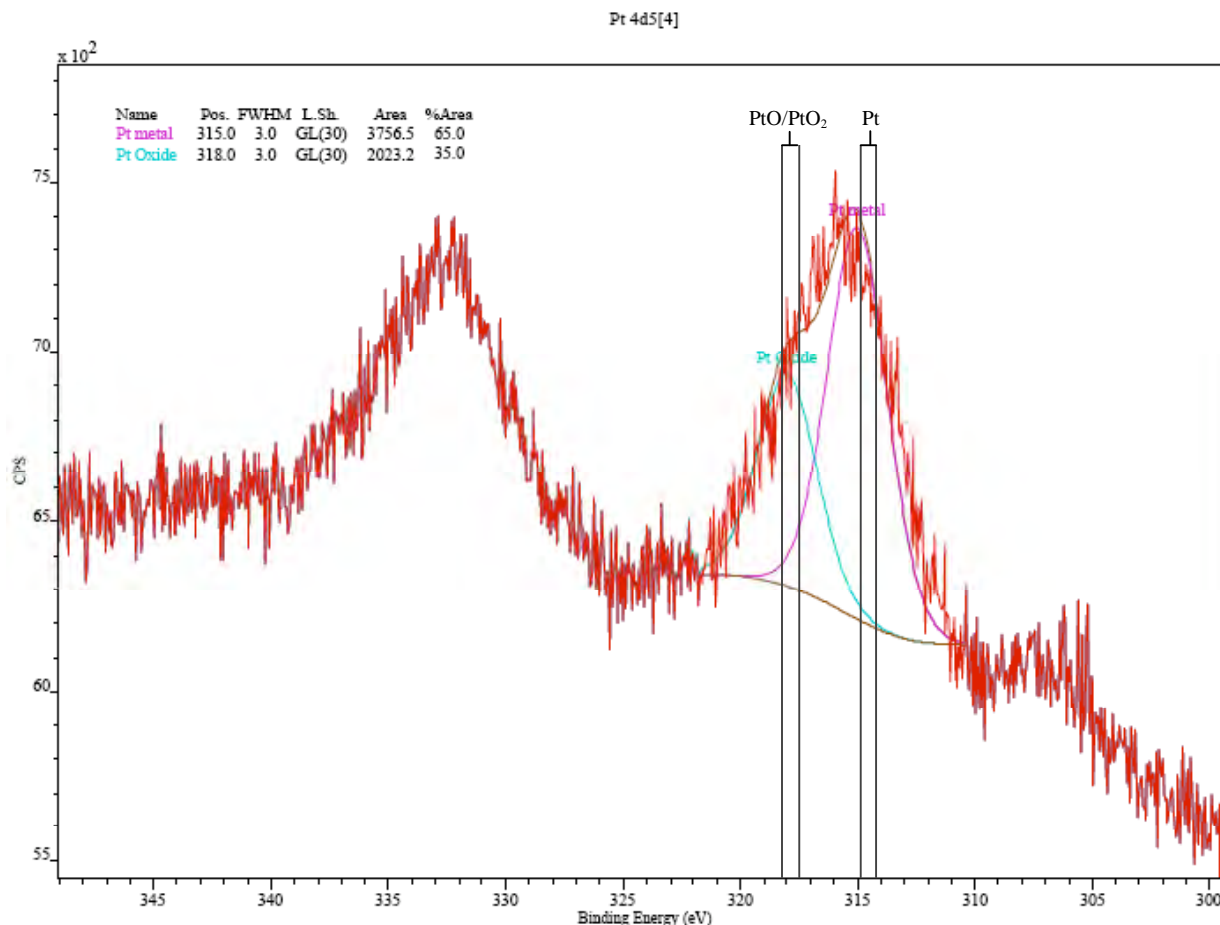


Figure 34. Expanded view of the Pt 4d region in the XPS spectrum of the 10 wt.% Pt/Al₂O₃ reference catalyst. The ranges shown in the spectrum correspond to those of the Pt 4d_{5/2} peak (right peak in the spectrum) as reported in the X-ray Photoelectron Spectroscopy Database of the National Institute of Standards and Technology (NIST) [59].

Given that analysis of the main Pt peak (4f) was rendered impractical due to interference from the Al 2p peak, peak fitting was performed on the Pt 4d_{5/2} peak. As shown in Figure 34, the resulting fit indicates that approximately two-thirds of the analyzed Pt is in the metallic form while the remaining third is present as the oxide. Given the low signal intensity of this peak, the fitting results should be viewed with caution. Nevertheless, they provide a clear indication that a considerable fraction of the Pt is present in the oxidized form when alumina is used as the support.

Figure 35 compares the Pt 4f peak of Pt/MWNTs, Pt/fMWNTs and 3:1 Pt-Rh/fMWNTs.

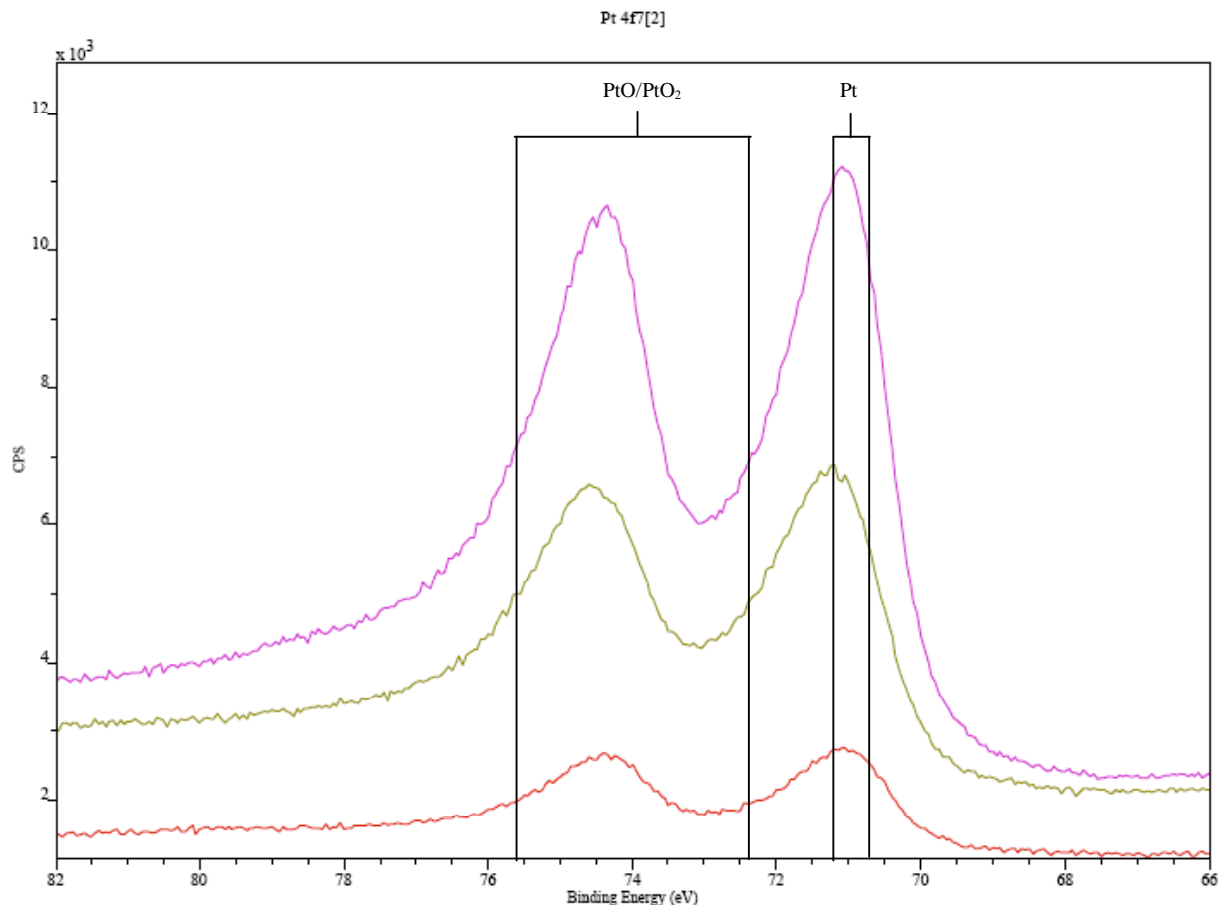


Figure 35. Combined plot showing an expanded view of the Pt 4f region in the XPS spectra of 10 wt.% Pt/MWNTs (top), 10 wt.% Pt/fMWNTs (middle) and 7.5 wt.% Pt – 2.5 wt.% Rh/fMWNTs (bottom) catalysts. The ranges shown in the spectrum correspond to those of the Pt 4f_{7/2} peak (right peak in the spectrum) as reported in the X-ray Photoelectron Spectroscopy Database of the National Institute of Standards and Technology (NIST) [59].

As can be seen from the figure, the intensity of the peaks, which represents the amount of Pt analyzed, follows the order Pt/fMWNTs > Pt-Rh/fMWNTs > Pt/MWNTs. This ordering is consistent with the metal dispersions in the catalysts as indicated by TEM. Further, the fact that in all cases the right peak is higher than the left peak indicates the presence of very little platinum oxide, if any at all (estimated at $\leq 5\%$ for each catalyst). This seems to be in agreement with the rationalization concerning the improved deNO_x activity shown by MWNTs-based catalysts compared to the activities shown by catalysts with oxidic supports; namely, that Pt is kept in a more reduced state in the former.

To further ensure that the oxidation state of the metal is indeed a support effect and not a particle size effect, the XPS analysis of an Al₂O₃-based catalyst with a considerably lower metal dispersion was performed. A 20 wt.% Pt/Al₂O₃ catalyst was prepared, having a metal dispersion of ~15% according to H₂-chemisorption. In contrast, the three original model catalysts were

determined to have dispersions of ~60% by the same method. Reassuringly, when the 20 wt.% Pt/Al₂O₃ catalyst was analyzed *via* XPS, its spectrum appeared to be very similar to that of the original Al₂O₃-based model catalyst, *i.e.*, *ca.* one-third of the Pt was present as the oxide. This corroborates the hypothesis that MWNTs stabilize the metal in a more reduced state, a desired effect given that metallic Pt is believed to be the active phase in the HC-SCR reaction.

Unfortunately, given that the amount of PtO is too low to be quantified in the MWNTs-based catalysts, the XPS results are inconclusive with respect to the effect on the Pt oxidation state that both Rh and the use of MWNTs versus fMWNTs may have.

Finally, it is important to mention that during the preparation of the alumina-based formulations, the metal precursor is decomposed to Pt metal by the calcination (under air) of the green catalysts at 400 °C for 2.5 hours. This is in contrast to the way in which Pt metal particles are produced when MWNTs are used as the catalyst support (reduction under 10% H₂ in He at 350 °C for 3.5 hours). In order to probe whether the preparation method had any influence in the oxidation state of the metal, a 10 wt.% Pt/Al₂O₃ model catalyst was prepared by a method involving sequential impregnations followed by H₂ reduction. After confirming its Pt loading by means of XRF and its Pt particle size by means of H₂ chemisorption, the model catalyst was analyzed by XPS. Figure 36 shows an expanded view of the Pt 4f and the Al 2p region in the XPS spectrum of the 10 wt.% Pt/Al₂O₃ catalyst prepared with H₂ reduction.

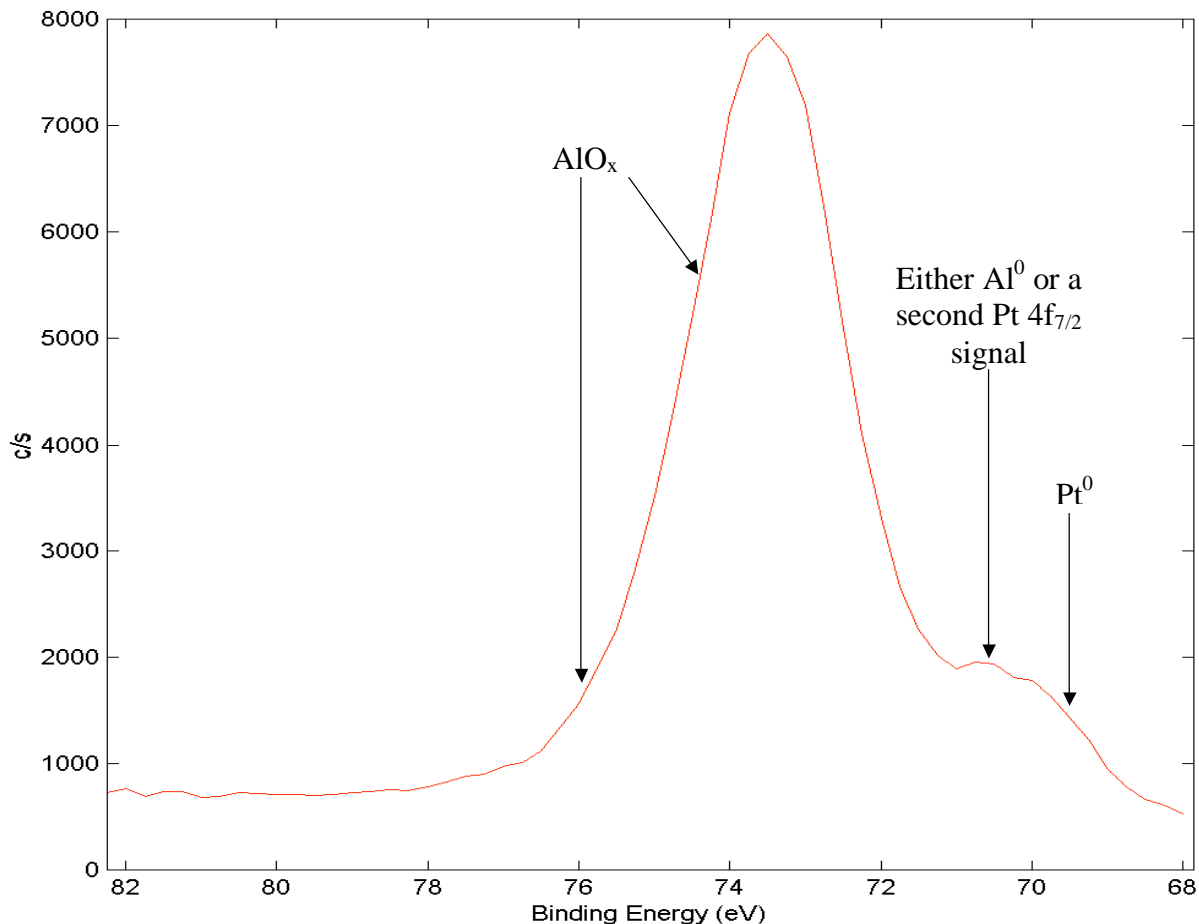


Figure 36. Expanded view of the Pt 4f and the Al 2p region in the XPS spectrum of 10 wt.% Pt/Al₂O₃ prepared by impregnation followed by H₂ reduction.

As shown in Figure 36, besides proving the presence of both metallic Pt and oxidized Al, the Pt 4f / Al 2p signal provides evidence for either another form of Pt or the presence of metallic Al. Given the unlikelihood of Al being present in the metallic form, XPS suggests that at least a fraction of the Pt is oxidized. Peak fitting of the Pt 4d_{5/2} signal (not shown) also suggests the presence of two different forms of Pt; however, the results proved less than conclusive due to the rather symmetric nature of the peak. Consequently, X-ray absorption near edge structure (XANES) experiments will be performed in the near future at Brookhaven National Laboratory with the aim of further probing the effect of the support on the Pt oxidation state.

In conclusion, the oxidation state of the metal can be invoked to explain the enhanced NO_x conversion observed when MWNTs-based materials are used as the support material as opposed to alumina. Further, it seems that the activity enhancement observed when functionalized (as opposed to pristine) MWNTs are used as the support can be explained by invoking the increased acidity of fMWNTs. However, additional experiments are required to probe this hypothesis.

Elemental mapping:

A set of elemental maps were acquired in order to gain further understanding of the most promising catalyst compositions identified to date; i. e., the 1.5 wt.% Pt – 0.5 wt.% Rh/fMWNTs and the 2 wt.% Pt – 10 wt.% Na/fMWNTs catalysts. To this end, the samples were first imaged with the electron microscope under the transmission mode to find representative regions. Once this was done, the microscope was switched to the scanning transmission mode under which the chosen region was simultaneously scanned and analyzed *via* EDS. After the scan was complete, the raw data were processed into intensity maps in which the brightness of a given pixel corresponds to a particular element's concentration in that region of the sample.

For the 1.5 wt.% Pt – 0.5 wt.% Rh/fMWNTs catalysts, the main focus was on determining the location of Pt and Rh with respect to each other. Figure 37 shows the carbon, platinum and rhodium maps of a 1.5 wt.% - 0.5 wt.% Rh/fMWNTs catalyst, along with the STEM micrograph in which the mapped region is highlighted, and a composite image of the three elemental maps.

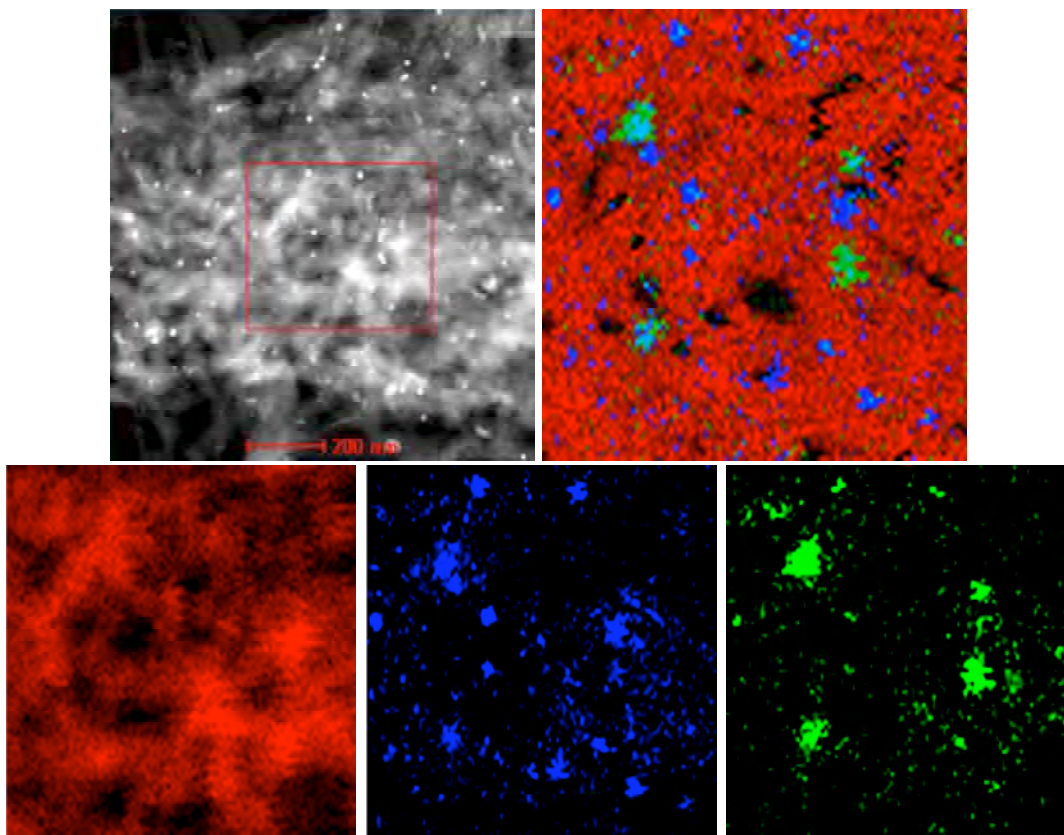


Figure 37. STEM micrograph (top row, left) of a 1.5 wt.% Pt – 0.5 wt.% Rh/fMWNTs catalyst; elemental maps (bottom row) for carbon (red), platinum (blue) and rhodium (green); and a composite image of all three elemental maps (top row, right). The maps were taken from the highlighted region in the STEM micrograph.

Both the shape of the activity curves and previously executed STEM-EDS analyses (*vide supra*) have suggested Pt and Rh to be truly alloyed (even in particles as small as 2 nm) and, as can be seen in the figure, this fact was confirmed in the bulk material by an elemental map taken of a region of $\sim 1 \mu\text{m}^2$. In order to appropriately interpret these elemental maps, it is important to remember that a transmission electron microscope compresses a three-dimensional space into a two-dimensional image. Therefore, superimposed small precious metal particles should not be mistaken to be a single large particle. As can be seen in Figure 37, there are both Pt-rich and Rh-rich regions in the bulk material; i.e., the distribution of these two metals throughout the support is not homogeneous. This is unsurprising, given the preparation method of this bimetallic catalyst. Indeed, the latter makes it reasonable to expect the resulting metal particles to cover the entire spectrum of Pt:Rh ratios.

For the 2 wt.% Pt – 10 wt.% Na/fMWNTs catalyst, emphasis was placed on determining the location of Pt and Na with respect to one other in an effort to rationalize the crucial effect that the preparation method has on catalyst performance. Figure 38 summarizes the three different preparation methods used to synthesize the 2 wt.% Pt – 10 wt.% Na/fMWNTs catalyst, along with a STEM micrograph in which the mapped region is highlighted, and the corresponding carbon, platinum, and sodium elemental maps.

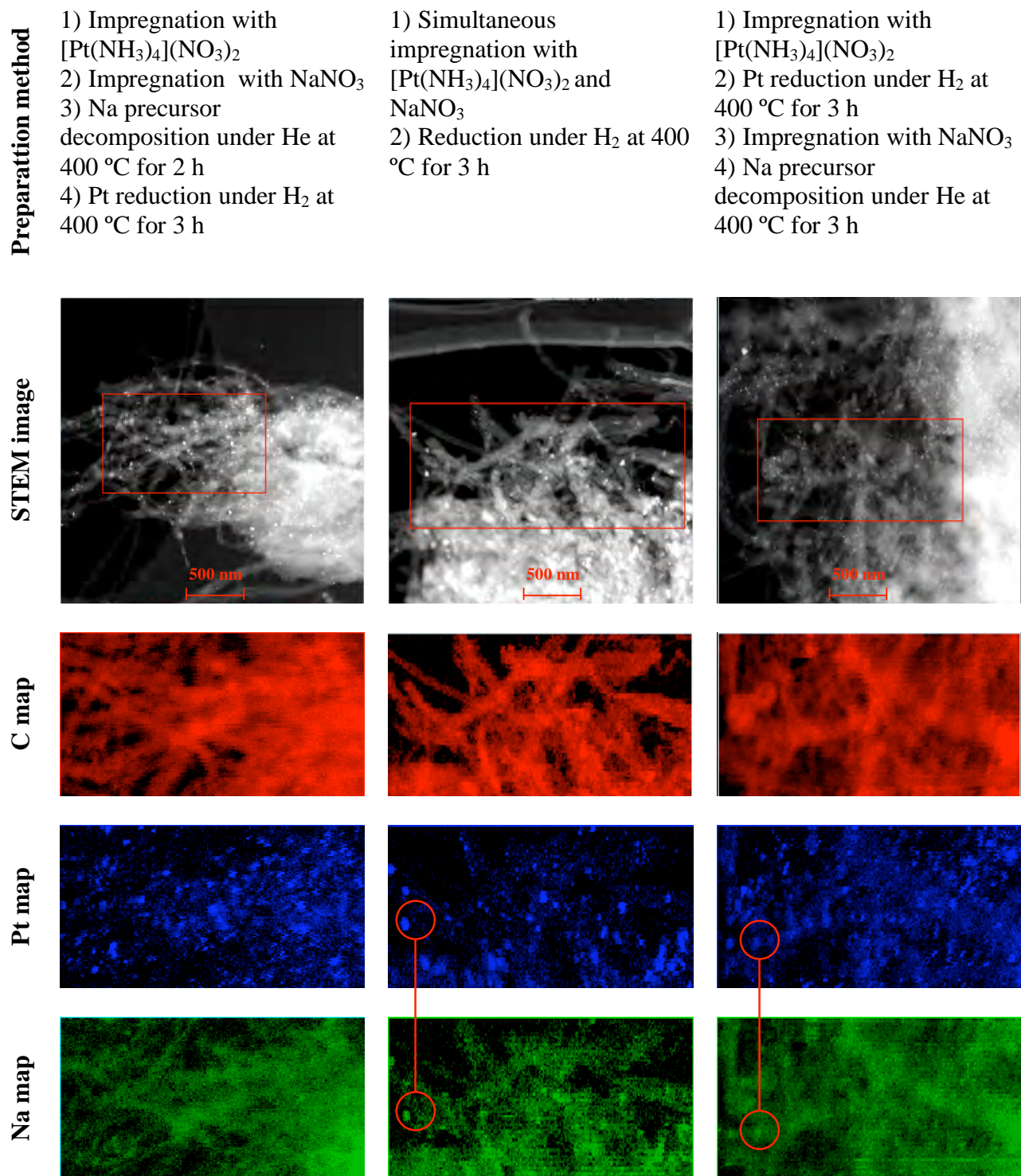


Figure 38. Carbon, platinum and sodium maps of three 2 wt.% Pt – 10 wt.% Na/fMWNTs catalysts prepared by different preparation methods (the mapped region corresponds to the highlighted rectangles in the STEM micrographs).

In past TEM-EDS experiments, parts of the sample containing well-dispersed MWNTs appeared to be Na-free. Given that this may have resulted from the use of a sample preparation method involving the dispersion of the sample in an organic solvent, this time a dry-mounting technique was used to load the sample onto the TEM grid (a less invasive method). Further, to ensure that the mapped regions were representative, regions were analyzed that contained both well-dispersed MWNTs and bulk-like material (as highlighted by the red rectangles on the STEM micrographs in Figure 38).

Taking into account that the catalyst represented by the left column was the only one showing promising performance, the maps were analyzed in an effort to rationalize the observed differences in catalyst properties. Comparing the Pt map in the left column with that in the middle column, the former seems to have a better Pt dispersion than the latter. Indeed, given that Na^+ was present in large excess, simultaneous impregnation should lead to most of the ion exchange sites on the fMWNTs support being occupied by Na^+ , which would be expected to result in a poor Pt dispersion. Thus, impregnating Pt before Na leads to a superior Pt dispersion, which might explain the improved deNO_x activity of the resulting catalyst.

Another feature of note is that the Na map in the right column shows areas of high Na concentration that seem to match the location of Pt in the corresponding Pt map. This may explain the improved performance of the catalyst represented by the left column with respect to that represented by the right one, given that one could argue that carrying out sodium precursor impregnation/decomposition after Pt impregnation/reduction would cause Pt to be covered by a layer of Na^+ , which might deactivate the Pt. Interestingly, this Pt-Na match is also observed in the catalyst represented by the middle column, while it appears to be absent from the one represented by the left column. With regards to the manner in which such deactivation might occur, two explanations are offered: 1) a Na coating would prevent the HC-SCR reactants from reaching the Pt surface; and 2) due to the close location of the metals with respect to one other, the effect of Na^+ in the inactive catalysts may be considerably higher than that in the active catalyst. Indeed, several authors have established that the Na-loading window in which promotional effects are observed is fairly narrow, since the sodium loading has to be sufficiently high to enhance NO adsorption, while ensuring that oxygen adsorption is not taken to a regime at which the catalyst is poisoned [51,52]. The latter may be occurring in the catalysts that show poor deNO_x activity.

Diffuse Reflectance Infrared Fourier Transform Spectroscopy (DRIFTS) studies:

DRIFTS studies were performed with the aim of identifying HC-SCR reaction surface intermediates, as well as establishing their location (i.e., whether they were adsorbed on the metal or on the support). Taking into account the fact that MWNTs are strongly IR-absorbing materials, prior to analysis a series of catalyst dilutions in KBr were prepared. Given that surface species resulting from the adsorption of NO_2 on Pt are known to possess relatively intense IR bands (compared to typical HC-SCR reaction surface intermediates), the dilute catalysts (contained in a cell equipped with KBr windows) were first exposed to a flow of 500 ppm NO_2 in N_2 . However, although some peaks were observed, it was determined that they corresponded to KBr-adsorbed NO_2 species. Therefore, a decision was made to use silicon in place of KBr, both for the cell window and as the diluent. Unfortunately, even when these changes were made and several experimental parameters essayed, the signal-to-noise ratio remained unacceptably

low. On this basis we conclude that there is no realistic prospect of obtaining meaningful DRIFTS spectra on these MWNTs-based catalysts.

7. Reactor studies.

Kinetic studies:

Experiments were performed in order to determine relevant kinetic parameters (activation energies and reaction orders) for NO reduction with propene catalyzed by the two MWNTs-based formulations with the highest deNO_x activity found to date: 2 wt.% Pt/fMWNTs and 1.5 wt.% Pt – 0.5 wt.% Rh/fMWNTs. The activation energies were calculated from a series of twelve Arrhenius plots obtained by permutation of the following reactant concentrations: [NO]= 250, 500, 800 and 1200 ppm; [C₃H₆]= 500, 1000 and 1500 ppm. The data points used to calculate the slope corresponded to temperatures below that at which the maximum NO conversion was observed. The reaction orders for NO were calculated from the slope of log-log plots of NO reduction rates vs. initial NO concentrations, using the following reactant concentrations: [NO]= 100, 250, 500, 800 and 1200 ppm; [C₃H₆]= 1000 ppm. Finally, the reaction orders for propene were calculated from the slope of log-log plots of NO reduction rates vs. initial C₃H₆ concentrations, using the following reactant concentrations: [C₃H₆]= 250, 500, 1000, 1500 and 2000 ppm; [NO]= 500 ppm. The results of this study are condensed in Table 14.

Table 14. Kinetic data for 2 wt.% Pt/fMWNTs and 1.5 wt.% Pt – 0.5 wt.% Rh/fMWNTs.

Catalyst	Activation energy (kJ/mol)	Reaction order for NO	Reaction order for NO	Reaction order for C ₃ H ₆	Reaction order for C ₃ H ₆
		190 °C	200 °C	190 °C	200 °C
2 wt.% Pt/fMWNTs	57±4	0.21	0.21	-0.31	0.64
1.5 wt.% Pt - 0.5 wt.% Rh/fMWNTs	58±8	0.13	0.28	-0.32	-0.46*

*0.39 at 205 °C.

Several conclusions can be drawn from these data. First, the activation energy values are lower than those reported in the literature for Pt/Al₂O₃ (91 kJ/mol) [18] and Pt-CeO₂/Al₂O₃ (173-182 kJ/mol) [60]. Bearing in mind the improved performance of MWNTs-based catalysts compared to that of formulations involving oxidic supports, this result is not unexpected. Also unsurprising were the more scattered activation energy values measured for the bimetallic catalyst compared to those of the monometallic formulation, given that in the former, the metal particles may cover the whole spectrum of Pt:Rh ratios, effectively behaving as a collection of catalysts and increasing the complexity of the system.

The observed reaction kinetics reflect, among other factors, the effect of temperature on the adsorption of reactants on the active sites of the catalyst and the reaction orders for propene

shown in Table 14 offer a good example of this. Negative reaction orders for C_3H_6 at 190 °C signify that at low temperatures the surface of the catalyst is covered, and therefore poisoned, by propene. As the temperature increases and approaches the light-off temperature of the reductant, the reaction orders for propene become positive, indicating the availability of active sites made possible by the oxidation of the alkene. These findings are also consistent with the results reported in Figure 20, which show a shift in the peak NO_x conversion to higher temperature upon increasing the propene concentration.

8. Preparation of monolithic catalysts.

Growth of MWNTs on a metal monolith:

In order to verify the feasibility of supporting MWNTs on automotive monoliths, the growth of MWNTs was attempted on a commercial 3" x 4" metallic monolith (300 cpsi, obtained from DCL Int. Inc.). In a typical experiment, the monolith was placed inside a nanotube synthesis reactor, consisting of a quartz tube reactor surrounded by a tube furnace. After purging the system with inert gas, a solution of ferrocene in xylenes was continuously introduced at a rate of 13 mL/hr via a syringe pump into a pre-heat section maintained at 200 °C. The xylenes/ferrocene vapors produced in this preheater were carried into the main part of the reactor, maintained 800 °C, by a flow of 10% H_2/N_2 . The walls of the monolith provide a surface on which MWNTs grow perpendicularly in parallel alignment. At the end of the run, the system was allowed to cool to room temperature and the monolith recovered. Visual inspection revealed the presence of a continuous and apparently uniform coating of MWNTs on the monolith. SEM measurements were subsequently performed in order to characterize the morphology of the supported MWNTs. Figure 39 shows a photograph of the coated monolith and a SEM image of the MWNT coating which reveals the high degree of nanotube alignment.

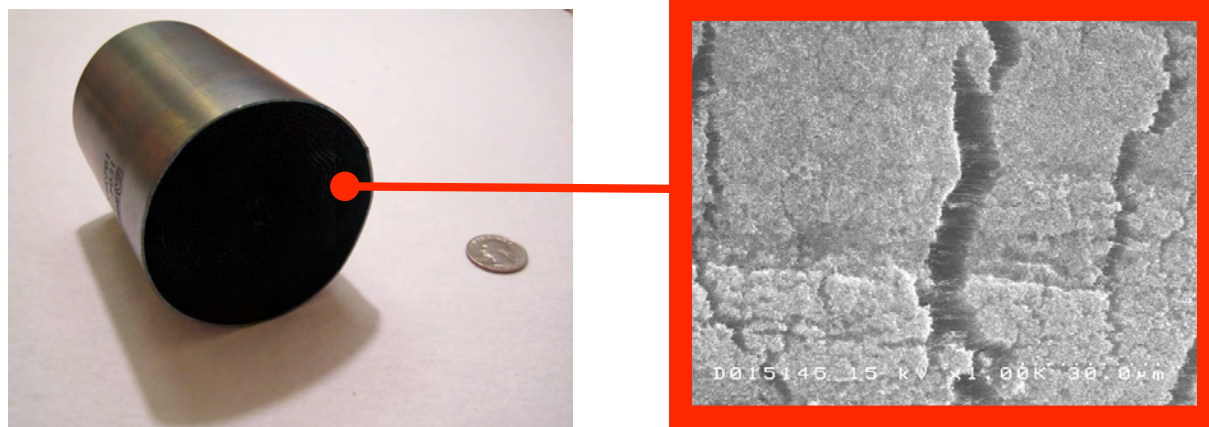


Figure 39. Photograph of a metal monolith coated with MWNTs and SEM image of the MWNTs showing their alignment.

Precious metal deposition on monolith-grown MWNTs:

The most promising low temperature HC-SCR formulations prepared in this project utilized functionalized multi-walled carbon nanotubes (fMWNTs) as the catalyst support and impregnation as the preparation method. However, it proved possible to prepare catalysts of fairly comparable performance using a polyol method for precious metal deposition and/or by using pristine MWNTs as the support (at low Pt loadings). This is particularly fortunate when trying to deposit precious metals on metal monolith-grown MWNTs, given that any attempt to functionalize the supported nanotubes with mineral acids would corrode the monolith, thus compromising its physical integrity. Therefore, the effectiveness of the polyol method to deposit Pt particles on untreated monolith-grown MWNTs was investigated, since this approach would both avoid MWNTs functionalization and promise to yield a catalytic device of satisfactory performance.

A recently published modified polyol method [61] was first followed. This method involves dissolving chloroplatinic acid (CPA) in ethylene glycol (EG) and heating the resulting solution in order to reduce the metal and produce a colloid, which is then put in contact with the support (monolith-grown MWNTs in this case). However, when this method was attempted, a problem immediately arose: the colloidal particles tended to aggregate and precipitate from the suspension. Given that this would negatively affect the Pt particle size of the product, it was decided to place the CPA in EG solution in contact with the support before carrying out the reduction. By so doing, colloidal Pt particles could be anchored by the support as soon as they formed, avoiding their aggregation and improving the metal dispersion in the final product. Unfortunately, the problem described above persisted, indicating that although Pt particles were forming, they were not being deposited on the support. Indeed, when the metal loading of the products of these two preparations was determined by means of proton induced X-ray emission (PIXE), the Pt content was considerably below that targeted. In an attempt to confirm the conclusions gathered from the PIXE analyses, some of the scraped material was observed under the transmission electron microscope. As can be seen in Figure 40, some relatively large particles (~ 20 nm in diameter) were observed and confirmed to be Pt by means of TEM-EDS.

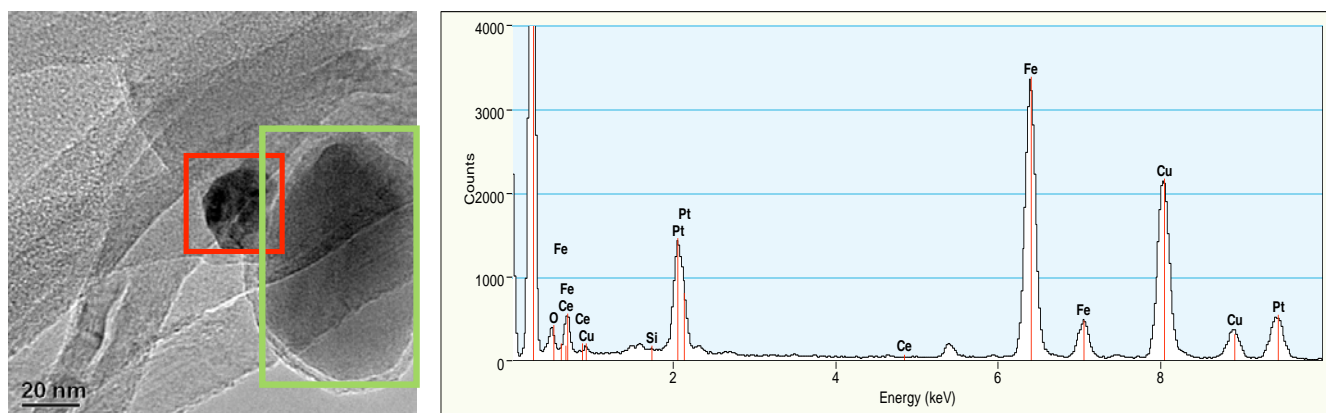


Figure 40. TEM image of a Pt/MWNTs/metal monolith catalyst and EDS spectrum of the area highlighted in red. An iron particle (the catalyst used in the production of the MWNTs) is highlighted in green.

Particles as small as 2 nm in diameter were also observed (see Figure 41), but their size impeded their elemental analysis by means of TEM-EDS. In general, however, relatively few Pt particles were found, consistent with the elemental analysis results.

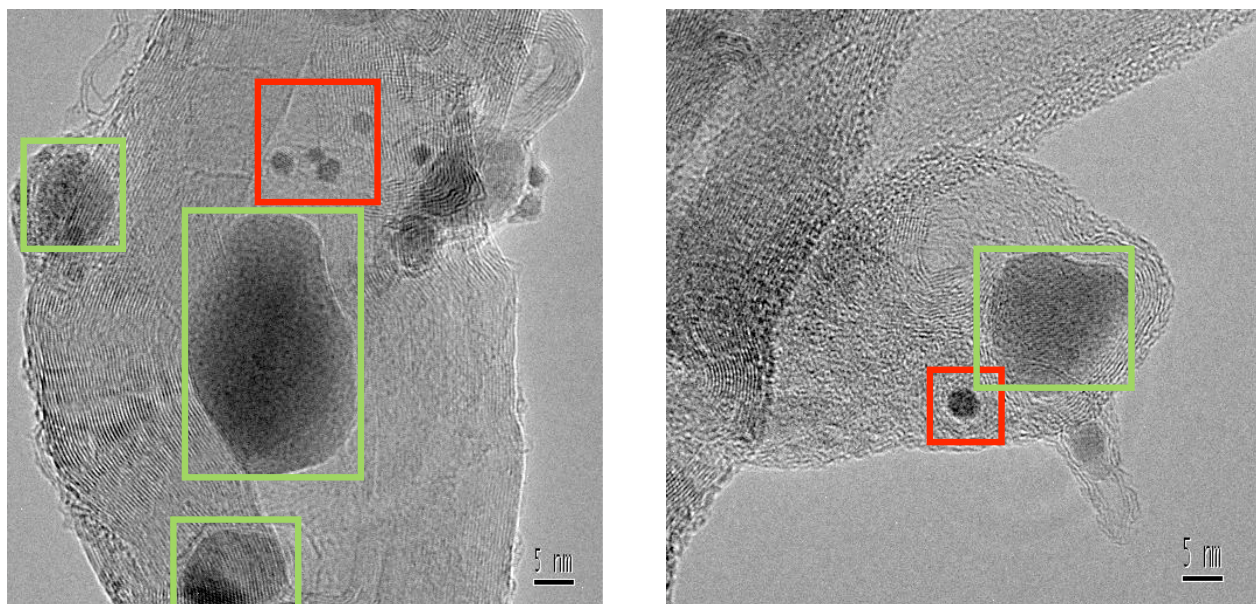


Figure 41. TEM image of a Pt/MWNTs/metal monolith catalyst showing both Pt metal particles of 2-5 nm in diameter (red) and iron catalyst particles remaining from the MWNT synthesis (green).

Evidently, acid activation of the MWNTs is a prerequisite for the deposition of high concentrations of Pt particles on nanotubes *via* the polyol method, as has been reported by some researchers [38]. Acid activation introduces functionalities which can anchor Pt ions prior to their reduction, thus facilitating metal deposition and improving the dispersion at high Pt loadings.

Activation of monolith-grown MWNTs:

It has been determined that the use of functionalized MWNTs as catalyst support yields formulations with improved HC-SCR performance. Further, it has also been established that prior to depositing precious metals on the surface of the monolith-tethered MWNTs, it is necessary to activate the latter. With this in mind and without forgetting that the use of mineral acids would be detrimental to the metal monolith, the surface modification of the monolith-grown MWNTs was attempted using alternative methods. A first attempt was made to activate MWNTs with the use of an oxygen plasma. Unfortunately, this process was found to be generally ineffective.

A second attempt was made following a recent report in the literature concerning the use of polyethyleneimine (PEI) as a functionalizing agent for MWNTs [62], in which a three-step approach was used to prepare a Pt/fMWNTs/metal monolith catalyst. The first step involved the adsorption of PEI on the surface of the MWNTs as a means to functionalize them. In the second

step, the PEI-fMWNTs/metal monolith was contacted with an aqueous CPA solution, aiming for the anchoring of the Pt to the functionalities introduced in the first step. In the third and last step, H₂ was flowed through the device at 350 °C, trying to accomplish both the reduction of the metal and the elimination of the PEI. Unfortunately, during the preparation the formation of a black precipitate could be observed, again suggesting that although Pt particles were formed, the particles failed to deposit on the surface of the MWNTs. Several variations of this method were examined in an attempt to achieve deposition of the Pt particles; however, the problem persisted.

Scouting experiments examining the adsorption of a variety of alternative surfactants including glycolic acid, octadecyl trimethyl ammonium bromide, sodium dodecyl sulfate and sodium dodecyl benzene sulfonate were also performed in an attempt to functionalize the MWNTs without the use of mineral acids. Unfortunately, these experiments also proved unsuccessful.

In view of this, the use of NO₂ was investigated as a means to functionalize the monolith-grown MWNTs prior to Pt deposition by the polyol method. First, TGA experiments were performed using pristine MWNTs in order to determine the feasibility of this nanotube activation method. These experiments were found to be fairly promising, given that after exposing a pristine MWNTs sample to a flow of 0.5% NO₂ in N₂ at 300 °C, the material showed a weight gain of *ca.* 1%, consistent with nanotube functionalization. Encouraged by these results, a MWNTs-coated metal monolith was then submitted to the same conditions to obtain metal monolith-grown NO₂-functionalized multiwalled carbon nanotubes (NO₂-fMWNTs) onto which the deposition of Pt by the polyol method was subsequently attempted. Reassuringly, during the course of the metal deposition no colloidal particles could be seen precipitating from the suspension, suggesting the successful deposition of Pt onto the monolith-grown NO₂-fMWNTs. In order to confirm that the metal deposition had indeed taken place, a small amount of carbonaceous material was scraped from the monolith and observed under the TEM. Figure 42 and Figure 43 show TEM micrographs for a Pt/NO₂-fMWNTs/metal monolith and a 3:1 Pt-Rh/NO₂-fMWNTs/metal monolith catalyst, respectively.

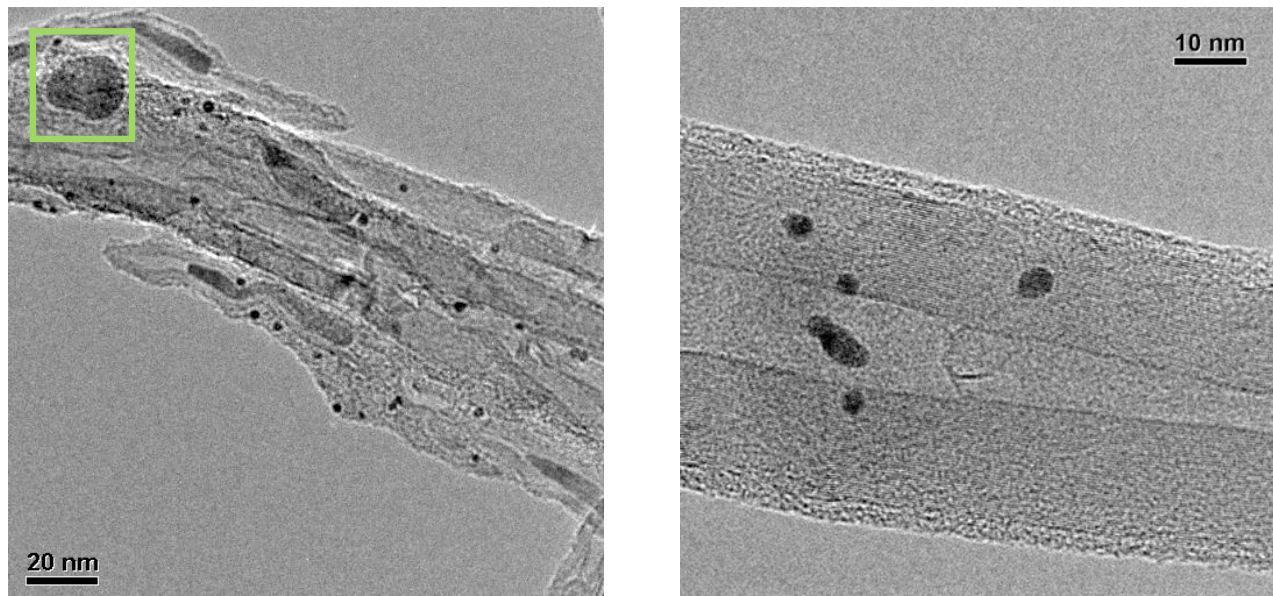


Figure 42. TEM micrographs of Pt/NO₂-fMWNTs/metal monolith (an iron catalyst particle remaining from the MWNT synthesis is highlighted in green).

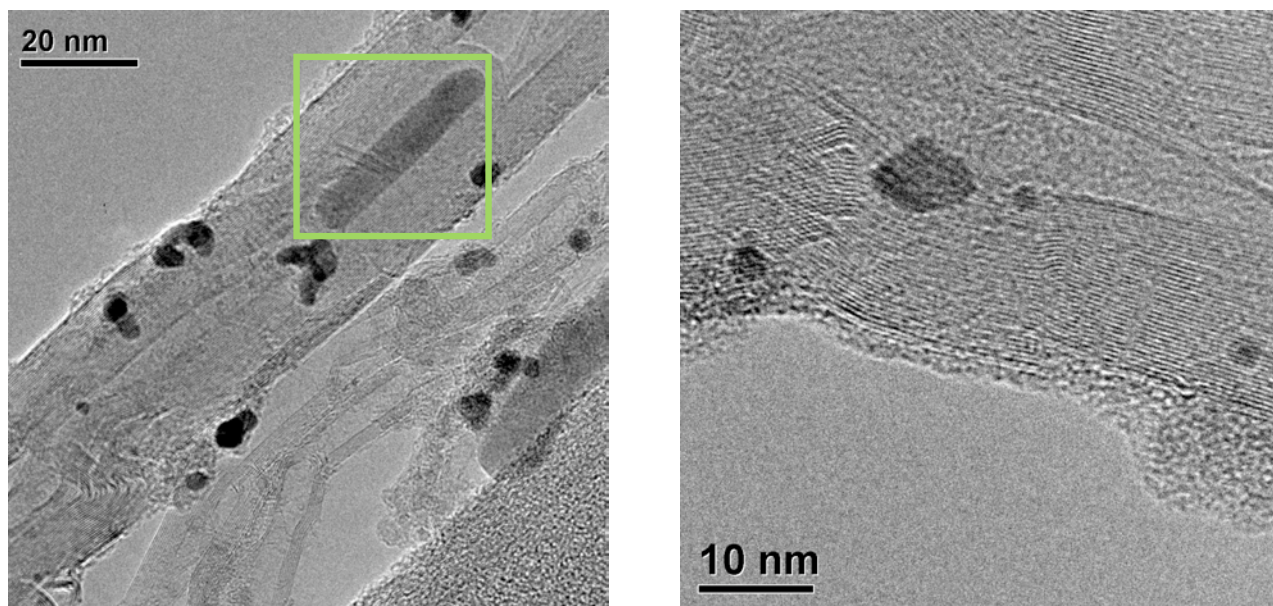


Figure 43. TEM micrographs of 3:1 Pt-Rh/NO₂-fMWNTs/metal monolith (an iron catalyst particle remaining from the MWNT synthesis is highlighted in green).

From the figures, it is evident that in both cases metal deposition onto the monolith-grown NO₂-fMWNTs indeed took place and that particles of *ca.* 5 nm in diameter were produced. Finally, in order to quantify the amount of metal successfully deposited, each preparation's washings were

analyzed *via* PIXE and the amount of metal deposited was calculated by difference. By this method, the monometallic catalyst was determined to contain 58 g Pt/cuft, whereas the bimetallic catalyst was found to contain 69 g 3:1 Pt-Rh/cuft.

9. Engine tests.

Pt/NO₂-fMWNTs/metal monolith catalyst:

Engine tests on the monolith catalysts were performed at Oak Ridge National Laboratory, using a 4-cylinder, 1.7-liter common-rail diesel engine coupled to a motoring DC dynamometer. Details of the experimental set-up are described in the Appendix. To expedite the testing, and to provide a comparison with microreactor data collected on the powder catalyst samples, propene was used as the reductant, supplied externally from a gas cylinder. Figures 44 and 45 summarize the results of experiments in which the average catalyst temperature was varied at constant space velocity - corresponding to 30,000 h⁻¹ and 50,000 h⁻¹, respectively - using a fixed C:NO_x ratio of 8.

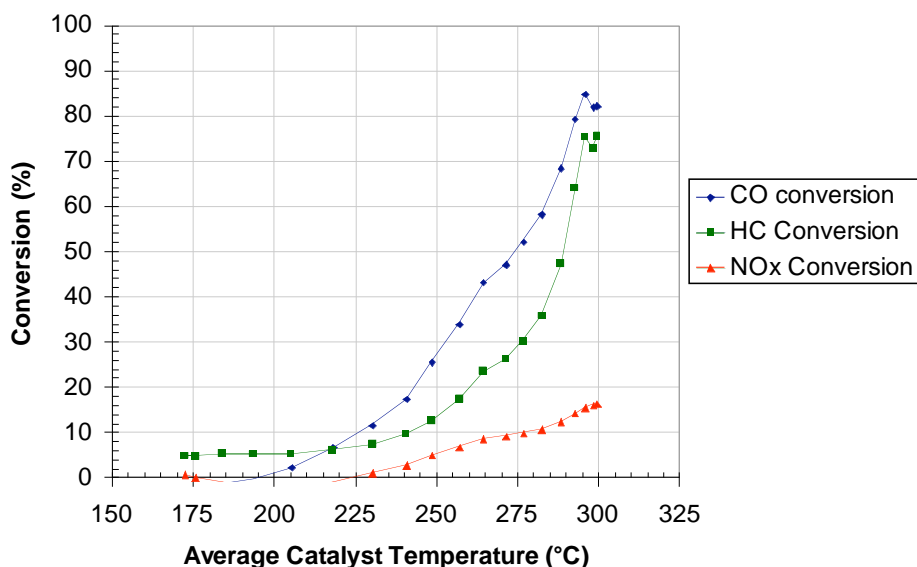


Figure 44. Results of temperature sweep for Pt/NO₂-fMWNTs/metal monolith catalyst. GHSV = 30,000 h⁻¹, C:NO_x = 8:1.

From these results it is apparent that while the catalyst is moderately active for the conversion of CO and hydrocarbons (the latter being mostly propene), the NO_x reduction activity is low. Rather surprisingly, NO_x conversion increases with temperature up to 300 °C, this having been fixed as the maximum operating temperature of the catalyst (in order to avoid any possible thermal damage). This contrasts with results obtained in microreactor tests (see Table 12), in which the temperature of maximum NO conversion (T_{max}) was found to fall in the range 205-225 °C for MWNT-supported Pt catalysts. Direct comparison of the results of powder and monolith catalyst tests are hampered by the considerable difference in effective space velocity used in the two

types of test. In the latter case, the GHSV is calculated on the basis of the entire monolith volume and the effective GHSV is therefore much higher than for a powder catalyst sample; this alone may explain the difference in NO_x reduction activity. Additionally, there are several other possible factors that may contribute to the high T_{max} value: (i) the actual Pt loading may be lower than indicated by chemical analysis of the filtrate and washings resulting from the catalyst preparation (a low concentration of catalytically active sites would be expected to result in a shift in the HC, CO and NO_x light-off curves to higher temperature); (ii) the bulk Pt dispersion might be worse than indicated by TEM, which would again represent a low concentration of active sites; and (iii) the catalyst might have been inhibited by components in the exhaust gas. Note that in the case of (i), a low Pt loading would also result in low NO_x conversion. In the case of a poor Pt dispersion, the NO_x conversion would not necessarily be decreased according to literature data [22,23,39,40]; however, a shift in the T_{max} to higher temperature might be expected, given that that this is tied to the light-off temperature of the hydrocarbon reductant. The exhaust gas composition was inevitably somewhat different from the feed used in the microreactor experiments. However, it seems unlikely that this difference alone could produce such a significant deviation in results. In order to address these issues, post mortem analyses will be performed on the Pt and Pt-Rh monolith catalysts used in this study; these analyses will enable a direct assessment of bulk metal loadings and dispersions. Finally, it should be noted that although the propene was injected in a turbulent area upstream of the catalyst, mixing may have been less than optimal. While this would not be expected to shift the T_{max} , it would negatively affect the NO_x conversion.

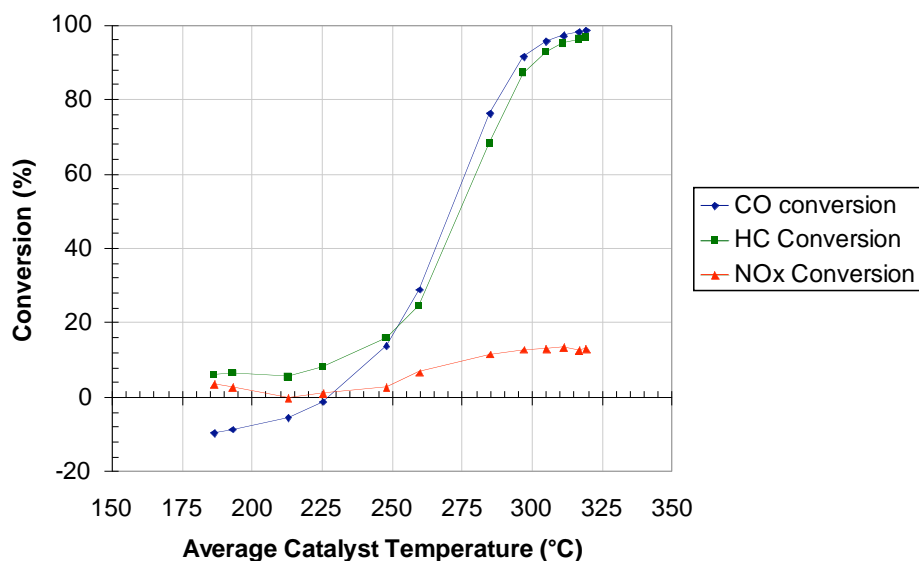


Figure 45. Results of temperature sweep for Pt/ NO_2 -fMWNTs/metal monolith catalyst. GHSV = $50,000 \text{ h}^{-1}$, C: NO_x = 8:1.

Comparison of the data in Figures 44 and 45 reveals that increasing the space velocity from $30,000 \text{ h}^{-1}$ to $50,000 \text{ h}^{-1}$ had only a minor effect on the NO_x , HC and CO conversion. NO_x conversion peaked at around 17% at the lower GHSV and 13.5% at the higher value, while the

CO and HC light-off appeared slightly better at 50,000 h⁻¹ (as reflected in the temperature required for 50% conversion); the differences were small, however, and may be due to a slight shift in the operating conditions. The relatively low NO_x conversion hampered the measurement of accurate product selectivities; however, based on N₂O concentrations measured by FT-IR (data not shown), the selectivity to N₂O fell in the range ~35-100%.

3:1 Pt-Rh/NO₂-fMWNTs/metal monolith catalyst:

The results of temperature sweep experiments performed using the 3:1 Pt-Rh/NO₂-fMWNTs/metal monolith catalyst are summarized in Figures 46 and 47. As before, space velocities of 30,000 h⁻¹ and 50,000 h⁻¹ were employed, respectively, at a fixed C:NO_x value of 8.

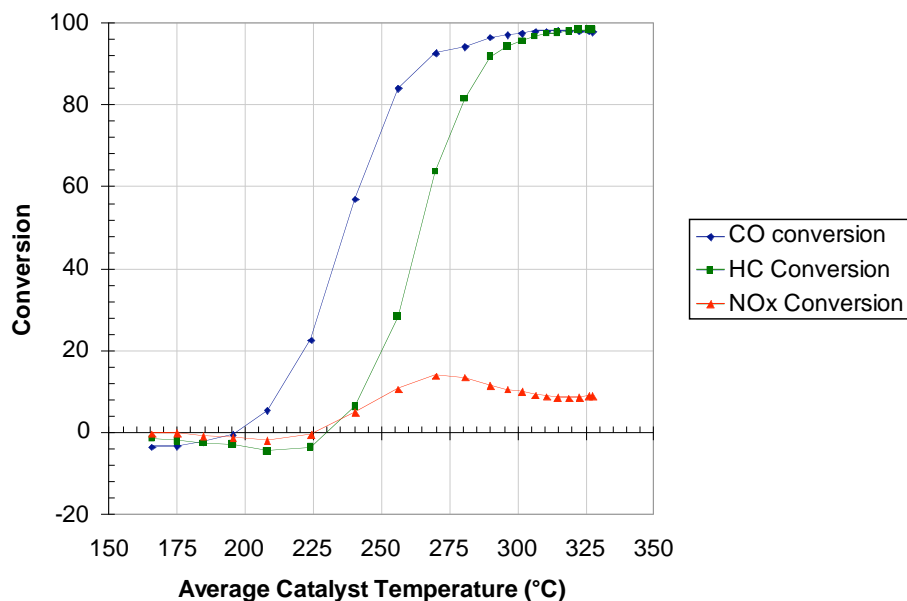


Figure 46. Results of temperature sweep for 3:1 Pt-Rh/NO₂-fMWNTs/metal monolith catalyst. GHSV = 30,000 h⁻¹, C:NO_x = 8:1.

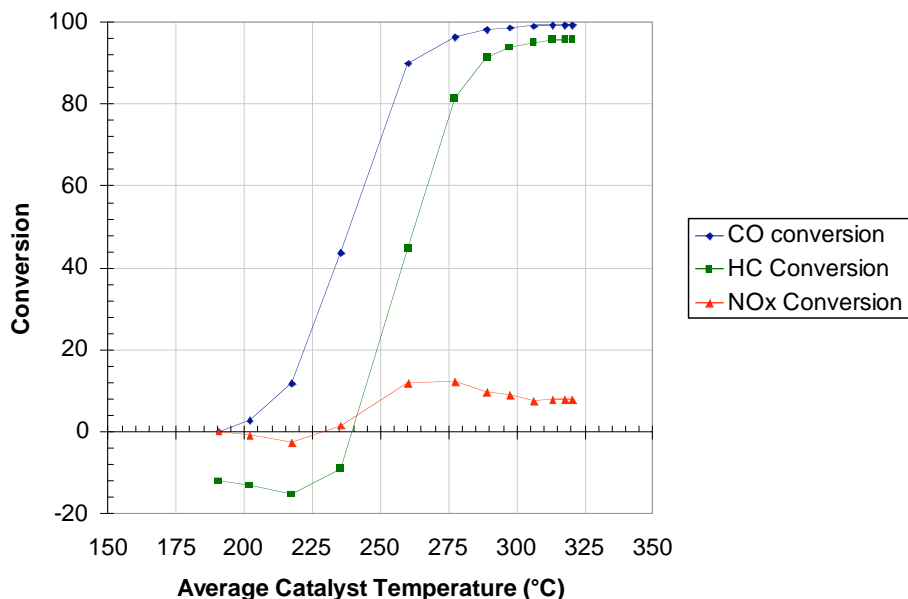


Figure 47. Results of temperature sweep for 3:1 Pt-Rh/NO₂-fMWNTs/metal monolith catalyst. GHSV = 50,000 h⁻¹, C:NO_x = 8:1.

As found for the Pt catalyst, the temperature of maximum NO_x conversion for the 3:1 Pt-Rh catalyst is shifted significantly relative to the earlier microreactor tests. From Figures 46 and 47, a T_{max} of ~270 °C is apparent, as compared to the T_{max} of 200 °C reported in Table 12. In comparison to the Pt catalyst, the Pt-Rh analogue showed slightly higher activity for CO and HC oxidation at both space velocities examined, while the NO_x conversion was comparable.

In order to investigate the effect of the reductant:NO_x ratio on catalyst performance, runs were conducted at fixed inlet temperature (270 °C) and space velocity (50,000 h⁻¹). As shown in Figure 48, increasing the C:NO_x ratio resulted in a progressive increase in NO_x conversion up to a maximum value of 18%, obtained at a C:NO_x ratio of 17. Also of note is the observation that above a C:NO_x ratio of ~14, the HC and CO conversions started to decline. This is likely due to the fact that at such high C:NO_x ratios the catalyst surface is mainly covered by hydrocarbons, thereby preventing the adsorption of sufficient oxygen for efficient CO and HC oxidation.

Figure 49 shows the N₂O concentration measured during the foregoing experiment. Of interest is the finding that the N₂O make declines at high C:NO_x ratios, even as the NO_x conversion is increasing. This suggests that high hydrocarbon surface coverage inhibits N₂O formation, which may therefore provide a means of mitigating N₂O emissions during HC-SCR over this catalyst (albeit at increased fuel penalty). Based on the data in Figure 49, the calculated N₂O selectivity ranges from 40% to 100%, which is comparable to that observed for the Pt catalyst and is in broad agreement with the results of earlier microreactor experiments.

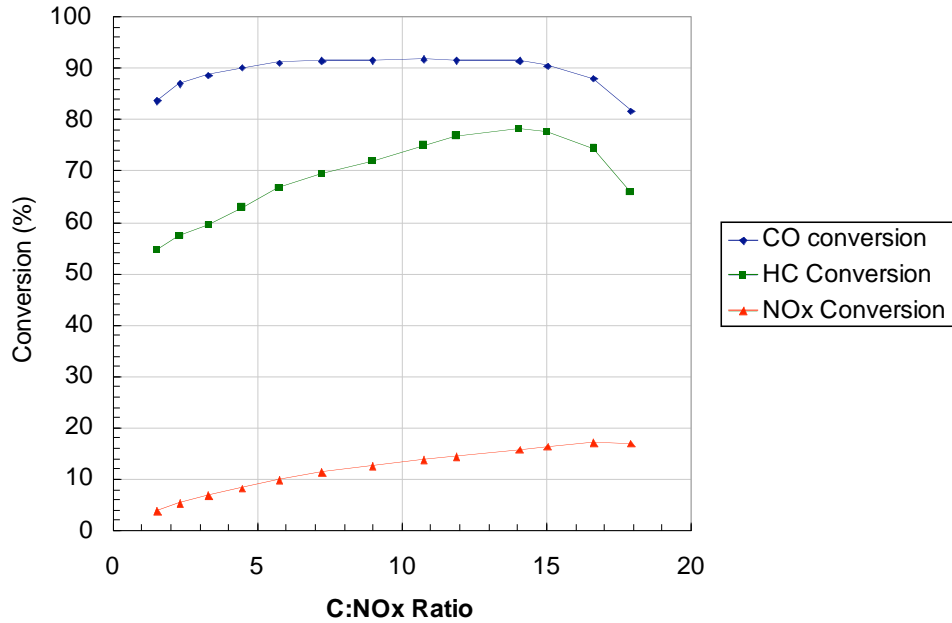


Figure 48. Results of C:NO_x sweep for 3:1 Pt-Rh/NO₂-fMWNTs/metal monolith catalyst. GHSV = 50,000 h⁻¹, T = 270-290 °C.

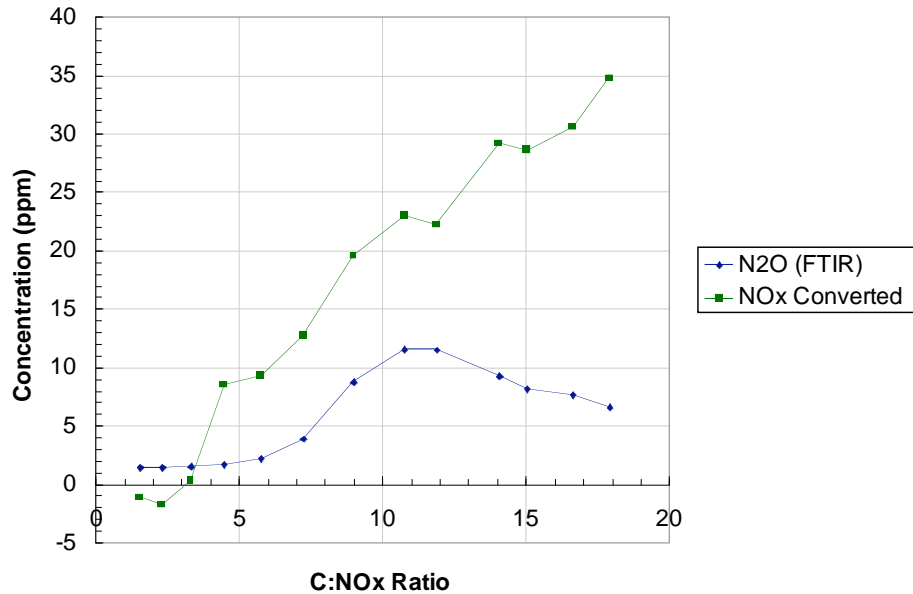


Figure 49. N₂O make during C:NO_x sweep for 3:1 Pt-Rh/NO₂-fMWNTs/metal monolith catalyst. GHSV = 50,000 h⁻¹, T = 270-290 °C.

In summary, the results of engine tests reveal that the monolithic Pt and Pt-Rh catalysts are fairly active for the oxidation of CO and hydrocarbons, while NO_x reduction activity was found to be rather low; this fact can be largely attributed to the very high effective space velocities used, although others factors may play a role. For the Pt-Rh catalyst, NO_x conversion increased with increasing C:NO_x ratio up to a limiting value at C:NO_x = 17. Of interest is the finding that the N₂O make declines at high C:NO_x ratios, even as the NO_x conversion is increasing. This suggests that high hydrocarbon surface coverage inhibits N₂O formation.

Finally, it is worth addressing the issue of catalyst architecture. For both the Pt and Pt-Rh catalysts studied, the metal loadings (58 g/cuft and 69 g/cuft, respectively) are in the range typically employed for diesel oxidation catalysts (DOCs) used on LD diesel vehicles. However, due to the low density of the MWNTs support, the loading of MWNTs on the monolith (7 g for the 0.41 L monolith, equivalent to 17 g/L) is much lower than the washcoat loading of a typical DOC or HC-SCR catalyst (~100 g/L). This has two main consequences: (i) it necessitates the use of high metal loadings on the MWNTs support (10.8 wt% and 12.5 wt%, respectively, for the Pt and Pt-Rh catalysts), which will tend to result in sub-optimal metal dispersions (in comparison with those possible at lower metal loadings); and (ii) the low MWNT loading will tend to diminish the direct involvement of the support in catalysis (e.g., as compared to the powder catalyst samples tested earlier in this work). These considerations highlight the potential disadvantages of employing a conventional metal monolith as the catalyst substrate. A better approach may be to form the MWNTs into a rigid, self-supporting foam monolith, as done for activated carbon in certain environmental applications [64]. This should eliminate the above drawbacks, potentially improving catalyst performance.

Conclusions:

- Powder-type HC-SCR catalysts possessing low temperature deNO_x activity superior to that shown by Pt/Al₂O₃ have been developed by using MWNTs as the catalyst support. The difference in activity has been assigned to the more reduced state in which the metals are kept in MWNTs-based formulations, although additional work is required to validate this idea.
- Due to the fact that the functionalization of the MWNT support prior to metal deposition translates into an added increase in activity, the acidity of the support has also been invoked to explain the superior performance of fMWNTs-based catalysts.
- When compared to other carbon-based HC-SCR formulations, MWNTs-supported catalysts are observed to be more active for NO reduction.
- Improvements have also been made through the use of alloys as the catalytically active phase, a 3:1 Pt-Rh alloy offering the maximum deNO_x activity, the lowest light-off temperature and the widest temperature window of operation. Regrettably, the N₂-selectivity shown by Pt catalysts is not significantly improved by alloying with Rh at this level.
- The promotion of MWNTs-based catalysts with Na⁺ achieves both a significant increase in N₂-selectivity and a considerable widening of the temperature window of operation. However, these effects are accompanied by a substantial decrease in NO_x conversion. Further, the occurrence of promotion effects is highly dependent on both the Pt:Na ratio and the catalyst preparation method.
- Monolithic catalysts have been prepared by growing MWNTs on metallic monoliths, activating the monolith-grown MWNTs with NO₂ and depositing precious metals *via* an *in situ* chemical reduction process.
- The results of engine tests reveal that the monolithic Pt and Pt-Rh catalysts are fairly active for the oxidation of CO and hydrocarbons, while NO_x reduction activity was found to be rather low; this fact can be largely attributed to the very high effective space velocities used, although others factors may play a role.

References:

1. M. Ishikawa, JP 2000140644 (to Toyota Motor Corp.).
2. M. Crocker, unpublished results.
3. H. Iwakuni, A. Takami, K. Komatsu, *Stud. Surf. Sci. Catal.*, **121** (1999) 251.
4. A. Takami, T. Takemoto, H. Iwakuni, K. Yamada, M. Shigetsu, K. Komatsu, *Catal. Today*, **35** (1997) 75.
5. A. Takami, T. Takemoto, H. Iwakuni, F. Saito, K. Komatsu, Society of Automotive Engineers, 950746 (1995).
6. M. Shigetsu, A. Takami, M. Kyougoku, H. Iwakuni, F. Saito, K. Komatsu, *Matsuda Giho*, **13** (1995) 30.
7. S. Nojima, K. Iida, N. Kobayashi, *Nippon Kagaku Kaishi*, 2001, 27.
8. R. Andrews, D. Jacques, A.M. Rao, F. Derbyshire, D. Qian, X. Fan, E.C. Dickey, J. Chen, *Chem. Phys. Lett.*, **303** (1999) 467.
9. R. Yu, L. Chen, Q. Liu, J. Lin, K.-L. Tan, S.C. Ng, H.S.O. Chan, G.-Q. Xu, T.S.A. Hor, *Chem. Mater.*, **10** (1998) 718.
10. S.C. Tsang, Y.K. Chen, P.J.F. Harris, M.L.H. Green, *Nature*, **372** (1994) 159.
11. Y. Xing, *J. Phys. Chem. B*, **108** (2004) 19255.
12. I. Salame, T. Bandoz, *J. Coll. Interfac. Sci.*, **240** (2001) 252.
13. W. Li, C. Liang, W. Zhou, J. Qiu, H. Li, G. Sun, Q. Xin. *Carbon* **42** (2004) 436.
14. W. Chen, J. Lee, Z. Liu. *Mater. Lett.* **58** (2004) 3166.
15. W. Li, C. Liang, J. Qiu, W. Zhou, H. Han, Z. Wei, G. Sun, Q. Xin, *Carbon* **40** (2002) 791.
16. J. Garcia, H.T. Gomes, P. Serp, P. Kalck, J.L. Figueiredo, J.L. Faria, *Catal. Today*, **102-103** (2005) 101.
17. J. M. García-Cortés, M. J. Illán-Gómez, A. Linares Solano, C. Salinas-Martínez de Lecea. *Appl. Catal., B* **25** (2000) 39.
18. B. Ioan, A. Miyazaki, K. Aika. *Appl. Catal. B* **59** (2005) 71.
19. J. Li, J. Hao, L. Fu, T. Zhu. *Top. Catal.* **30/31** (2004) 81.
20. G.R. Bamwenda, A. Obuchi, A. Ogata, J. Oi, S. Kushiyama, K. Mizuno. *J. Mol. Catal. A: Chem.* **126** (1997) 151.
21. A. Obuchi, I. Kaneko, J. Oi, A. Ohi, A. Ogata, G.R. Bamwenda, S. Kushiyama. *Appl. Catal. B* **15** (1998) 37.
22. J.M. García-Cortés, J. Pérez-Ramírez, M.J. Illian-Gómez, F. Kapiteijn, J.A. Moulijn, C. Salinas-Martínez de Lecea, *Appl. Catal. B*, **30** (2001) 399.
23. J.M. García-Cortés, M.J. Illán-Gómez, A. Linares Solano, C. Salinas-Martínez de Lecea, *Appl. Catal. B*, **25** (2000) 39.
24. H. Hamada, Y. Kintaichi, M. Sasaki, T. Ito, *Appl. Catal. A*, **75** (1991) L1.
25. M. Inaba, Y. Kintaichi, H. Hamada, *Catal. Lett.*, **36** (1996) 223.
26. R. Burch, *Catal. Today*, **35** (1997) 27.
27. R. Burch, P. J. Millington, *Catal. Today*, **29** (1996) 37.
28. G. Zhang, Y. Yamaguchi, H. Kawakami, T. Suzuki, *Appl. Catal. B*, **1** (1992) L15.
29. H. Hamada, *Catal. Today*, **22** (1994) 21 and references therein.
30. H. H. Ingelsten, M. Skoglundh, E. Fridell, *Appl. Catal. B*, **41** (2003) 287.
31. G. R. Bamwenda, a. Ogata, a. Obuchi, J. Oi, K. Mizuno, J. Skrzypek, *Appl. Catal. B*, **6** (1995) 311.
32. K. S. Oh, S. I. Woo, *Catal. Lett.*, **110** (2006) 247.

33. A. Giroir-Fendler, P. Denton, A. Boreave, H. Praliaud, M. Primet, *Top. Catal.*, **16** (2001) 237.
34. F. Figueras, B. Coq, E. Ensuque, D. Tachon, G. Delahay, *Catal. Today*, **42** (1998) 117.
35. A. Satsuma, K. Yamada, T. Mori, M. Niwa, T. Hattori, Y. Murakami, *Catal. Lett.*, **31** (1995) 367.
36. O. V. Metelkina, V. V. Lunin, V. A. Sadykov, S. A. Beloshapkin, G. M. Alikina, E. V. Lunina, O. O. Parenago, *Petroleum Chem.*, **40** (2000) 90.
37. K. Kawabata, H. Yoshimatsu, K. Fujiwara, T. Yabuki, A. Osaka, A. Miura, *J. Mater. Sci.*, **34** (1999) 2529.
38. W. Z. Li, C. H. Liang, W. J. Zhou, J. S. Qiu, Z. H. Zhou, G. Q. Sun, Q. Xin, *J. Phys. Chem. B*, **107** (2003) 6292.
39. J. H. Lee, H. H. Kung, *Catal. Lett.*, **51** (1998) 1.
40. M. C. Demicheli, L. C. Hoang, J. C. Ménéz, J. Barbier, M. Pinabiau-Carlier, *Appl. Catal. A*, **97** (1993) L11.
41. R. Burch, P. J. Millington, a. P. Walker, *Appl. Catal. B*, **4** (1994) 65.
42. P. Denton, A. Giroir-Fendler, H. Praliaud, M. Primet, *J. Catal.*, **189** (2000) 410.
43. R. Burch, P. J. Millington, *Catal. Today*, **26** (1995) 185.
44. E. Xue, K. Seshan, J. R. H. Ross, *Appl. Catal. B*, **11** (1996) 65.
45. K. Otto, H. C. Yao, *J. Catal.*, **66** (1980) 229.
46. J. Kaspar, C. de Leitenburg, P. Fornasiero, A. Trovarelli, M. Graziani, *J. Catal.*, **146** (1994) 136.
47. X. Xu, D. W. Goodman, *Catal. Lett.*, **24** (1994) 31.
48. R. Verdejo, S. Lamoriniere, B. Cottam, A. Bismarck, M. Shaffer, *Chem. Comm.*, **5** (2007) 513.
49. A. Obuchi, A. Ohi, M. Nakamura, A. Ogata, K. Mizuno, H. Ohuchi, *Appl. Catal. B*, **2** (1993) 71.
50. L. Mussmann, D. Lindner, M. Votsmeier, E. Lox, T. Kreuzer. EP1138382 (2001).
51. P. Vernoux, A. Y. Leinekugel-Le-Cocq, F. Gaillard, *J. Catal.*, **219** (2003) 247.
52. I. V. Yentekakis, V. Tellou, G. Botzolaki, I. A. Rapakousios, *Appl. Catal. B*, **56** (2005) 229.
53. N. D. Lang, J. K. Holloway, J. K. Norskov, *Surf. Sci.*, **150** (1985) 24.
54. N. Macleod, J. Isaac, R. M. Lambert, *Appl. Catal. B*, **33** (2001) 335.
55. E. F. Iliopoulou, A.P. Evdou, A.A. Lemonidou and I.A. Vasalos, *Appl. Catal. A*, **274** (2004) 179.
56. K. Sato, T. Yoshinari, Y. Kintaichi, M. Haneda, H. Hamada, *Catal. Commun.*, **4** (2003) 315.
57. K. Sato, T. Yoshinari, Y. Kintaichi, M. Haneda, H. Hamada, *Appl. Catal. B*, **44** (2003) 67.
58. J. M. García-Cortés, J. Pérez-Ramírez, J. N. Rouzaud, A. R. Vaccaro, M. J. Illán-Gómez, C. Salinas-Martínez de Lecea, *J. Catal.*, **218** (2003) 111.
59. <http://srdata.nist.gov/xps/>.
60. J. A. Botas, M. A. Gutierrez Ortiz, M. P. Gonzales Marcos, J. R. Gonzales Velasco, *Appl. Catal. B*, **32** (2001) 243.
61. I. Kvande, S. T. Briskeby, M. Tsympkin, M. Rønning, S. Sunde, R. Tunold, D. Chen, *Topics Catal.*, **45** (2007) 81.
62. X. Hu, T. Wang, X. Qu, S. Dong, *J. Phys. Chem. B*, **110** (2006) 853.
63. J. Parks, B. West, M. Swartz, S. Huff, SAE Technical Paper no. 2008-01-0448.
64. B. Crittenden, A. Patton, C. Jouin, S. Perera, S. Tennison, J.A.B. Echevarria, *Adsorption*, **11** (2005) 537.

Appendix: Experimental Methods.

A. Preparative.

Functionalization of MWNTs with a mixture of 1:1 H₂SO₄-HNO₃:

15 g of MWNTs were suspended in a mixture of 750 mL of H₂SO₄ and 750 mL of HNO₃ *via* sonication. The resulting suspension was refluxed for 4 h, allowed to cool, mixed with an equal volume of deionized water and allowed to settle. The supernatant was then decanted and replaced by an equal volume of deionized water. The resulting suspension was filtered and the cake was washed with deionized water and allowed to dry in a vacuum oven. The dry product was then pulverized, re-suspended in deionized water *via* sonication, and washed by a cycle of centrifuging, decanting and suspending in deionized water until the washings attained a neutral pH, at which point the supernatant was decanted and the solid dried in a vacuum oven.

PGM deposition via wet impregnation:

1 g of catalyst support was mixed with 100 mL of solvent (ethanol for MWNTs and deionized water for fMWNTs) and the appropriate amount of metal precursor(s) (H₂PtCl₆ · 6H₂O or H₂PtCl₆ · 6H₂O and RhNO₃). The mixture was sonicated for 30 min and the solvent was then removed from the resulting suspension using a rotary evaporator. The resulting material was dried in a vacuum oven and then reduced under a flow of H₂ (300 °C, 3 h).

PGM deposition via the polyol method:

1 g of catalyst support was suspended in 100 mL of ethylene glycol *via* sonication. The appropriate amount of metal precursor(s) (H₂PtCl₆ · 6H₂O or H₂PtCl₆ · 6H₂O and RhNO₃ in aqueous solution) was added dropwise to the resulting suspension while stirring. A saturated solution of KOH in ethylene glycol was then added dropwise to the mixture until it attained a pH of >13. The resulting mixture was refluxed for 3 h, allowed to cool, and filtered. The cake was washed (first with a dilute aqueous solution of NH₄OH, then with deionized water) and dried in a vacuum oven.

Growth of MWNTs on a metal monolith:

A stainless steel 300 cpsi metal monolith (DCL, Inc., Toronto, ON) was packed into a fused quartz horizontal reactor and placed in an electric furnace. Argon was flowed through the metal monolith while the temperature of the reactor was raised to 800 °C. Once this temperature was reached, the flow of argon was switched to a flow of 10 % H₂ in Ar and a saturated solution of ferrocene in xylenes was fed into the reactor for 1 h. The system was then allowed to cool to room temperature under an inert atmosphere. The reactor was then turned around and the run was repeated to ensure MWNT growth throughout the entire inside of the monolith. Typically, two runs yielded *ca.* 7 g of metal monolith-supported MWNTs.

Functionalization of metal monolith-grown MWNTs with 0.5% NO₂ in N₂:

A stainless steel 300 cpsi metal monolith coated with MWNTs was packed into a fused quartz horizontal reactor placed in an electric furnace. Nitrogen was flowed through the metal monolith while the temperature of the reactor was raised to 300 °C. Once this temperature was reached, the flow of nitrogen was switched to 0.5 % NO₂ in N₂ and the flow maintained for 1 h. The system was then allowed to cool to room temperature under inert atmosphere. The reactor was then

turned around and the run was repeated to ensure MWNT functionalization throughout the entire inside of the monolith.

PGM deposition on NO₂-functionalized monolith-grown MWNTs via the polyol method:

The appropriate amount of metal precursor(s) ($\text{H}_2\text{PtCl}_6 \cdot 6\text{H}_2\text{O}$ or $\text{H}_2\text{PtCl}_6 \cdot 6\text{H}_2\text{O}$ and RhNO_3) was dissolved in ethylene glycol and the resulting solution was stirred for 15 min. A NO₂-functionalized MWNTs-coated 300 cpsi stainless steel monolith was then dipped in the solution and the stirring continued for 15 min. The system was then heated to 160 °C and kept at this temperature for 1.5 h, after which the monolith was turned upside down and the temperature maintained at 160 °C for a further 1.5 h. The monolith was then drained, dried, washed with deionized water, and dried again. Using this method, both a monometallic and a bimetallic monolithic catalyst were prepared. The monometallic catalyst was determined to contain 58 g Pt/cuft, whereas the bimetallic catalyst was found to contain 69 g 3:1 Pt-Rh/cuft.

B. Analytical.

Determination of precious metal loadings:

For alumina-supported reference catalysts, the precious metal loading was determined by means of XRF. For catalysts with carbonaceous materials (Darco KB-B, activated carbon fibers, MWNTs or fMWNTs) as the support, the precious metal loading was determined *via* PIXE at Elemental Analysis, Inc. (Lexington, KY), using a General Ionex Corp. Tandetron Model 4110A proton accelerator coupled with a custom X-ray Emission apparatus. To determine the precious metal density of PGM/NO₂-fMWNTs/metal monolith catalysts, the filtrate and washings from the preparations were collected, analyzed *via* PIXE, and the amount of metal successfully deposited was calculated by subtraction. Prior to PIXE analysis, solid samples were homogenized in an agate or cryogenic mixer mill and a pellet was pressed using ~300 mg of material. For liquid samples, preparation prior to analysis involved pouring the sample into an 8 mL Teflon cup and covering with a Kapton film through which the sample was irradiated.

Precious metal particle size analysis:

H₂-chemisorption measurements were performed in a Zeton Altamira AMI-200 instrument by first ramping at 1 °C/min to a reduction temperature of 400 °C and holding at this temperature for 1 h under a flow of 10% H₂ in He. The sample was then cooled to 100 °C under a flow of Ar. To count the active metal sites, the temperature was then ramped to 400 °C under a flow of Ar, the desorbed hydrogen being monitored with a thermal conductivity detector (TCD). The temperature was held at 400 °C until the TCD signal returned to the baseline condition. The Pt dispersion was calculated on the assumption of a 1:1 H:Pt stoichiometric ratio and a spherical particle morphology.

To prepare samples for TEM, a small amount of the material was first dispersed in the appropriate solvent (acetone and *o*-xylene for alumina-supported and MWNTs-based catalysts, respectively) *via* sonication. A drop of the resulting dispersion was then placed on a 200 mesh lacey carbon-copper grid and the solvent was allowed to evaporate in a vacuum oven. TEM and STEM observations were performed using a JEOL 2010F field emission analytical transmission electron microscope operated at an accelerating voltage of 200kV, coupled to a STEM unit with a high-angle annular dark field (HAADF) detector and a Gatan Imaging Filter. The electron beam had a point-to-point resolution of 0.2 nm. To obtain particle size distribution histograms,

200 precious metal particles were measured in high magnification TEM micrographs using image analysis software (Gatan Digital Micrograph®).

Thermogravimetric analyses:

Thermogravimetric measurements were made using a TA Instruments Q500 analyzer. In all cases the total gas flow was 50 mL/min and the temperature was ramped from room temperature to 800 °C at a rate of 5 °C/min.

Spectroscopic analyses:

XPS analyses were performed on a PHI 5600 LS instrument, using an Al K α X-ray radiation source. The analysis area was 1 × 3 mm and the C 1s line (285.0 eV) was employed as a binding energy standard.

TEM-EDS and STEM-EDS analyses were carried out either by converging the beam in TEM mode or using the 1 nm analytic probe in STEM mode. For elemental mapping, sample preparation consisted of lightly dusting catalyst powder onto a 200 mesh lacey carbon-copper grid. Spectrum images were then obtained in STEM mode using the EmiSpec. Inc., EsVision software.

C. Catalyst testing.

Powder catalysts:

Experiments were performed in a vertical stainless steel tube reactor (1 cm inner diameter). The catalyst (1 g) was packed into a ~2.5 cm bed between plugs of glass wool. The gas mixture was flowed downwards through the catalyst bed and consisted of 500 ppm NO, 10% O₂, 10% H₂O and 500 ppm of propene as the reductant balanced with N₂. The gas flows were regulated with mass flow controllers and the total flow rate was kept at 1667 cm³/min (STP), corresponding to a space velocity of ca. 50,000 h⁻¹ (W/F = 0.01 g · h · dm⁻³). Data points were taken at steady state in non-sequential intervals of 10 °C to account for possible hysteresis in the range 180-300 °C, the temperature being monitored by a thermocouple placed in the catalyst bed. The outlet gases were continuously analyzed using a chemiluminescence NO-NO₂ analyzer (ECO PHYSICS® CLD 700 EL ht) and discontinuously analyzed for N₂O with a high level gas filter correlation analyzer (Thermo Electron Corp. model 46C). NO conversion and N₂O selectivity were calculated according to expressions (1) and (2):

$$\text{NO conv. (\%)} = [([\text{NO}_x]_i - [\text{NO}_x]_o) \times 100] / [\text{NO}_x]_i \quad (1)$$

$$\text{N}_2\text{O selec. (\%)} = [([\text{N}_2\text{O}]_o \times 2) \times 100] / ([\text{NO}_x]_i - [\text{NO}_x]_o) \quad (2)$$

where [NO_x]_i and [NO_x]_o are inlet and outlet NO_x (NO+NO₂) concentrations, respectively, and [N₂O]_o represents the outlet N₂O concentration.

Monolith catalysts:

Tests were conducted at Oak Ridge National Laboratory, in the Fuels, Engines, and Emissions Research Center. A Mercedes OM668 4-cylinder, 1.7-liter common-rail diesel engine was coupled to a motoring DC dynamometer. The engine, which is a 1999 model used in the Mercedes A170 in Europe, has a bore and stroke of 80 mm and 84 mm respectively, and it has a rated power output of 66kW (89 hp) at 4200 rpm. Modifications to the engine included the addition of an electronic intake throttle, an electronically controlled high flow exhaust gas recirculation (EGR) valve (in lieu of the stock vacuum-operated valve), and an EGR cooler [63].

Additionally, the factory engine control module was replaced with a rapid development engine controller based on a dSpace® MicroAutoBox. This rapid development system (RDS) was developed in partnership with Ricardo, Inc., and provides complete control over all engine electronics, including timing, duration, and number of fuel injection events, fuel rail pressure, intake throttle, EGR valve, and turbocharger wastegate.

Temperature sweep experiments were performed by increasing the engine load in stepwise fashion at fixed engine speed (1500 rpm). No EGR was employed. The catalyst volume was 0.41 L. Experiments were conducted at GHSVs of either 30,000 or 50,000 h⁻¹. To obtain the desired exhaust gas flows, a slipstream was taken from the main exhaust flow. In the experiments, propene was used as the reductant, supplied externally from a gas cylinder. The propene was injected at a distance of ~15" upstream of the catalyst face, in a turbulent area immediately downstream of the split in the exhaust to the slipstream. The mixed gas passed through an elbow and expansion cone (from 2.5" pipe to 3.5" pipe) prior to the catalyst. To monitor the temperature across the catalyst, thermocouples were placed approximately 2" from the front catalyst face and about 1.5" from the catalyst face on the downstream side.

Dual conventional emissions benches were used for raw exhaust sampling. These benches use California Analytical Instruments® (CAI) non-dispersive infrared (NDIR) analyzers for carbon monoxide (CO) and carbon dioxide (CO₂), heated chemiluminescence detectors (HCLD) for NO_x, and heated flame ionization detectors (HFID) for total hydrocarbons (HC). A Nicolet Rega 7000 Fourier Transform InfraRed (FTIR) analyzer was used for quantifying nitrous oxide (N₂O) in the diluted exhaust.